

<b>REPORT DOCUMENTATION PAGE</b>				<i>Form Approved</i> <i>OMB No. 0704-0188</i>	
The public reporting burden for this collection of information is estimated to average 1 hour per response, including the time for reviewing instructions, searching existing data sources, gathering and maintaining the data needed, and completing and reviewing the collection of information. Send comments regarding this burden estimate or any other aspect of this collection of information, including suggestions for reducing the burden, to the Department of Defense, Executive Services and Communications Directorate (0704-0188). Respondents should be aware that notwithstanding any other provision of law, no person shall be subject to any penalty for failing to comply with a collection of information if it does not display a currently valid OMB control number.					
<b>PLEASE DO NOT RETURN YOUR FORM TO THE ABOVE ORGANIZATION.</b>					
1. REPORT DATE (DD-MM-YYYY) 15/08/2012		2. REPORT TYPE		3. DATES COVERED (From - To) May 2009 - May 2012	
4. TITLE AND SUBTITLE Predicting Failure Initiation in Structural Adhesive Joints				5a. CONTRACT NUMBER	
				5b. GRANT NUMBER FA9550-09-1-0394	
				5c. PROGRAM ELEMENT NUMBER	
6. AUTHOR(S) Alberto Díaz Díaz				5d. PROJECT NUMBER	
				5e. TASK NUMBER	
				5f. WORK UNIT NUMBER	
7. PERFORMING ORGANIZATION NAME(S) AND ADDRESS(ES) Centro de Investigación en Materiales Avanzados S.C. Miguel de Cervantes 120. CI Chihuahua. 31109 Chihuahua, Chih. Mexico				8. PERFORMING ORGANIZATION REPORT NUMBER	
9. SPONSORING/MONITORING AGENCY NAME(S) AND ADDRESS(ES) AFOSR/IO 875 N RANDOLPH ST ARLINGTON, VA 22023				10. SPONSOR/MONITOR'S ACRONYM(S)	
				11. SPONSOR/MONITOR'S REPORT NUMBER(S) AFRL-OSR-VA-TR-2012-1124	
12. DISTRIBUTION/AVAILABILITY STATEMENT Distribution A: Approved for public release					
13. SUPPLEMENTARY NOTES					
14. ABSTRACT The aim of this project is to bring a better knowledge of the phenomena involved in the failure of structural adhesive joints and to develop new tools to predict the initiation of this failure. First, a constitutive model of the adhesive was developed by carrying out experiments on three types of adhesives. For two of these adhesives, a rigorous proof of important viscoplastic phenomena is shown. Arcan tests, tensional and torsional tests on butt joints and double lap joints were performed with the three adhesives and two metallic substrates in order to obtain a set of data for testing the accuracy of the predictions of a failure criterion. Linear and non-linear solid finite element calculations were carried out to analyze the stress state in the tested specimens. A layer-wise model was developed to ease the stress calculations in plate-like adhesive joints. In order to predict failure initiation, the solid finite element calculations and a twofold failure criterion involving simultaneously stress and energy conditions were applied. Accurate predictions were obtained for the adhesive joint specimens tested in this project. The layer-wise model and pertinent failure criteria					
15. SUBJECT TERMS Adhesive, failure, viscoplasticity, adhesive joint, butt joint tests, double lap joint tests, Arcan tests, finite element analysis, layer-wise model, strain energy release rate, failure criterion					
16. SECURITY CLASSIFICATION OF:			17. LIMITATION OF ABSTRACT	18. NUMBER OF PAGES	19a. NAME OF RESPONSIBLE PERSON
a. REPORT	b. ABSTRACT	c. THIS PAGE			Alberto Díaz Díaz
U	U	U	U	112	19b. TELEPHONE NUMBER (Include area code) 52614-4394802

Reset

## INSTRUCTIONS FOR COMPLETING SF 298

**1. REPORT DATE.** Full publication date, including day, month, if available. Must cite at least the year and be Year 2000 compliant, e.g. 30-06-1998; xx-06-1998; xx-xx-1998.

**2. REPORT TYPE.** State the type of report, such as final, technical, interim, memorandum, master's thesis, progress, quarterly, research, special, group study, etc.

**3. DATES COVERED.** Indicate the time during which the work was performed and the report was written, e.g., Jun 1997 - Jun 1998; 1-10 Jun 1996; May - Nov 1998; Nov 1998.

**4. TITLE.** Enter title and subtitle with volume number and part number, if applicable. On classified documents, enter the title classification in parentheses.

**5a. CONTRACT NUMBER.** Enter all contract numbers as they appear in the report, e.g. F33615-86-C-5169.

**5b. GRANT NUMBER.** Enter all grant numbers as they appear in the report, e.g. AFOSR-82-1234.

**5c. PROGRAM ELEMENT NUMBER.** Enter all program element numbers as they appear in the report, e.g. 61101A.

**5d. PROJECT NUMBER.** Enter all project numbers as they appear in the report, e.g. 1F665702D1257; ILIR.

**5e. TASK NUMBER.** Enter all task numbers as they appear in the report, e.g. 05; RF0330201; T4112.

**5f. WORK UNIT NUMBER.** Enter all work unit numbers as they appear in the report, e.g. 001; AFAPL30480105.

**6. AUTHOR(S).** Enter name(s) of person(s) responsible for writing the report, performing the research, or credited with the content of the report. The form of entry is the last name, first name, middle initial, and additional qualifiers separated by commas, e.g. Smith, Richard, J, Jr.

**7. PERFORMING ORGANIZATION NAME(S) AND ADDRESS(ES).** Self-explanatory.

**8. PERFORMING ORGANIZATION REPORT NUMBER.** Enter all unique alphanumeric report numbers assigned by the performing organization, e.g. BRL-1234; AFWL-TR-85-4017-Vol-21-PT-2.

**9. SPONSORING/MONITORING AGENCY NAME(S) AND ADDRESS(ES).** Enter the name and address of the organization(s) financially responsible for and monitoring the work.

**10. SPONSOR/MONITOR'S ACRONYM(S).** Enter, if available, e.g. BRL, ARDEC, NADC.

**11. SPONSOR/MONITOR'S REPORT NUMBER(S).** Enter report number as assigned by the sponsoring/monitoring agency, if available, e.g. BRL-TR-829; -215.

**12. DISTRIBUTION/AVAILABILITY STATEMENT.** Use agency-mandated availability statements to indicate the public availability or distribution limitations of the report. If additional limitations/ restrictions or special markings are indicated, follow agency authorization procedures, e.g. RD/FRD, PROPIN, ITAR, etc. Include copyright information.

**13. SUPPLEMENTARY NOTES.** Enter information not included elsewhere such as: prepared in cooperation with; translation of; report supersedes; old edition number, etc.

**14. ABSTRACT.** A brief (approximately 200 words) factual summary of the most significant information.

**15. SUBJECT TERMS.** Key words or phrases identifying major concepts in the report.

**16. SECURITY CLASSIFICATION.** Enter security classification in accordance with security classification regulations, e.g. U, C, S, etc. If this form contains classified information, stamp classification level on the top and bottom of this page.

**17. LIMITATION OF ABSTRACT.** This block must be completed to assign a distribution limitation to the abstract. Enter UU (Unclassified Unlimited) or SAR (Same as Report). An entry in this block is necessary if the abstract is to be limited.



## **FINAL REPORT**

### **Project:**

**Predicting Failure Initiation in Structural Adhesive Joints**

### **Principal Investigator's name:**

**Alberto Díaz Díaz**

### **Centro de Investigación en Materiales Avanzados S.C.**

Miguel de Cervantes 120.  
Complejo Industrial Chihuahua.  
31109 Chihuahua, Chihuahua. MEXICO  
Phone 52-614-439-48-02  
Fax: 52-614-439-11-12  
E-mail: alberto.diaz@cimav.edu.mx

**Award No: FA9550-09-1-0394**

**AFOSR Program manager: James Fillerup.**

**Reporting period: May 2009 - May 2012**

August 15, 2012

## **Abstract**

The aim of this project is to bring a better knowledge of the phenomena involved in the failure of structural adhesive joints and to develop new tools to predict the initiation of this failure. First, a constitutive model of the adhesive was developed by carrying out several experiments on three types of adhesives. For two of these adhesives, a rigorous proof of important viscoplastic phenomena is shown. This is a first important contribution of this project. Arcan tests, tensional and torsional tests on butt joints and double lap joints were performed with the three adhesives and two metallic substrates in order to obtain a set of data for testing the accuracy of the predictions of a failure criterion. Linear and non-linear solid finite element calculations were carried out to analyze the stress state in the tested specimens. A layer-wise model was developed to ease the calculation and analysis of stresses in plate-like adhesive joints. For these joints, a solid finite element analysis may become unaffordable owing to the computational cost. The layer-wise model is able to take into account non-linear phenomena in the adhesive layer and its calculations were validated theoretically and experimentally. This is a second important contribution of this project. In order to predict failure initiation, the solid finite element calculations and a twofold failure criterion involving simultaneously stress and energy conditions were applied. Accurate predictions were obtained for the adhesive joint specimens tested in this project. This is a third significant impact of this work. The layer-wise model was applied to the prediction of failure in tests with plate-like adhesive joints published by other researchers. A criterion on the cumulative plastic strain in the adhesive provides accurate predictions of cohesive failure for the considered joints. This is another noteworthy contribution of this project.

# Contents

Introduction .....	4
I. Experiments and modeling of the behavior of adhesives.....	6
1. Specimen preparation .....	6
1.1 Polyester specimens.....	6
1.2 Hysol specimens .....	7
2. Experimental results .....	8
2.1 Results for the polyester adhesive .....	8
2.2 Results for Hysol adhesives.....	9
3. Modeling.....	14
3.1 Case of the polyester adhesive.....	14
3.2 Case of Hysol adhesives .....	16
4. Current work to obtain a correct modeling of Hysol adhesives .....	22
4.1 Adhesive curing.....	23
4.2 Viscoplastic model .....	25
5. Conclusions .....	31
II. Adhesive joint experiments .....	32
1. Tests description and specimen preparation .....	32
1.1 Joints bonded with the polyester adhesive .....	32
1.2 Joints bonded with Hysol adhesives .....	35
2. Results .....	42
2.1 Joints bonded with the polyester adhesive .....	42
2.2 Joints bonded with Hysol adhesives .....	46
3. Conclusions .....	50
III. Stress calculation in structural adhesive joints .....	51
1. Solid finite element modeling .....	51
1.1 Linear elastic analysis for the tested adhesive joints.....	51
1.2 Non-linear analysis .....	62
2. A layer-wise model for plate-like adhesive joints .....	65
2.1 Model description .....	66
2.2 Theoretical validation .....	69
2.3 Experimental validation.....	75
3. Conclusions .....	80

IV. Failure prediction .....	82
1. Predictions based on a linear analysis .....	82
1.1 Selection of a failure criterion .....	82
1.2 Example of a failure prediction and determination of the failure parameters .....	85
1.3 Failure prediction for the tested adhesive joints .....	90
2. Predictions based on a non-linear analysis .....	94
2.1 Failure of a family of composite double lap joints .....	94
2.2 Failure of a family of T-joints .....	96
3. Conclusions .....	99
General conclusions.....	101
References .....	102
Appendix 1. Drawings and dimensions of devices. ....	105
1. Parts of the Arcan device.....	105
2. Type F specimens. ....	107
Appendix 2. Publications and thesis.....	109
1. Thesis.....	109
2. Publications in conferences .....	111
3. Publications in journals .....	111

## Introduction

The aim of this project is to bring a better knowledge of the phenomena involved in the failure of structural adhesive joints and to develop new tools to predict the initiation of this failure. A correct failure prediction requires the calculation of stresses, energies and/or strains in the adhesive joint. The accuracy of this calculation depends on the correctness of the constitutive model applied for the adhesive. The mechanical behavior may vary from one adhesive to another. For this reason, three types of adhesives were studied in this project; one of them exhibited a quasi linear elastic behavior whereas the others had a non-linear behavior. Another important aspect in the failure prediction is the precision of the method which solves the spatial differential equations of the structural problem. In this project, a solid finite element modeling and a layer-wise model are proposed to the analysis of stresses in adhesive joints with eventual material non-linearities. The final tool to be applied in a failure prediction is a failure criterion. This criterion involves material parameters that must be identified by tests on adhesive joints. A good criterion must predict failure for any geometry subjected to any loading condition. Herein, several adhesive joint tests are performed so as to identify the parameters involved in a failure criterion. In this project, failure criteria are developed and their accuracy is tested by comparing the failure predictions to experimental results.

This report is divided in four chapters. In chapter I, the tests with the studied adhesives are described, the experimental results are shown and a constitutive model of the mechanical behavior of the adhesives is proposed. In chapter II, adhesive joint tests are described and the failure loads for each test are listed. Chapter III describes the theoretical tools proposed in this project to calculate stresses in adhesive joints. In the last chapter, the previous tools and pertinent failure criteria are applied to predict failure in the adhesive joints tested in this

project and in other joints tested by other researchers. Finally, general conclusions of the project are drawn.

This document contains additionally two appendices. The first shows the dimensions and drawings of the devices developed in this project and the latter contains a list of thesis and publications related with this project.



## **I. Experiments and modeling of the behavior of adhesives**

At the beginning of the project, two types of adhesives were considered: Hysol D609 and Hysol E20HP. The first is less ductile than the latter. Another adhesive was considered during the last 2 years of the project: a polyester resin which exhibits a quasi-brittle behavior.

Tensile, compressive and torsional tests were performed so as to characterize the mechanical behavior of the adhesives. Cyclic tests were considered in order to determine the cause of eventual non linearities and quantify eventual plastic strains. The specimens tested in tension and compression were instrumented with strain gages to obtain an accurate measurement of strains.

### **1. Specimen preparation**

#### **1.1 Polyester specimens**

The polyester resin used as adhesive was made by adding a cobalt naphtate catalyst to the base resin with the ratio recommended by the supplier. The adhesive cures after 24 hours at an average room temperature of 25 °C. In order to characterize the adhesive mechanical behavior and to evaluate the effect of the hydrostatic stress, three cylindrical specimens were made with a diameter of 12.5mm to perform compression tests, and five bone-shaped specimens for the tension tests. In these last specimens, the thickness was 2.96mm and the width was 12.6mm. These last specimens were prepared with a mold made with a flat plate having the cavities where the adhesive resin was poured in. The specimens for compressive tests were prepared by pouring the adhesive in a thermoplastic tube and after extracting

them the ends were flattened in a manual lathe. In Figure 1, a picture of two specimens is shown. These specimens were instrumented with axial and transversal strain gages.

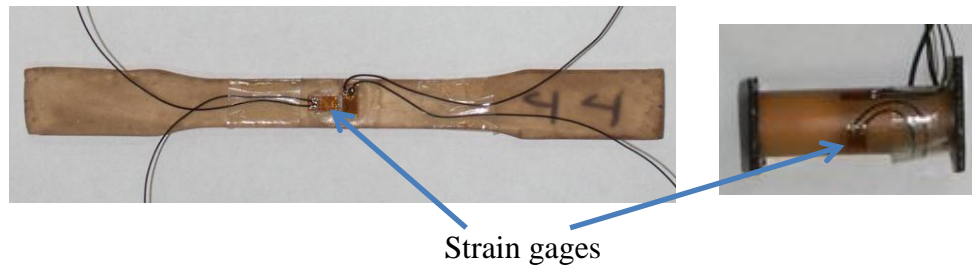


Figure 1. Polyester specimens to be tested in tension and compression

## 1.2 Hysol specimens

In order to prepare Hysol adhesive specimens, urethane molds were elaborated by making use of calibrated steel standards which dimensions may be found in the ASTM E8 standard. Then, the adhesive was poured in the molds using an application gun and a mixing nozzle. The specimens and molds were then put in a vacuum chamber during 10 minutes so as to remove the air bubbles in the uncured adhesive specimen. After this, the specimens were left curing during 24 hours at room temperature as suggested by the supplier. The specimens were tested in tension and torsion. Five diameters were initially considered: 0.11", 0.16", 0.25", 0.35" and 0.5". For tensile tests, only the three last diameters were tested whereas in torsion the three first diameters were tested.



Figure 2. Hysol specimens in molds curing in a vacuum chamber a) and specimens obtained b).

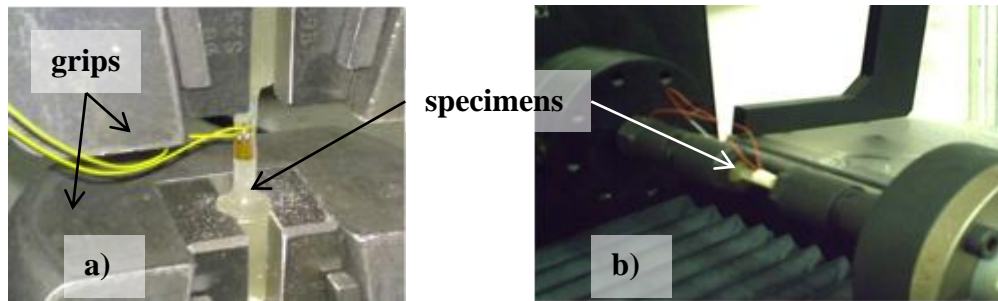


Figure 3. Hysol specimens tested in tension a) and torsion b)

## 2. Experimental results

### 2.1 Results for the polyester adhesive

In Figure 4, the axial stress  $\sigma$  and the transverse strain  $\varepsilon_t$  are plotted against the axial strain  $\varepsilon_{ax}$  for a representative polyester specimen subjected to tension and compression. In compression, the adhesive has an elastoplastic behavior that makes possible to reach higher strains than in tension. This usually happens with thermoset polymers (such as structural adhesives) with yield function and failure criterion depending on hydrostatic stress [1]. The

averages for Young's modulus  $E$ , maximum stress  $\sigma^{\max}$  and Poisson's ratio  $\nu$  obtained in the tension tests are 3.13GPa, 29.9MPa and 0.35, respectively. Five repetitions were performed for each type of test. It is possible to appreciate that, in tension the behavior is seemingly quasi linear elastic.

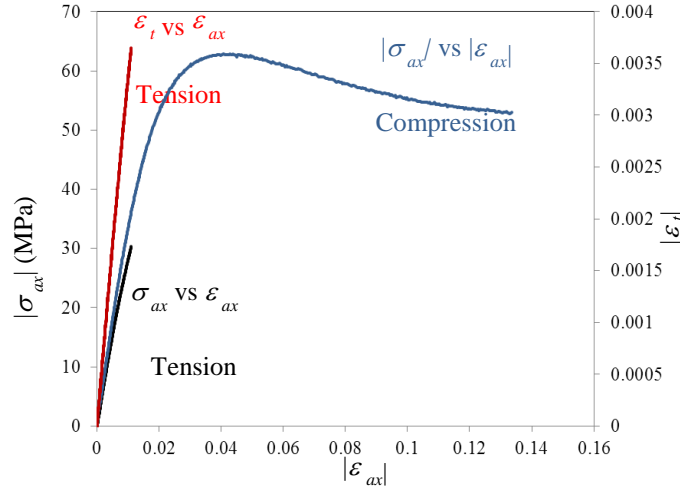


Figure 4. Axial stress  $\sigma_{ax}$  and transverse strain  $\varepsilon_t$  vs axial strain  $\varepsilon_{ax}$  for the adhesive subjected to tension and compression.

## 2.2 Results for Hysol adhesives

The tests presented in this section were performed five days after the curing process suggested by the provider has been completed. The tensile tests were carried out in an Instron Universal testing machine model 1510. The torsion tests were carried out in an Instron MT2 machine.

During the tensile tests, the strain rate was varied and the minimum strain rate assayed was 0.2%/min. At the stress levels that we have tested with different strain rates (<15MPa), no viscous phenomena were observed since the behavior didn't seem sensitive to the strain rate. For this reason, the tests were all carried out at a 0.2%/min strain rate. The obtained

stress-strain curves are similar to those shown in in Figure 5 and Figure 6 for E20HP and D609 bulk adhesives, respectively. The diameter of the specimens tested in the previous figures was 0.5". It is worth mentioning that other diameters were tested and no size effect on the behavior and strength was observed (an effect occurs usually for very brittle materials such as concrete). Figure 7 and Figure 8 display the evolution of the absolute value of the transverse strain against the axial strain for these tensile tests. The Young's modulus and the Poisson's ratio were determined from the initial slope of the stress vs. axial strain and transverse strain vs. axial strain curves, respectively. The averages obtained for these properties are listed in Table 1.

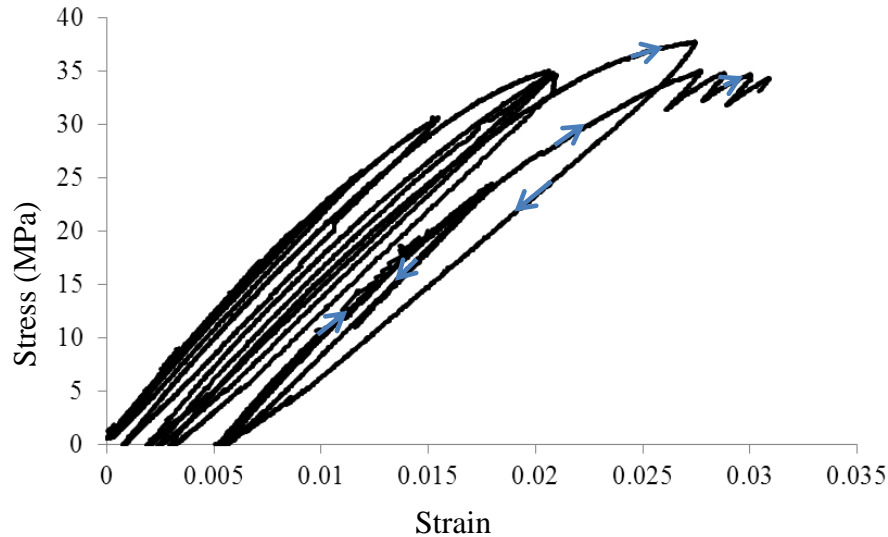


Figure 5. Stress vs. strain curve (E20HP adhesive)

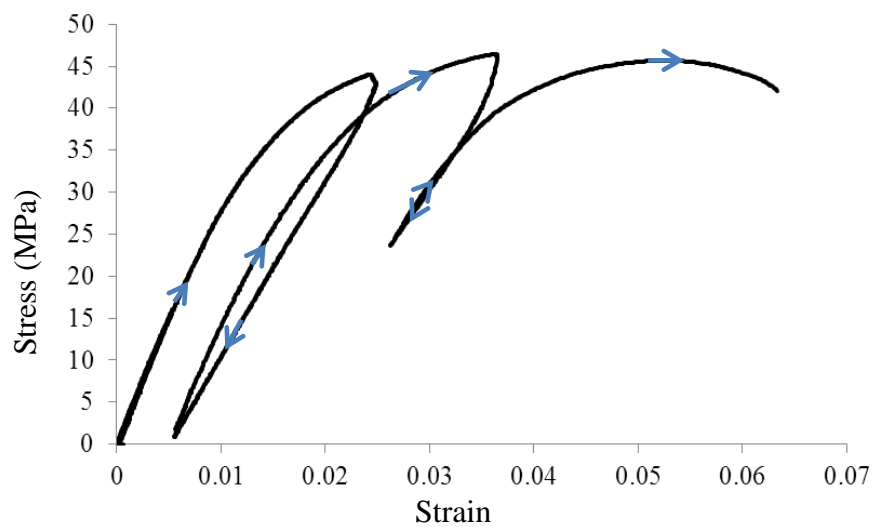


Figure 6. Stress vs. strain curve (D609 adhesive)

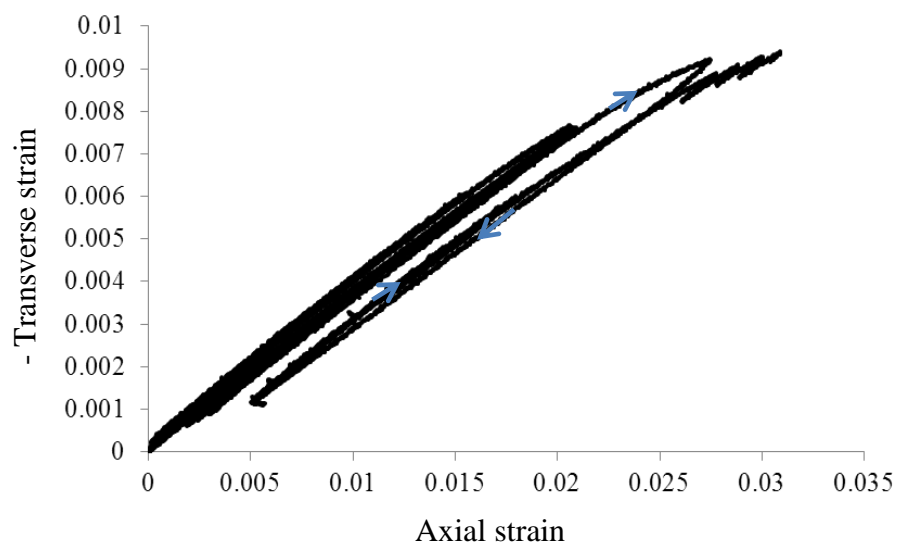


Figure 7. - Transverse strain vs. axial strain curve (E20HP adhesive)

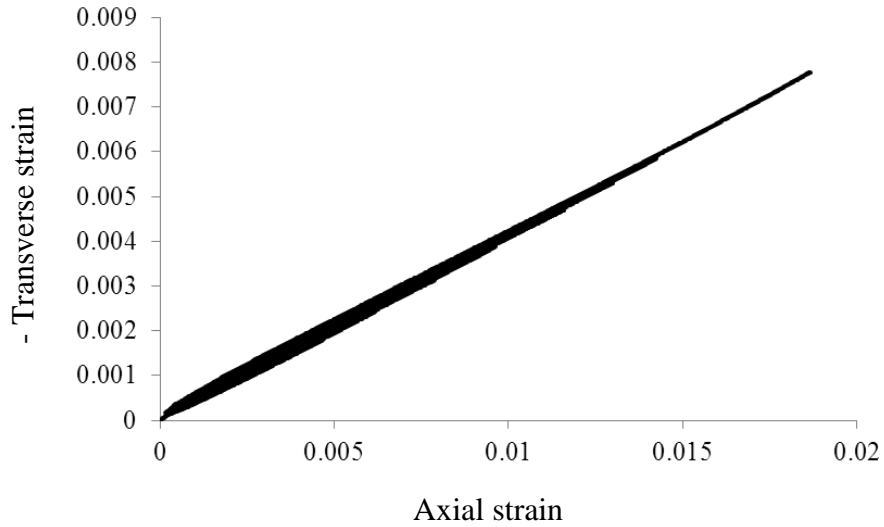


Figure 8. - Transverse strain vs. axial strain curve (D609 adhesive)

Adhesive / Property	Young's modulus	Poisson's ratio
E20HP	2.3GPa	0.38
D609	3.2GPa	0.37

Table 1. Elastic properties obtained for Hysol adhesives (tested 5 days after curing)

In Figure 9 and Figure 10, torque vs. rotation angle curves for specimens with a 0.25" diameter are shown for the E20HP and the D609 adhesives, respectively. The loading rate was 20°/min and the length of the specimen to be considered for a strain calculation is 33mm. The behavior is initially linear and then becomes non linear. Plastic strains and hysteresis loops are observed.

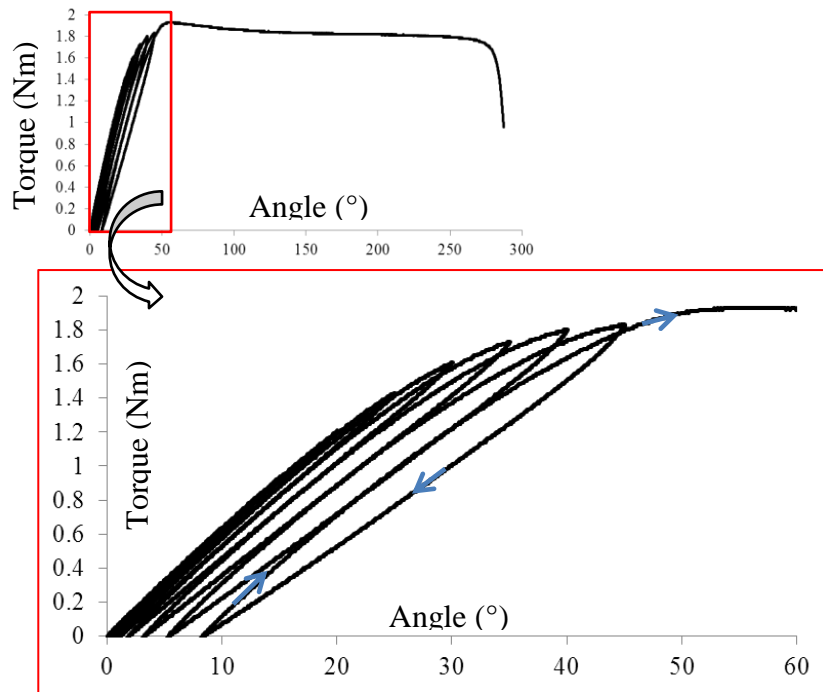


Figure 9. Torque vs. torsional angle (E20HP adhesive)

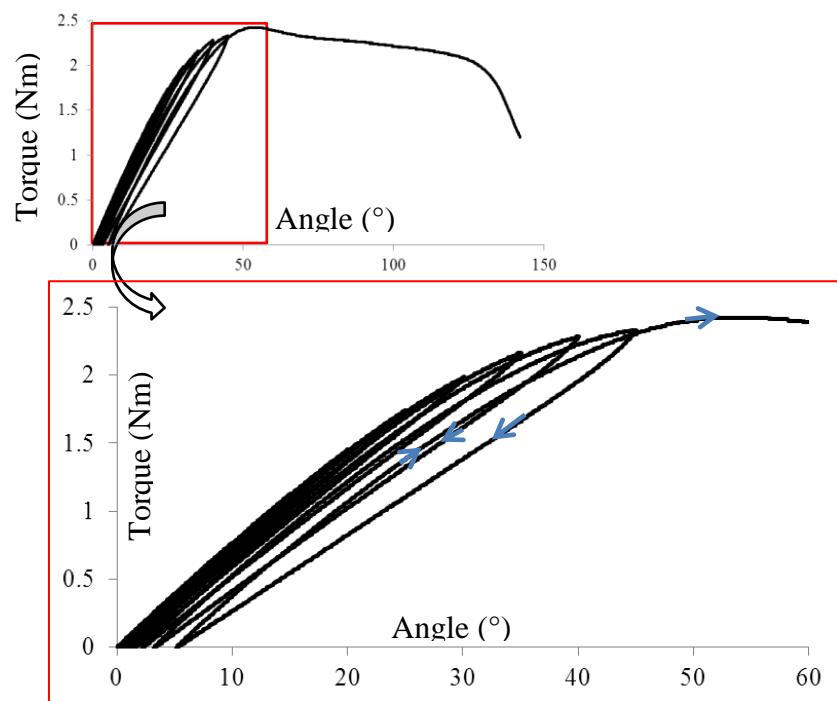


Figure 10. Torque vs. torsional angle (D609 adhesive)



### 3. Modeling

#### 3.1 Case of the polyester adhesive

In the case of the polyester resin, the behavior in tension was practically linear elastic in tension but in compression important plastic strains were observed. In order to quantify thoroughly eventual plastic strains in tension, in Figure 11, the strain  $\sigma_{ax}$  was plotted against the axial plastic strain

$$\varepsilon_{ax}^p = \varepsilon_{ax} - \frac{\sigma_{ax}}{E}. \quad (1)$$

A characteristic curve of plasticity with hardening having plastic strain magnitudes lower than 0.15% is appreciated. A correct fitting of this curve is provided by the following expression:

$$\sigma = 9.43 + 557(\varepsilon_{ax}^p)^{0.5}. \quad (2)$$

In Figure 11, the transverse plastic strain

$$\varepsilon_t^p = \varepsilon_t - \nu \frac{\sigma_{ax}}{E} \quad (3)$$

was also graphed against the axial plastic strain  $\varepsilon_{ax}^p$ . It may be seen that plastic strains  $\varepsilon_{ax}^p$  and  $\varepsilon_t^p$  are proportional. If a classic plasticity model (Von-Mises criterion, an associated plasticity and a normal flow rule) was used to predict the tensile behavior, the value  $\mu$  of the slope of the  $-\varepsilon_t^p$  vs.  $\varepsilon_{ax}^p$  curve would be equal to 0.5. The experimental value of this slope is  $\mu = 0.23$  (see Figure 11); which shows how unsuitable would be a Von-Mises type plasticity classic model. Furthermore, the difference in tension and compression behaviors shows that the use of the Von-Mises criterion would be incorrect.

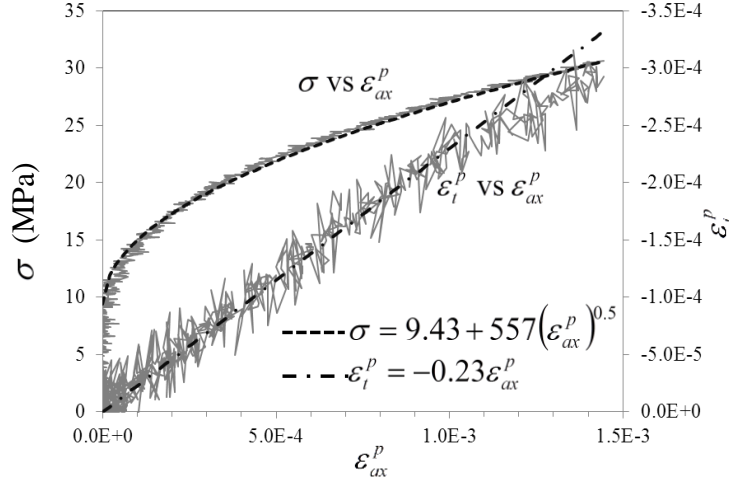


Figure 11. Stress and plastic transverse strain vs. plastic axial strain (experimental curves and theoretical fitting)

In order to predict accurately the stresses in an adhesive joint, a model of plasticity is required. Since the adhesive behavior is very sensitive to the hydrostatic stress, a Drucker-Prager type criterion is adopted:

$$f(\boldsymbol{\sigma}) = \sigma^{eq} + 3\alpha\sigma^h - \sigma^0 - R(p) \quad (4)$$

where  $\boldsymbol{\sigma}$ ,  $\sigma^{eq}$ ,  $\sigma^h$ ,  $\alpha$ ,  $\sigma^0$ ,  $p$  and  $R(p)$  are the stress tensor, the Von-Mises stress, the hydrostatic stress, a constant material property, the initial yield stress, the cumulative plastic strain and the hardening function, respectively. If the associated plasticity hypothesis and a normal flow rule are adopted, it is easily shown that a constant  $\alpha$  in the plasticity criterion is related to the slope  $\mu$  of the  $-\varepsilon_t^p$  vs.  $\varepsilon_{ax}^p$  curve in a tensile test by means of the following equation:

$$\alpha = \frac{-\mu + 0.5}{1 + \mu}. \quad (5)$$

Therefore, the value of  $\alpha = 0.22$  is obtained. In the other hand, since

$$p = \frac{\varepsilon_{ax}^p}{\alpha + 1} \quad (6)$$

for a tensile test, equations (2) and (4) yield  $\sigma^0 = 11.5 \text{ MPa}$  and  $R(p) = Kp^\gamma$ , where  $K = 750 \text{ MPa}$  and  $\gamma = 0.5$ . In this way, we already have the parameters required for simulating the elastoplastic behavior of the adhesive in the adhesive joints.

### 3.2 Case of Hysol adhesives

Herein the case of the structural adhesives D609 and E20HP is analyzed. Let us consider an unloading after a loading phase that has caused plasticity. Practically, at the very beginning of the unload phase, the slope seems to be the same as that in the linear elastic range at the beginning of the test (see from Figure 12 to Figure 15). This happens even for different loading rates. The same happens at the beginning of a reloading as shown in the figures mentioned above. For this reason, we thought that no viscoplasticity occurred. In fact, in all the viscoplastic theories reviewed a greater slope would be expected since the viscoplastic phenomena are still active at the beginning of the unloading stage. In these theories, the only thing that would explain this is that the load rate is very small. Then, a classical elastoplastic model would suffice to model the stress strain behavior.

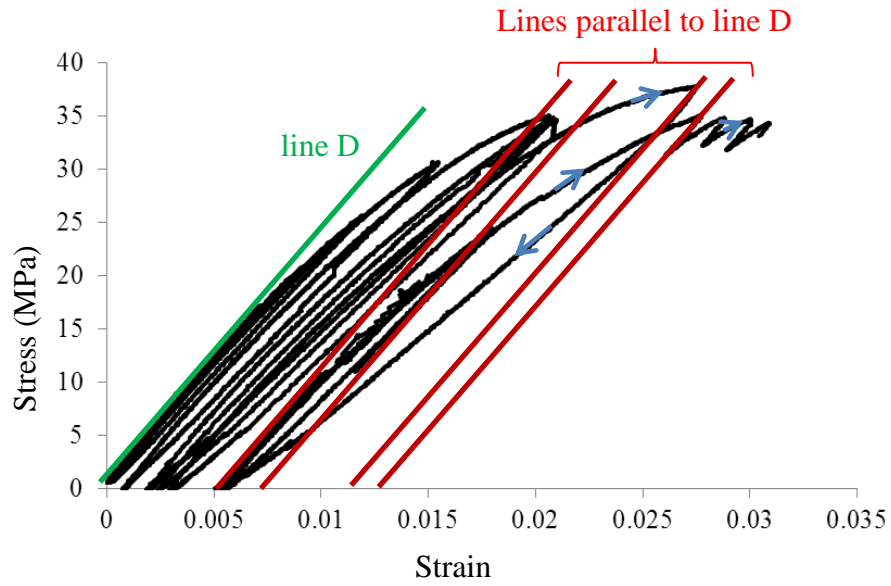


Figure 12. Stress vs. strain curve and lines to analyze the behavior (E20HP adhesive)

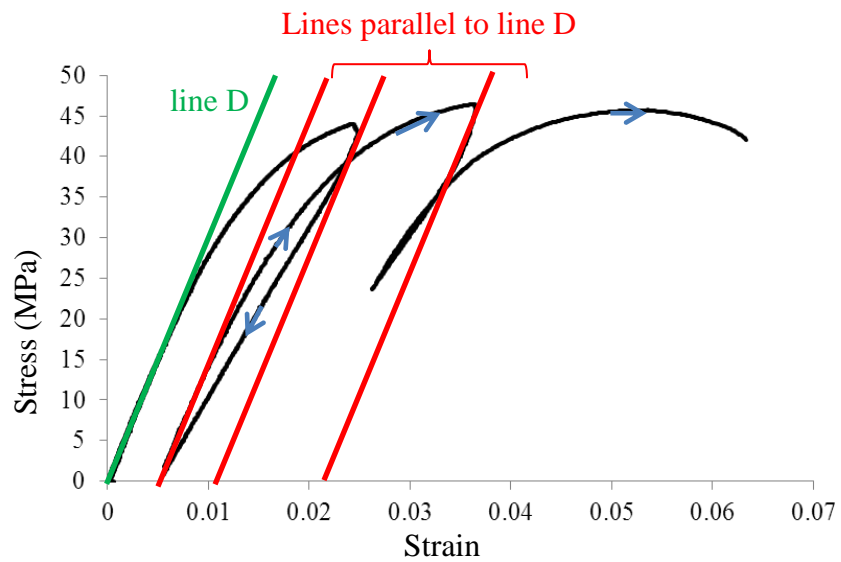


Figure 13. Stress vs. strain curve and lines to analyze the behavior (D609 adhesive)

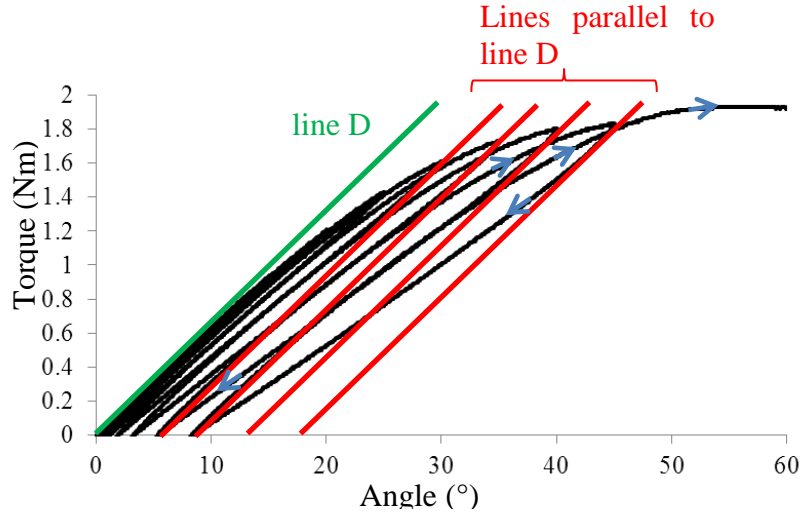


Figure 14. Torque vs. torsional angle and lines to analyze the behavior (E20HP adhesive)

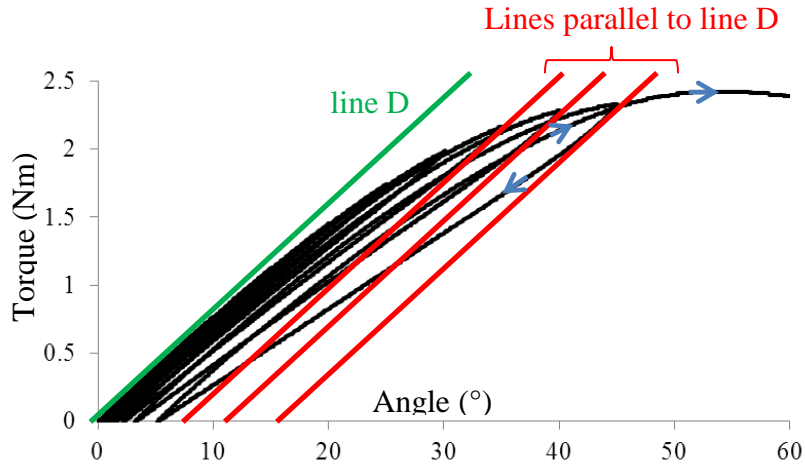


Figure 15. Torque vs. torsional angle and lines to analyze the behavior (D609 adhesive)

An isotropic hardening is not observed and the apparent elastic zone is not centered on the zero stress axis. Besides, a kind of hardening seems to appear and saturate as the strain increases. Therefore an elastoplastic model with nonlinear kinematic hardening [2] for both adhesives was proposed. The equations of the model are:

- Linear elastic constitutive equation:

$$\sigma_{ij} = \frac{E}{1+\nu}(\varepsilon_{ij} - \varepsilon_{ij}^p) + \frac{\nu E}{(1+\nu)(1-2\nu)}(\varepsilon_{kk} - \varepsilon_{kk}^p)\delta_{ij} \quad (7)$$

where  $E$  and  $\nu$  are the Young's modulus and the Poisson's ratio, respectively;  $\boldsymbol{\sigma}$ ,  $\boldsymbol{\varepsilon}$  and  $\boldsymbol{\varepsilon}^p$  are the stress, strain and plastic strain tensors;  $\delta$  is the Kronecker delta function.

- Yield function:

$$f(\boldsymbol{\sigma}, \mathbf{X}) = \left( \frac{3}{2} \sum_{1 \leq i, j \leq 3} (\sigma_{ij}^d - X_{ij}^d)^2 \right)^{1/2} - \sigma^y \quad (8)$$

where  $\sigma^y$  is the yield stress,  $\mathbf{X}$  is the kinematic hardening stress, the superscript  $d$  stands for the deviatoric part of a tensor.

- Normal flow rule

$$\dot{\varepsilon}_{ij}^p = \dot{p} \frac{\partial f}{\partial \sigma_{ij}} \quad (9)$$

where  $p$  is the cumulative plastic strain

- Kinematic hardening rule

$$\dot{X}_{ij}^d = \gamma \left( \frac{2}{3} X_{\infty}^d \dot{\varepsilon}_{ij}^p - X_{ij}^d \dot{p} \right) \quad (10)$$

where  $\gamma$  and  $X_{\infty}$  are constants.

The constants appearing in the model for each adhesive are listed in Table 2. The predictions for the cyclic tensile tests with a same strain rate were correct as shown in Figure 16 and Figure 17 for the E20HP and D609 adhesives, respectively. The ratcheting phenomenon is predicted.

Adhesive	$\sigma^y$ (MPa)	$\gamma$	$X_{\infty}$ (MPa)
E20HP	10	490	28
D609	10	170	40

Table 2. Properties of the Hysol adhesives according to a plasticity model with nonlinear kinematic hardening.

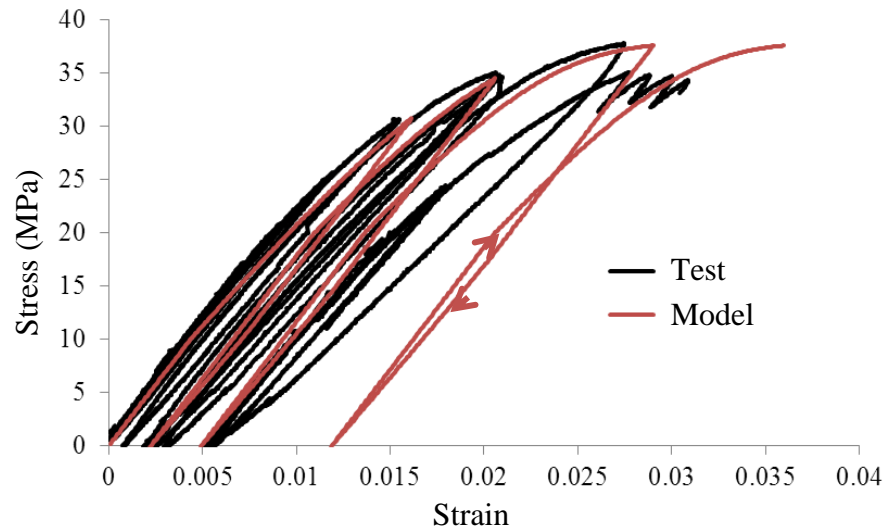


Figure 16. Predicted and experimental stress vs. strain curve (E20HP adhesive)

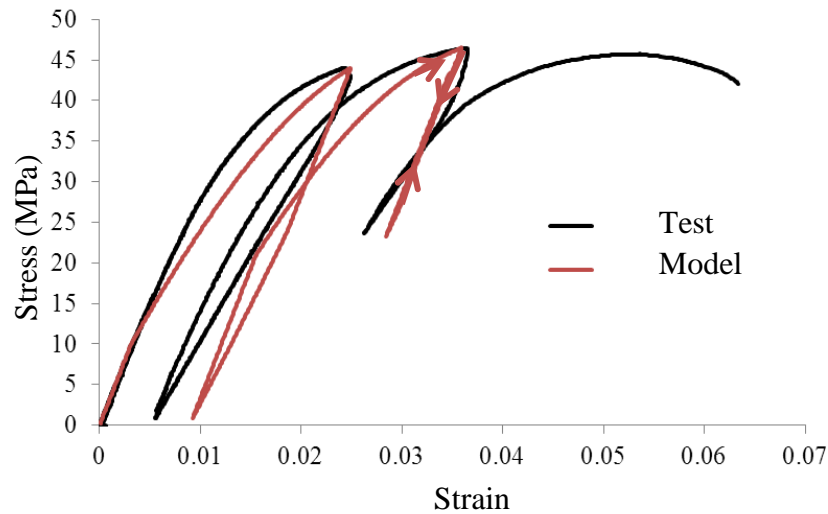


Figure 17. Predicted and experimental stress vs. strain curve (D609 adhesive)

The model was then applied to the prediction of the behavior of specimens subjected to torsion. The model didn't provide accurate predictions for every specimen size. Other yield functions such as a Drucker-Prager-like function were assayed but the predictions were not accurate for different diameters [3].

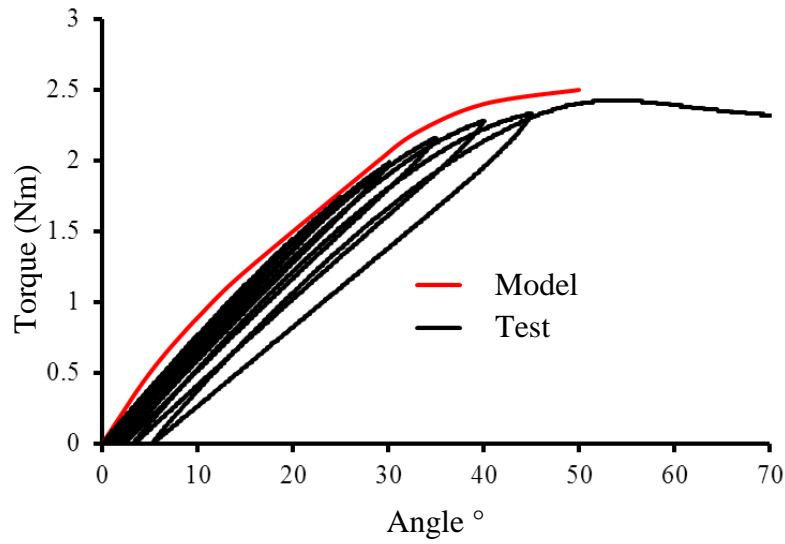


Figure 18. Predicted and experimental torque vs. angle curve (D609 adhesive, 0.25" diameter)

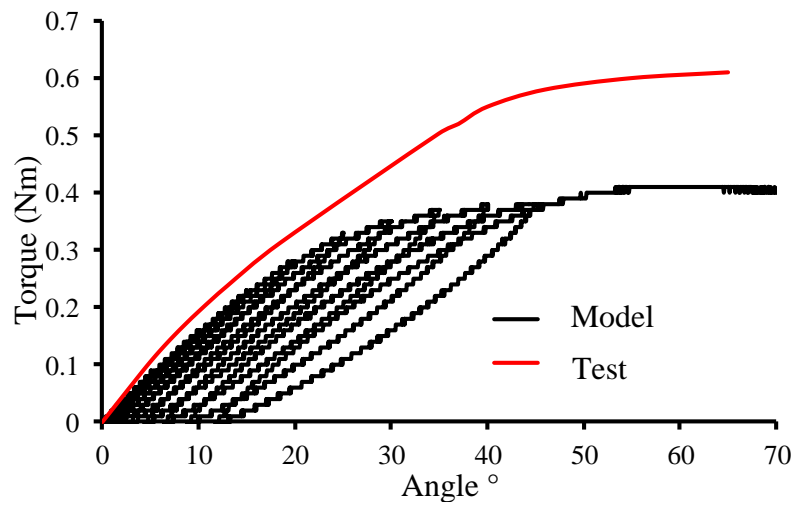


Figure 19. Predicted and experimental torque vs. angle curve (D609 adhesive, 0.16" diameter)

Besides the previous shortcoming of the model, we observed that



- *The constants appearing in the model have to be readjusted if the load rate is varied or if the elapsed time from curing to testing is not the same (the mechanical properties of the adhesive are not stable).*
- *Once the behavior is non-linear, if the strain is fixed, the stress decreases (stress relaxation). This implies that viscous phenomena really occur.*

The tasks required to understand the problems described above and the development of a new model need an extra budget. New adhesives and a better machine than the Instron Universal testing machine model 1510 are needed. This old machine has an obsolete software which is not able to make cyclic tests and stress controlled tests. The cyclic tensile tests carried out in this project were controlled manually. Fortunately, from another project started on 2012, we bought new adhesives and a better Instron machine (model 3382) so as to carry out stress controlled tests and automated cyclic tests. In the following section, the current work to develop a correct modeling of Hysol adhesives is described.

#### **4. Current work to obtain a correct modeling of Hysol adhesives**

As mentioned above, the mechanical properties of the adhesives cured as proposed by the provider are not stable and this may be due to a bad control of adhesive curing. Besides, new mechanical tests are required to develop a more predictive model. A model that predicts accurately the behavior of the adhesive has not been reported yet. Cognard et al. mention continuously the necessity of such a model [4], [5], [6]. Some models are available in literature but are not validated by comparing its results to cyclic tests with different strain rates [7], [8].

## 4.1 Adhesive curing

Recently, a paper published by Cognard provided us a hint regarding the instability of the mechanical properties of adhesives. Those adhesives which may cure at room temperature may require an additional heat treatment (not specified by the provider) so as to ensure a quasi-complete curing of the adhesive [9], [4]. A determination of the glass transition temperature  $T_g$  of the D609 adhesive was performed by a TGA-DSC device. In Figure 20, the obtained curve by the DSC device (blue curve) shows that  $T_g$  for this adhesive is  $45^{\circ}\text{C}$  and the TGA (red curve) provides the degradation temperature  $T_d=184^{\circ}\text{C}$ . As proposed by Cognard, a heat treatment at a temperature above  $T_g+20^{\circ}\text{C}$  should ensure a quasi-complete curing. The steps of the heat treatment proposed for the D609 are then:

1. 24 hours at room temperature (proposed by the provider)
2. 36 hours at a  $65^{\circ}\text{C}$  temperature
3. 4 hours at a  $40^{\circ}\text{C}$  temperature so as to cause a smooth cooling of adhesive joint specimens.

In order to prove that the mechanical properties of the adhesive are stable after this treatment, a DMA analysis was performed varying the temperature at a 1Hz frequency with a small strain amplitude (0.05%) so as to avoid plasticity. In Figure 21, the elastic modulus and temperature are plotted against time for untreated and treated specimens. One may observe that the treated specimen exhibits stable mechanical properties after a temperature cycle whereas the untreated specimen does not have the same mechanical properties after a temperature cycle. This is surely due to curing reactions that take place in the untreated specimen. One would expect a growth of the elastic modulus after a heating cycle in the untreated specimen because curing advances. Nevertheless, the measured elastic modulus decreases, this may be due to a damage process in the untreated specimen. In fact, the untreated specimen exhibited an important plastic deflection whereas the treated specimen didn't. The instability of the mechanical properties of the untreated specimen is the cause of the important variations of the behavior of the adhesives when the time elapsed after curing is not controlled. A measurement of the  $T_g$  and a heat treatment proposal has not been performed yet for the E20HP adhesive. This task will be performed during 2012.

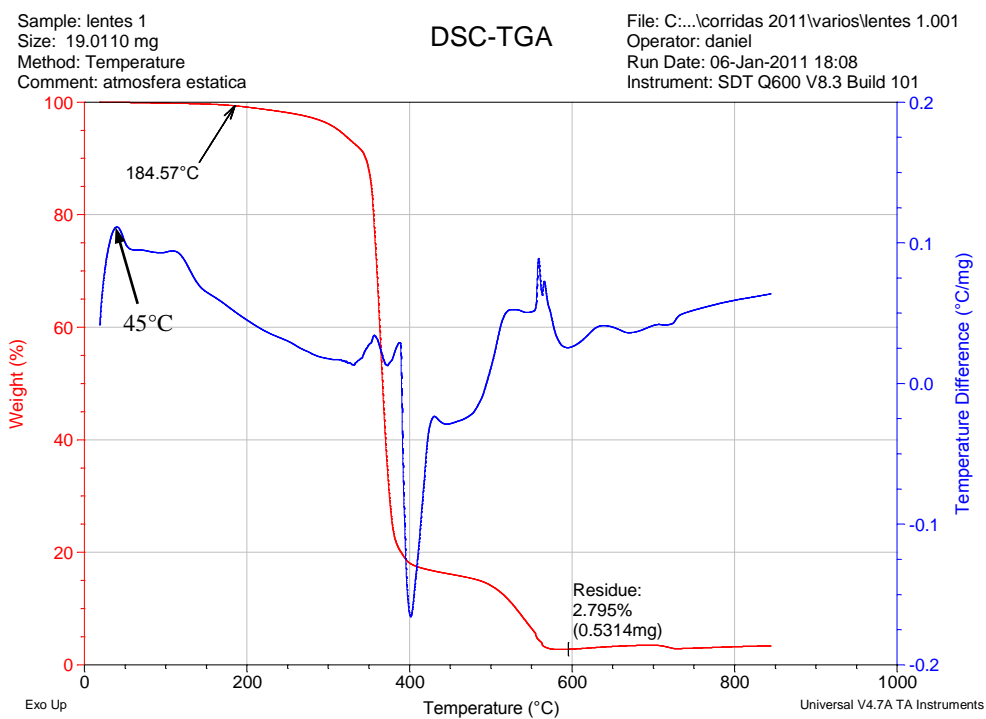


Figure 20. TGA performed to a D609 sample (cured as suggested by the provider)

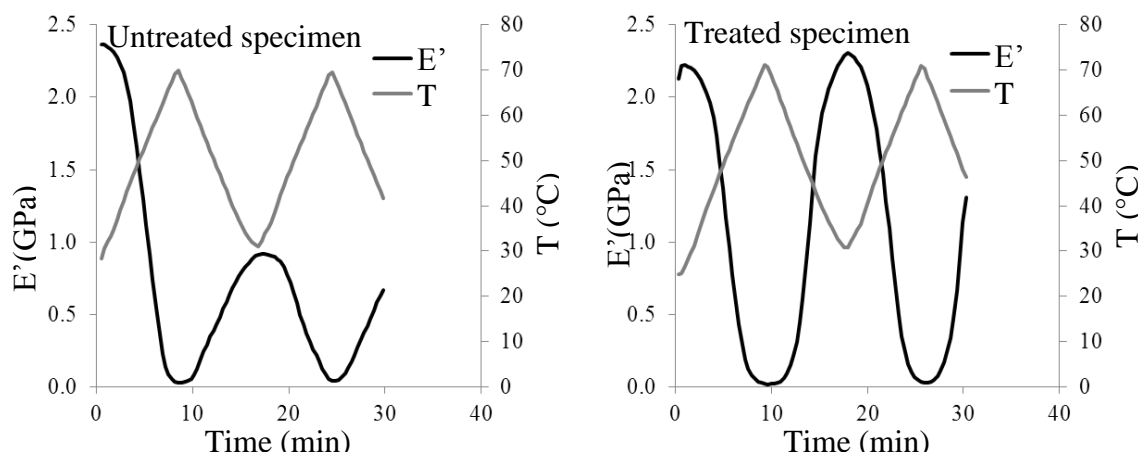


Figure 21. Elastic modulus ( $E'$ ) and temperature ( $T$ ) for untreated and treated D609 samples (DMA).

## 4.2 Viscoplastic model

The tensile tests shown in this subsection were carried out in the new Instron machine (model 3382) with D609 specimens cured and treated with the heat treatment proposed in the previous subsection so as to ensure a quasi-complete curing of the adhesive and stable mechanical properties. The specimens have a  $\frac{1}{4}$ " diameter.

In Figure 22, the stress-strain curves obtained for a tensile test with a 0.04%/min strain rate and a multicroep test with a 2%/min strain rate for each loading are shown. The steps with a horizontal slope for the multicroep test correspond to a 10 min constant stress. Once the stresses are greater than 10MPa, an important effect of the strain rate is observed. The initial slope does not depend on the strain rate. For these reasons, one may affirm that a viscoplastic phenomenon occurs.

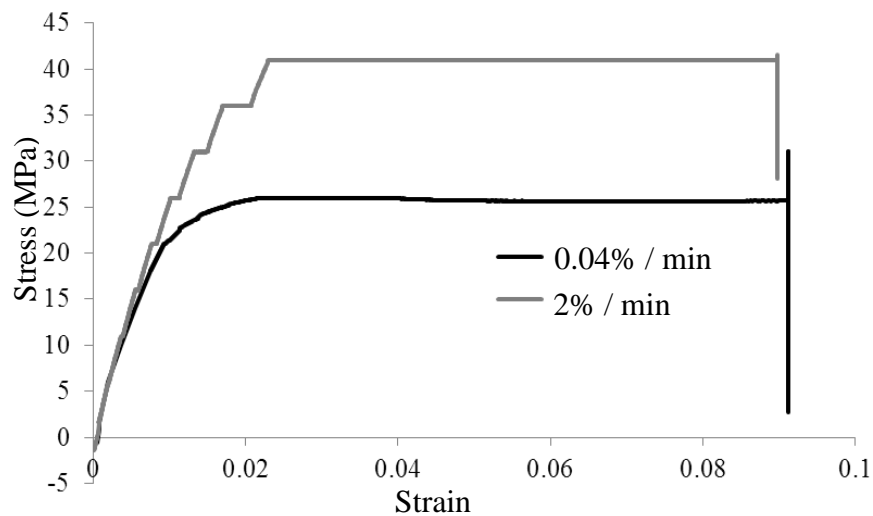


Figure 22. Stress-strain curves with different strain rates (D609 adhesive).

Creep tests were then carried out with different stress levels: 30, 32.5, 35, 37.5 and 40MPa. The tests were stress controlled and the stress rate applied was 100MPa/min before maintaining the stress constant. In Figure 23, the strain evolution for these creep tests is shown. The time origin was taken at the beginning of the stage where the stress is maintained constant. The curves in Figure 23 are classical curves of viscoplasticity. A first stage has a nonlinear evolution of the plastic strain, then a linear part with a constant plastic strain rate is observed and finally a nonlinear evolution is observed due to an important damage growth.

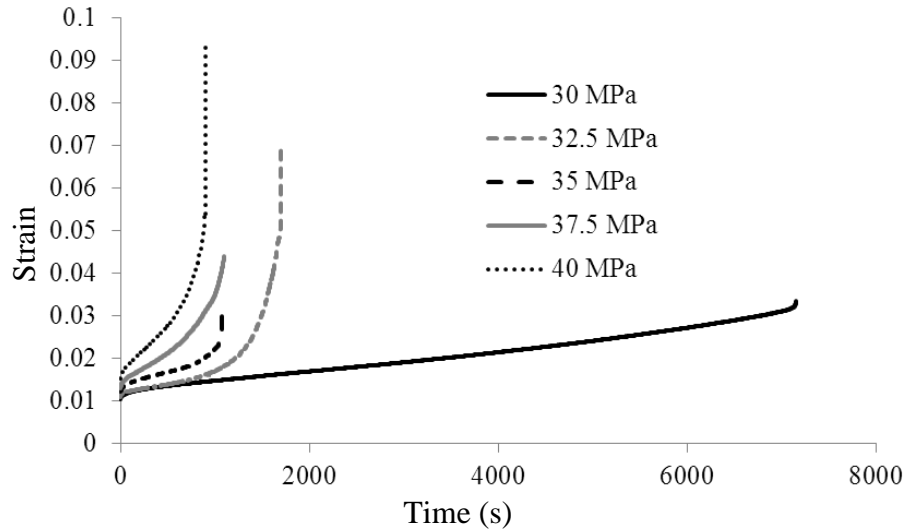


Figure 23. Strain vs. time for creep tests with different stress levels (D609 adhesive)

Taking into account the observed phenomena in Figure 22 and the slopes of the constant strain rate stages of the creep tests in Figure 23, a preliminary 1D model was proposed for the adhesive:

- Linear elastic constitutive equation:

$$\sigma = E(\varepsilon - \varepsilon^p) \quad (11)$$

where  $E$  is the Young's modulus;  $\sigma$ ,  $\varepsilon$  and  $\varepsilon^p$  are the stress, strain and plastic strain.

- Yield function:

$$f(\sigma, X) = |\sigma - X| - \sigma^y \quad (12)$$

where  $\sigma^y$  is the yield stress,  $X$  is the kinematic hardening stress.

- Odqvist's law:

$$\dot{\varepsilon}^p = \left( \frac{f(\sigma, X)}{K} \right)^N \text{ if } f(\sigma, X) \geq 0 \quad (13)$$

where  $K$  and  $N$  are material parameters defining the viscoplastic behavior

- Kinematic hardening rule

$$\dot{X} = -\gamma \dot{\varepsilon}^p \left( \frac{\dot{\varepsilon}^p}{|\dot{\varepsilon}^p|} X - X_\infty \right) \quad (14)$$

where  $\gamma$  and  $X_\infty$  are constants.

The constants appearing in the model above are identified by means of the experimental results exhibited in Figure 22 and Figure 23:  $E = 3.4\text{GPa}$ ,  $\nu = 0.33$ ,  $\sigma^y = 1\text{MPa}$ ,  $\gamma = 200$ ,  $X_\infty = 24\text{MPa}$ ,  $K = 2000\text{MPas}^{1/N}$  and  $N = 2.11$ . The model equations were programmed in MATLAB in order to predict the behavior of the adhesive for any type of 1D loading.

Once the model parameters were identified, another mechanical test was performed to test the accuracy of the model predictions. A stress controlled cyclic test was carried out at a 1MPa/min rate; the obtained stress-strain curve is shown at the left hand side in Figure 24. The model predictions are shown at the right hand side in the previous Figure. The model predictions are globally correct but the unloading predictions are not accurate enough since it seems that a kind of damage occurs because the slopes of the tangents in the experimental curve seem to decrease.

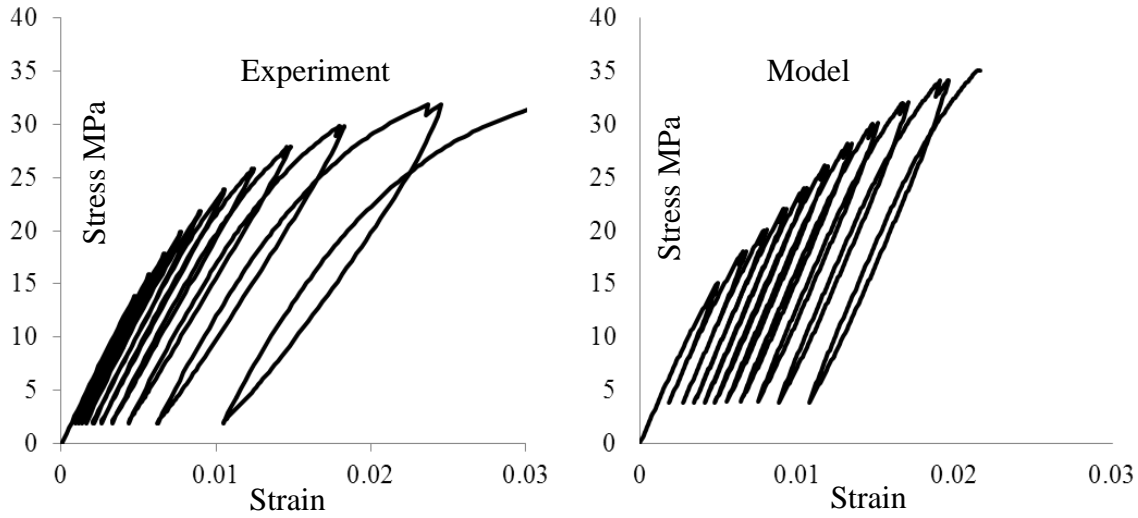


Figure 24. Stress-strain curves for a cyclic tensile test: experiment and viscoplastic predictions (D609 adhesive)

In order to prove that damage occurs, a multicreep cyclic test was performed. In Figure 25, the schematic plot of the stress vs. time programmed in the Instron machine is shown. In all, 6 unloadings were performed. The loading and unloading was performed at a 30MPa/min rate so as to avoid the evolution of the plastic strains during these stages. In Figure 26, the stress-strain curve for the multicreep test is shown. The plastic strain evolves mainly during the stages where the stress is fixed. For high level stresses the plastic strain increases but for low level stresses it decreases. Let us analyze the first unloading (see Figure 27). The plastic strain increases for stress levels greater than 18MPa and decreases for stress levels smaller than 10MPa. For the stage when the stress is 14MPa, an increase or decrease of the plastic strain is not obvious. The elastic zone in this unloading lies within the [10MPa,18MPa] interval. An approximation of the apparent Young's modulus  $E=3.44\text{GPa}$  in this unloading was thus calculated by making use of the slope of the stress-strain curve in the previous interval. The damage parameter is then defined by  $d = \frac{E^0 - E}{E^0}$ ,

where  $E^0 = 3.69\text{GPa}$  is the Young's modulus of the undamaged material calculated with the slope of the stress-strain curve at the beginning of the first loading. The damage parameter for the first unloading is then 0.069. In a similar manner, the apparent Young's

modulus and the damage parameter were calculated for the other unloadings and both were plotted in Figure 28 against the number of the unloading. It is clear that damage occurs and that it increases as the plastic strain grows.

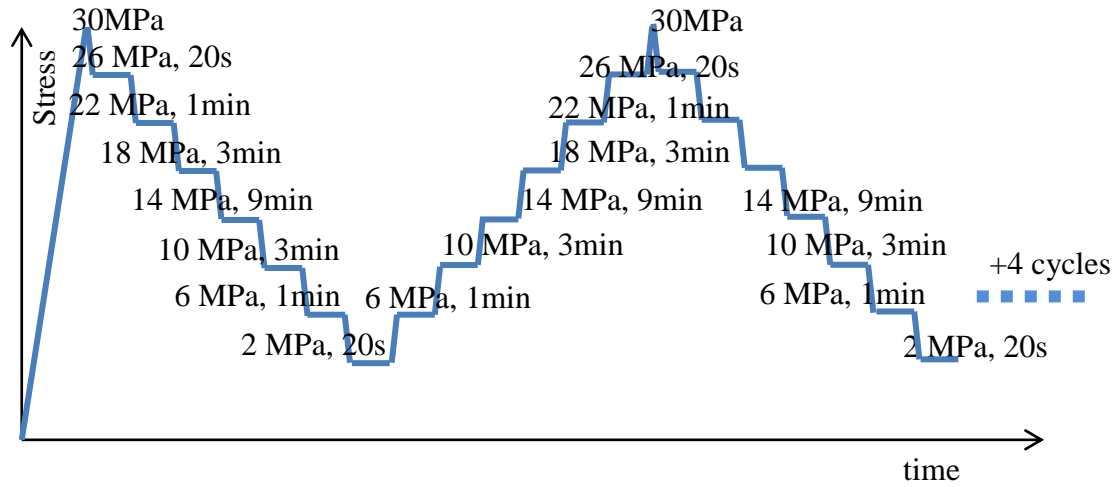


Figure 25. Schematic plot of stress vs. time for a multicreep test.

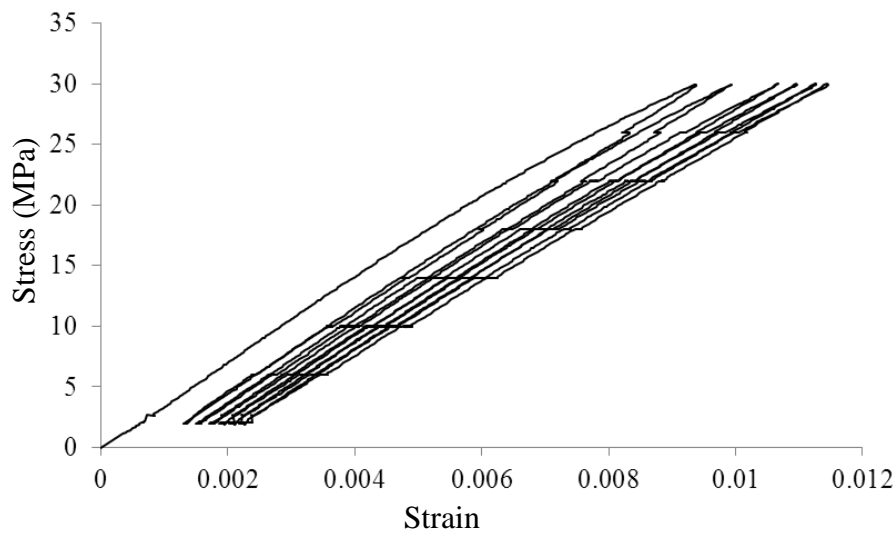


Figure 26. Stress –strain curve obtained in the multicreep test (D609 adhesive).



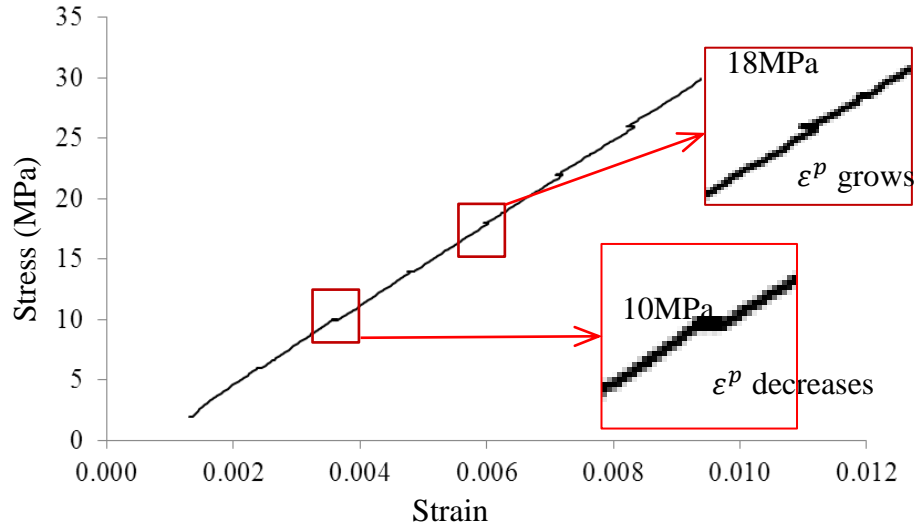


Figure 27. Analysis of the first unloading in the multicroep test.

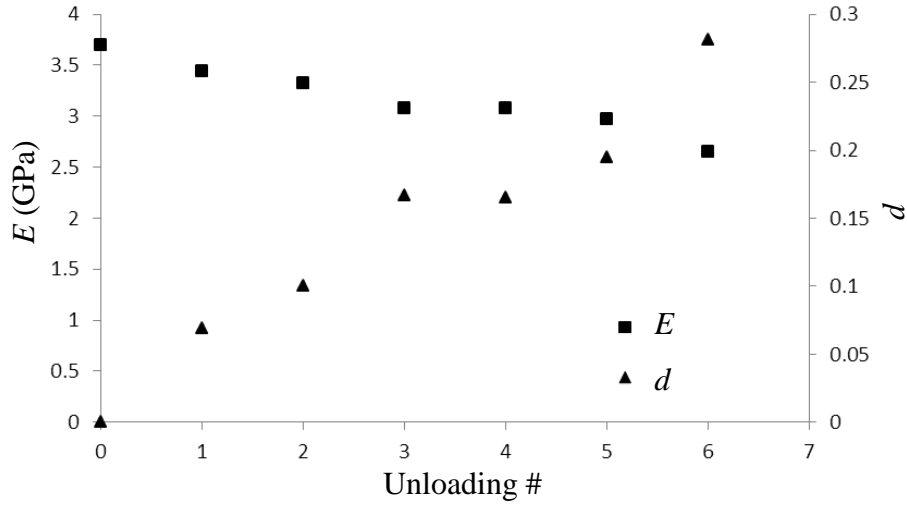


Figure 28. Apparent Young's modulus  $E$  and damage parameter  $d$  calculated at each unloading.

The development of a model involving damage and viscoplasticity is the purpose of a PhD thesis started at CIMAV on January 2012. Once the model will be validated for uniaxial tests, a 3D constitutive model will be proposed and validated by comparing its predictions

to different multiaxial tests such as torsion and flexion. This model will be obtained by July 2013.

## **5. Conclusions**

Three adhesives were analyzed: polyester, D609 and E20HP. The polyester exhibited a quasi linear elastic behavior before failure onset. Hysol D609 and E20HP adhesives exhibited a complex behavior which couldn't be understood and analyzed with the devices considered at the beginning of the project in spite the several efforts and models applied to predict their behavior. Besides the curing process proposed by the provider is not the best choice since instable mechanical properties are obtained for Hysol adhesives. New testing machine and adhesives were bought on 2012 so as to perform a correct analysis of the behavior of these adhesives. A PhD student is currently studying the curing process and the behavior of these Hysol adhesives. Today, the main findings for these Hysol adhesives are:

- a heat treatment is required to ensure a quasi-complete curing. A heat treatment has been proposed in section 4 of this chapter for the D609 adhesive. This treatment was validated with a Dynamical Mechanical Analysis with a temperature variation.
- a viscoplastic phenomenon with kinematic hardening and damage is observed. A preliminary model involving viscoplasticity with a nonlinear kinematic hardening without damage has been proposed and its predictions are globally correct but it is not accurate enough to predict important stiffness losses due to damage.

The model that will be developed must predict failure accurately. Today, we are not able to predict the adhesive failure when different loading rates and multiaxial loads are applied.

## II. Adhesive joint experiments

In this chapter, mechanical tests with adhesive joints are proposed to provoke their failure in different stress state conditions. The results of these tests will be applied on chapter IV to propose failure criteria.

### 1. Tests description and specimen preparation

Two types of metallic substrates were considered: 1018 steel and aluminum. The mechanical properties of these materials were obtained by means of 3 tensile tests. For the steel considered, the averages for Young's modulus, maximum stress and Poisson's ratio obtained in the tension tests are  $E = 181\text{GPa}$ ,  $\sigma^{\max} = 120\text{MPa}$  and  $\nu = 0.33$ , respectively. For the aluminum considered, the averages obtained were:  $E = 70\text{GPa}$ ,  $\sigma^{\max} = 35\text{MPa}$  and  $\nu = 0.33$ . All the surfaces of the substrates were sandblasted (the obtained roughness was  $R_a = 2\mu\text{m}$ ) and cleaned with acetone.

#### 1.1 Joints bonded with the polyester adhesive

In this case, three different types of tests were carried out to submit the interfaces to different normal stress - shear stress ratios. The tests are shown in Figure 29 and are named as follows:

- Type A: "Torsion-Tension" tests with butt joint specimens,
- Type B: Tension tests with double lap joints,
- Type C: Peeling tests with double lap joints.

In Figure 29, the specimen dimensions are specified. The adhesive thickness in all the samples was constant and equal to 0.5 mm. For the adhesive length  $l$  in type B and C specimens, three values were used: 10 mm, 15 mm, and 20 mm. It is worth telling that for type B specimens, only the adhesive length varied in one joint end with the abovementioned values, the adhesive length in the other end remained the same, equal to 30 mm.

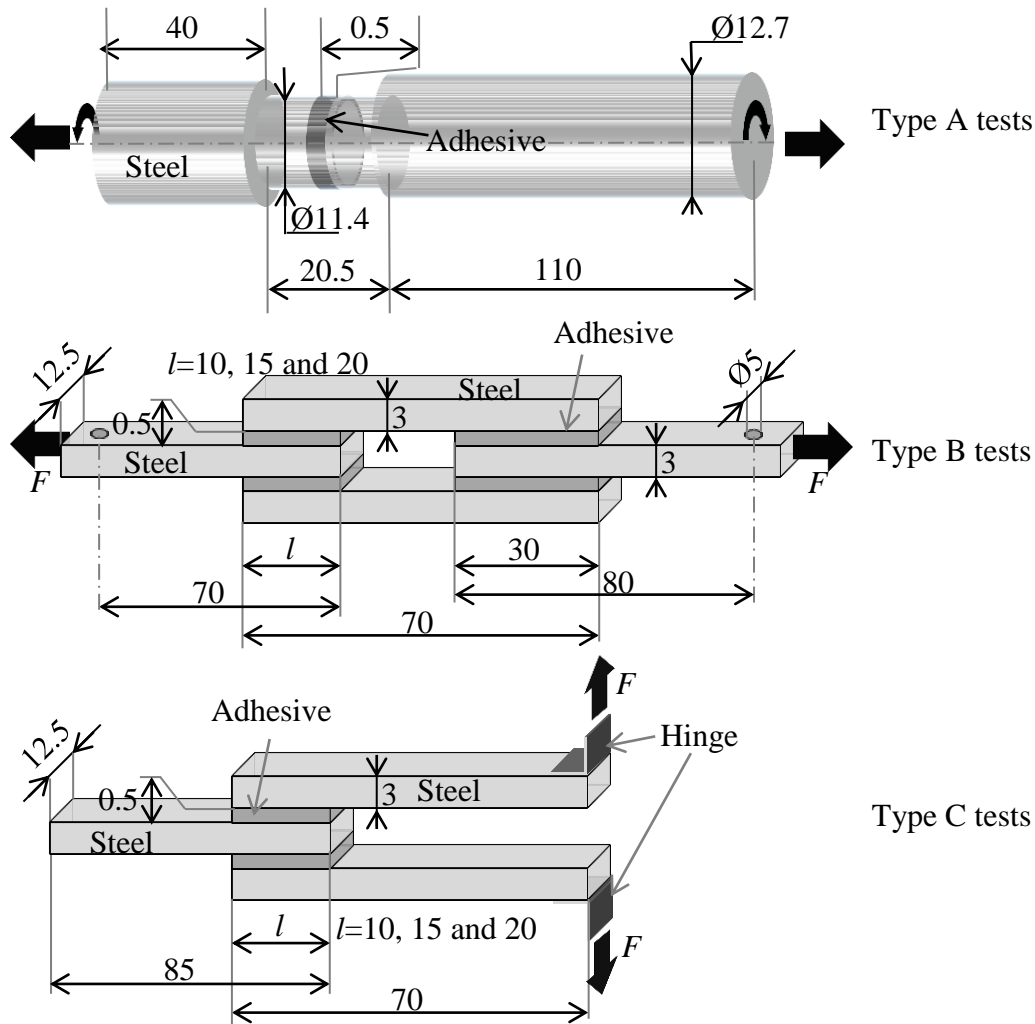


Figure 29. Joint specimens bonded with polyester and dimensions in mm

Type A specimens consist of two coaxial steel cylindrical pieces. For every pair of coaxial metallic pieces, half an urethane slip coupling was inserted in the upper end of the lower piece and the resin was poured into the cavity formed by the upper half of the coupling (see Figure 30). Afterwards, the upper metallic piece was slipped into the coupling leaving the desired adhesive thickness. The correct adhesive thickness was assured by means of stops in the specimen ends. For the construction of specimens B and C, urethane molds were made (see Figure 30) thanks to machined and calibrated standards. The surfaces of the substrates of all the 3 types of specimens were treated with a sandblasting technique for them to have a flat surface and the same roughness in all the tests (the roughness was  $R_a = 2\mu\text{m}$ ). In every case, the surfaces were cleaned with acetone and left drying to apply the adhesive subsequently.

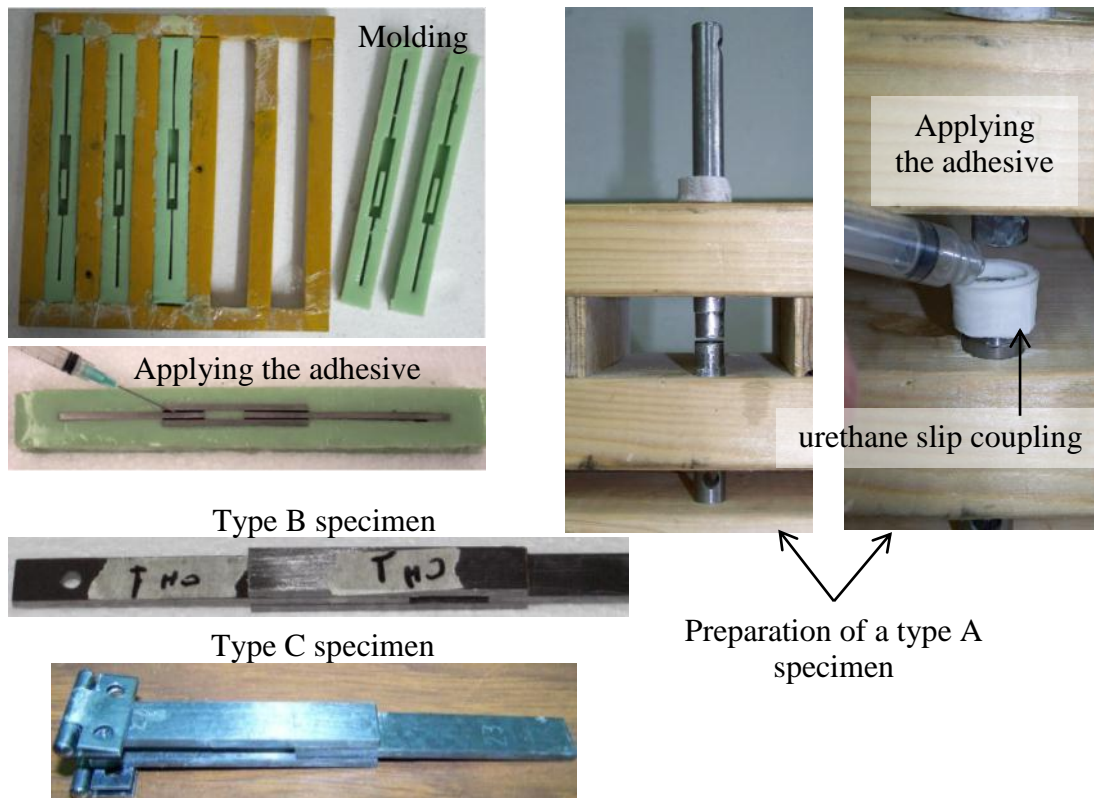


Figure 30. Preparation of adhesive joint specimens.

For type A specimens, a tensile load  $F$  is first applied and then the torque  $T$  is increased at a rate of approximately 1 Nm/min. In Figure 31, a picture of the device used for these tests is shown. The tests of type B and C specimens were carried out in a universal testing machine and the displacement rate was 0.1 mm/min. The load in type B specimens was transmitted with pins so as to prevent transmission of parasite moments.

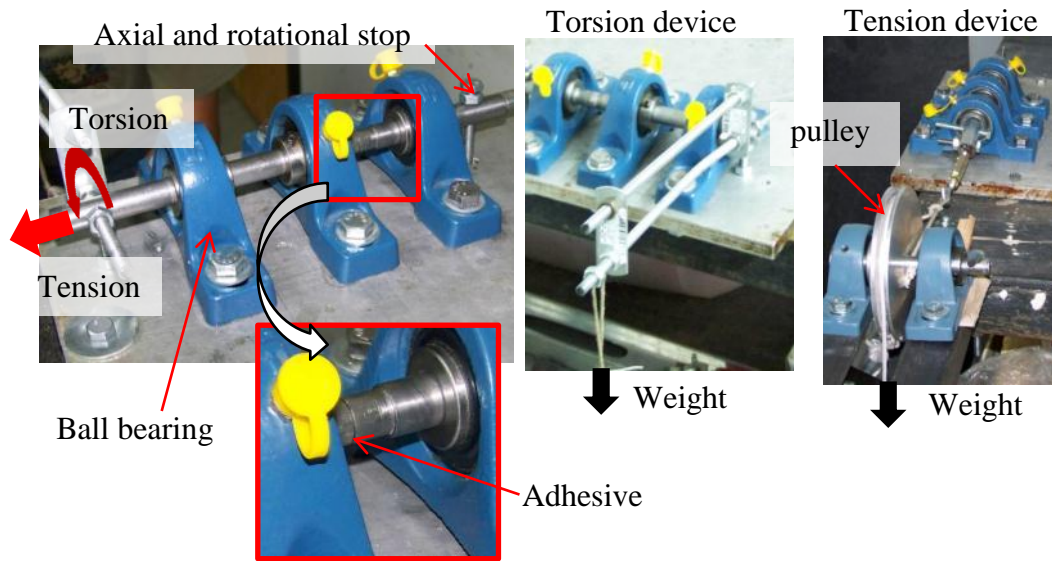


Figure 31. Experimental device used to perform type A tests

## 1.2 Joints bonded with Hysol adhesives

The tests considered in this subsection are named as follows:

- Type D tests: ARCAN tests without edge effects (see Figure 32 and Figure 33). A thorough description of the ARCAN tests may be found in [9]. In these tests the interfaces of the adhesive joint may be subjected to different ratios of peel stress / shear stress. These ratios depend on the angle  $\alpha$  considered to apply the load (see Figure 32). Type D specimens do not have a flat shape at the edges near the interfaces (see Figure 33) in order to avoid edge effects on stresses and to ensure

that stresses are virtually uniform in the adhesive and at the interfaces. The dimensions of specimens D are provided in appendix 1. The area of the adhesion surface is 69mm×14mm. The adhesive thickness is 0.5 mm. The specimens are made with a 1018 steel and the D609 adhesive. Seven values of the angle  $\alpha$  are assayed: 0, 15, 30, 45, 60, 75 and 90 degrees. When  $\alpha = 0^\circ$  ( $\alpha = 90^\circ$ ), the interface is subjected essentially to a normal load (shear load).

- Type E tests: ARCAN tests with edge effects (see Figure 32 and Figure 33). In this case the specimens do have a flat shape at the edges and important edge effects on stresses are expected (stress singularities at the edges of the interfaces). The dimensions of specimens E are provided in appendix 1. The area of the adhesion surface is 65mm×10mm. The adhesive thickness is 0.5 mm. The specimens are made with a 1018 steel and the D609 adhesive. Seven values of the angle  $\alpha$  are assayed: 0, 15, 30, 45, 60, 75 and 90 degrees.
- Type F tests: torsional tests with cylindrical butt joints (see Figure 34). The dimensions of specimens F are provided in appendix 1. A guide in these specimens allows to ensure the coaxiality of the two parts of the specimen (see appendix 1). The adhesive thickness is 0.5 mm. Two types of metals are considered for the substrates: 1018 steel or aluminum. The two adhesives (D609 and E20HP) are applied to the two substrates above so as to obtain 4 types of butt joints. The specimens with an aluminum substrate have a 28.575mm (1 1/8") diameter whereas those with a steel substrate have a 31.75mm (1 1/4") diameter. This difference in diameters was required to ensure that the machine could break the aluminum specimens.

Type D and E tests were carried out at a 1mm/min load rate. Type F tests were carried out at a 2°/min loading rate.

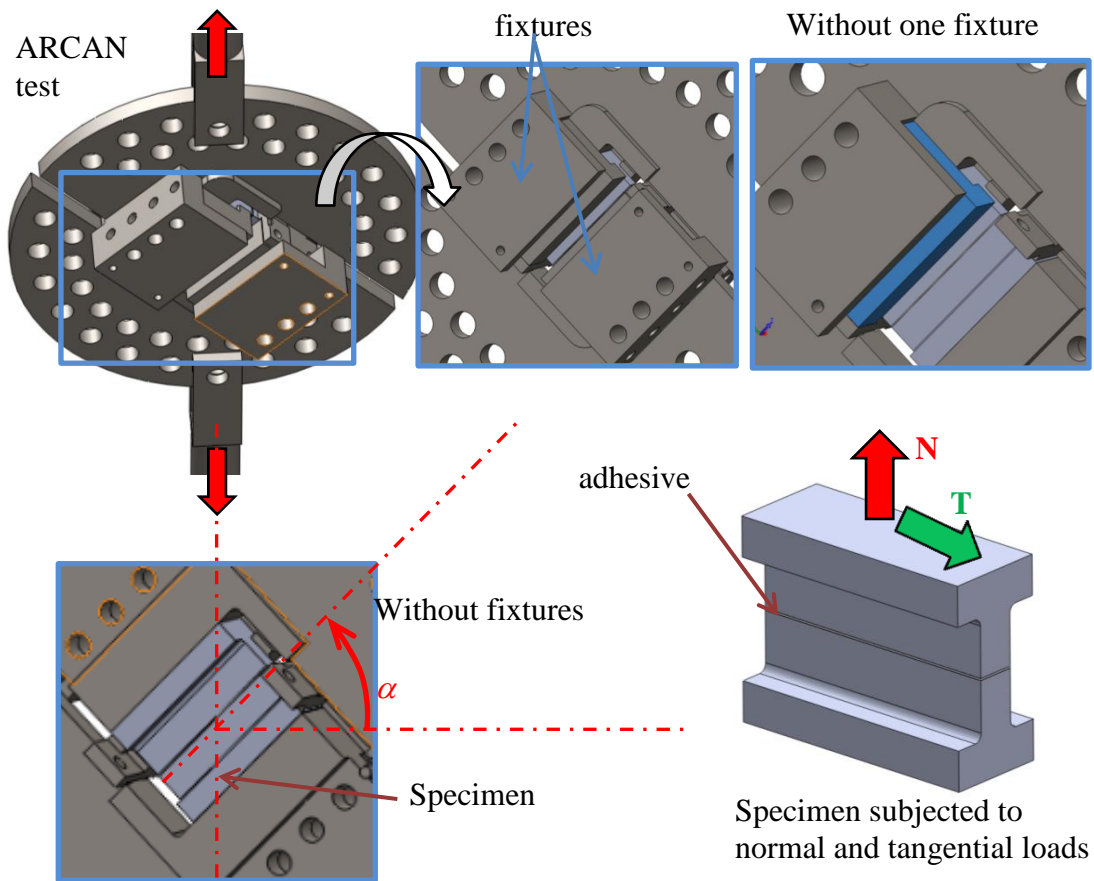


Figure 32. Arcan tests.



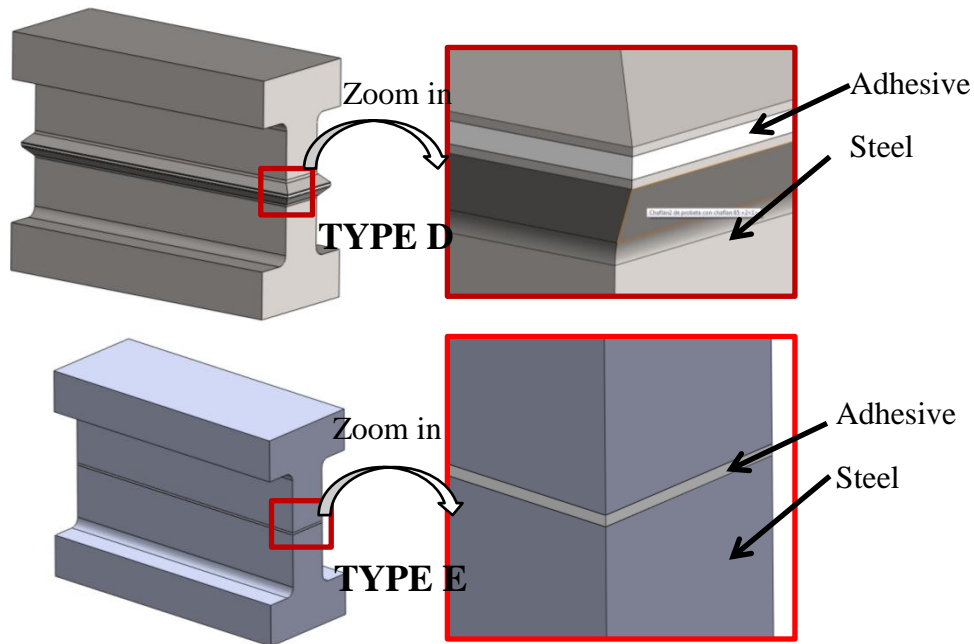


Figure 33. Type D and E specimens

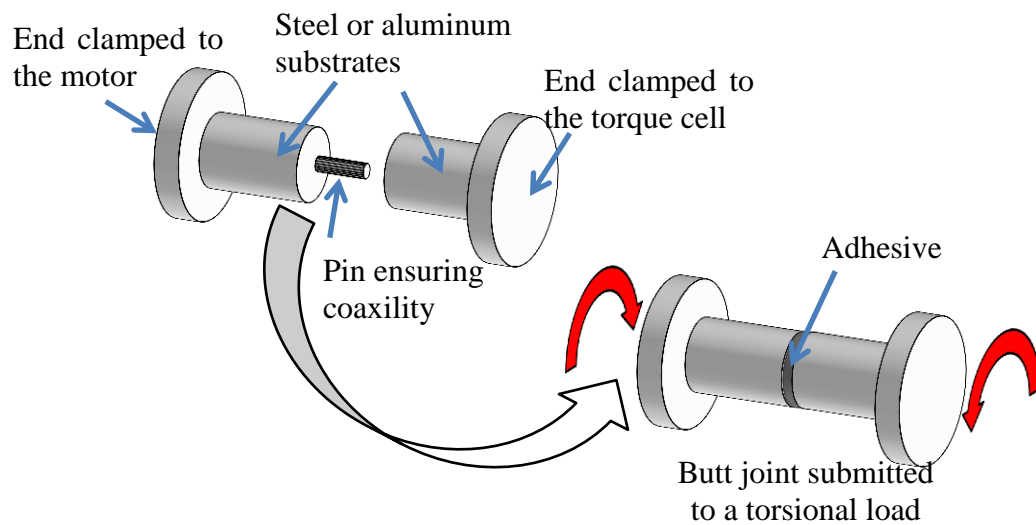


Figure 34. Type F specimens and tests.

The ARCAN discs and fixtures were designed in SolidWorks software and built with a D2 steel. In appendix 1, the dimensions of the discs and fixtures are shown. The surfaces of all

specimens were treated with a sandblasting technique for them to have practically a same roughness ( $R_a = 2\mu\text{m}$ ). In Figure 35, a device designed to prepare specimens and the application of the adhesive are shown. After leaving the type D and E specimens 24 hours at room temperature, the specimens are subjected to the heat treatment described in section 4.2. An example of a specimen D is shown in Figure 36. The ARCAN device mounted on a universal testing machine can be observed in Figure 37

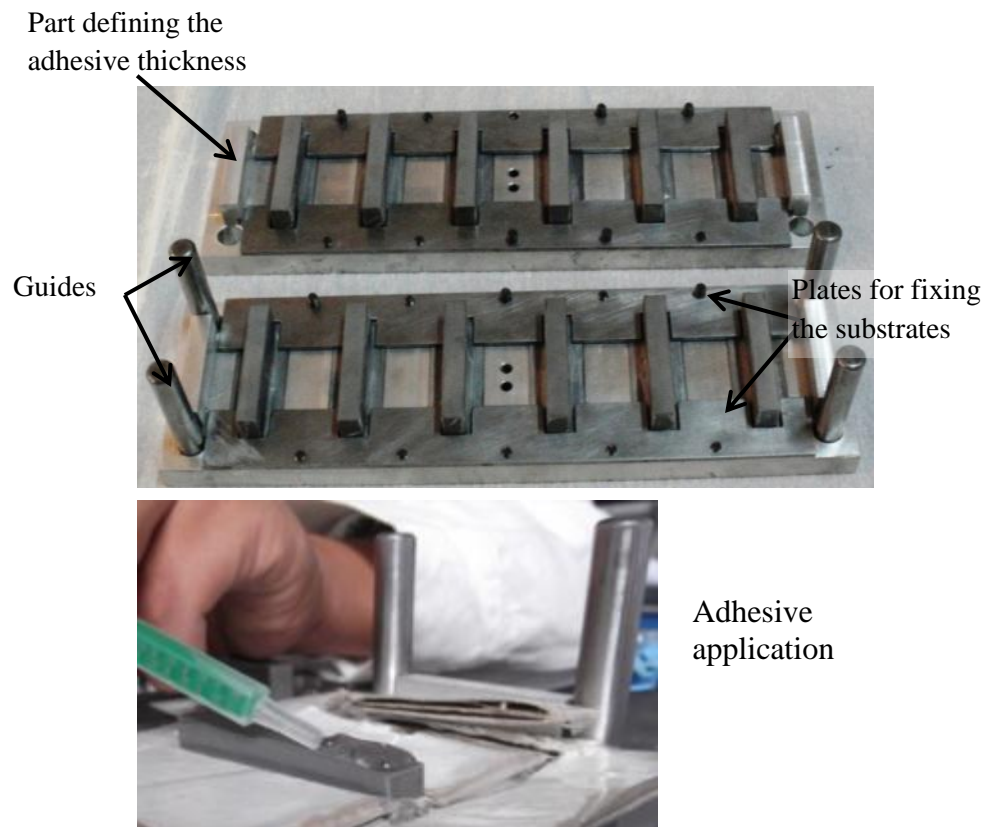


Figure 35. Preparation of type D and E specimens (devices and adhesive application)

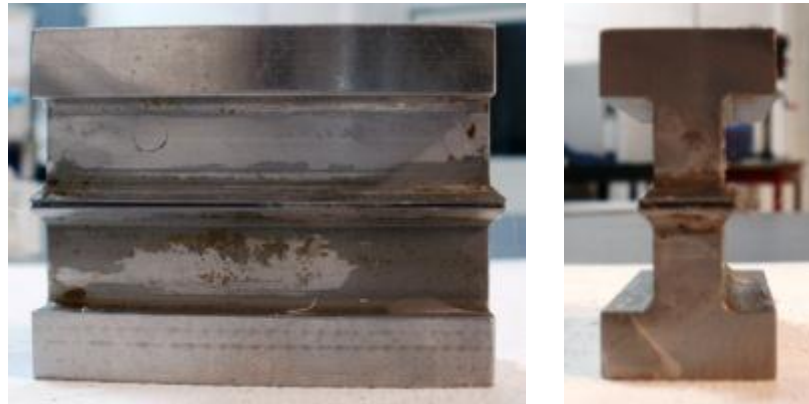


Figure 36. Example of a manufactured type D specimen.

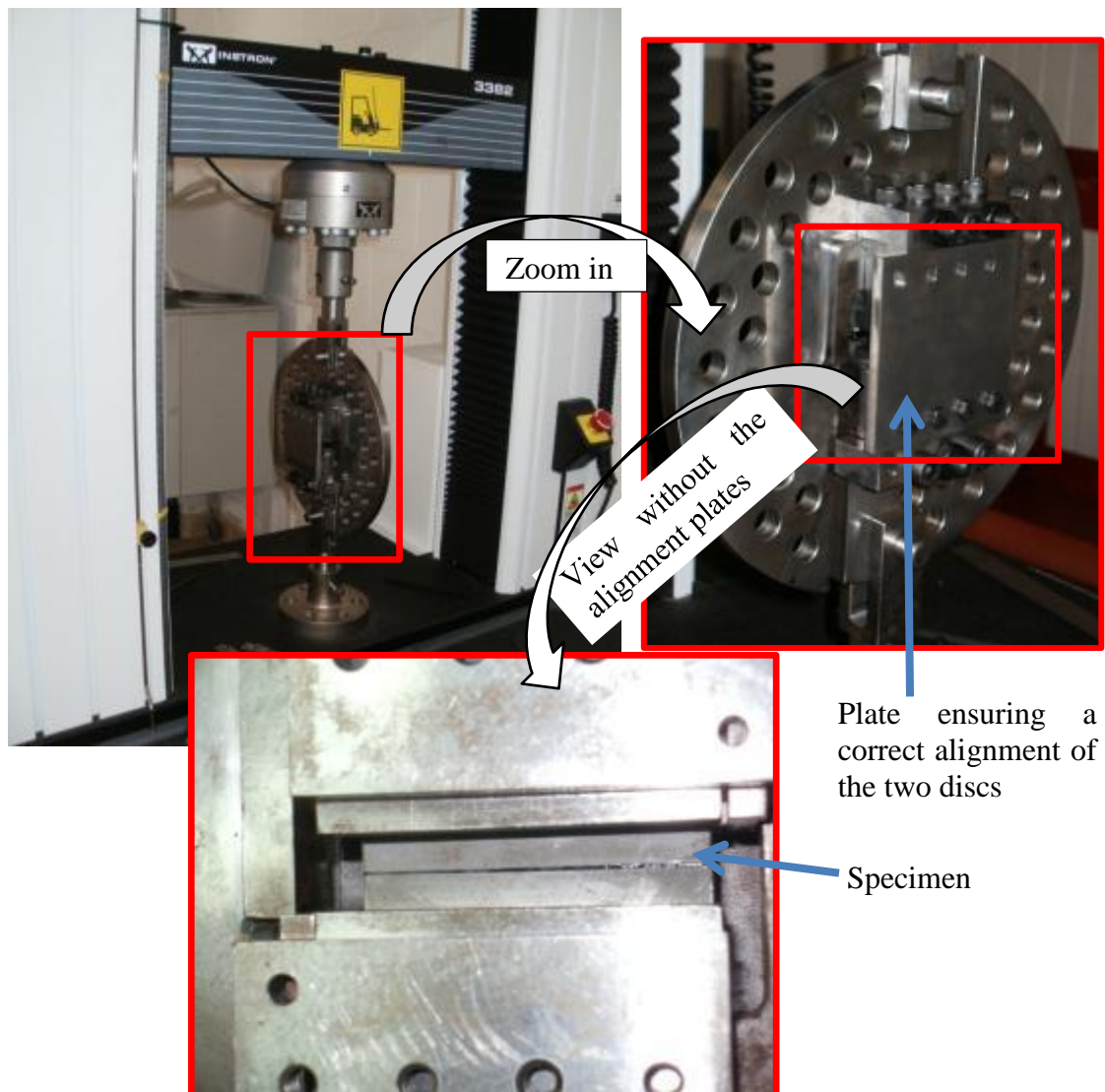
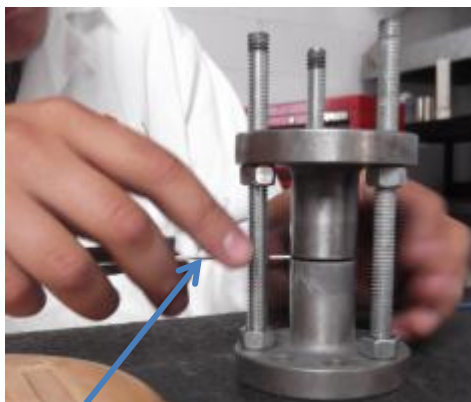


Figure 37. Pictures of the ARCAN devices mounted on an INSTRON universal machine.

For type F tests (butt joints), the substrates were machined and the surfaces were sandblasted to obtain a same roughness. In Figure 38, the preparation of type F specimens is illustrated. The specimens were cured during 24 hours as suggested by the adhesive provider at room temperature and tested five days after. *Unfortunately, for these tests the heat treatment required to ensure a quasi-complete curing of the adhesives was not performed because the treatment has been found after the tests were carried out.* The tests were carried out on an Instron torsional machine. This machine is able to apply a very small axial load combined with the torsional load. The value of this axial load is not enough to create considerable normal stresses on the butt joint. These normal stresses are negligible as compared to the shear stresses caused by the torsional load.



Gage to define the adhesive thickness



Adhesive application

Figure 38. Preparation of specimens F.

## 2. Results

### 2.1 Joints bonded with the polyester adhesive

#### 2.1.1 Type A tests results

For this type of tests, due to the simplicity of the device used, no force vs. displacement graphs were obtained. Only critical combination values of axial force and torque were obtained. All the tests carried out had a spontaneous catastrophic failure with an abrupt noise. In practically every test, an adhesive failure was observed; two pictures displaying a typical interfacial failure are shown in Figure 39. The values of force and torque at failure are provided in Table 3. It is worth mentioning that two A1 and two A7 tests were carried out.



Adhesive failure (most cases)



Adhesive and cohesive failure (few cases)

Figure 39. Typical failures for tests A.

Test	Axial Force (KN)	Torque (Nm)
A1	1.130 – 1.083	0
A2	0.650	2.438
A3	0.773	3.127
A4	0.523	3.040
A5	0.434	4.251
A6	0.193	3.421
A7	0	4.824 – 4.745

Table 3. Measured loads at failure for tests A.

### *2.1.2 Type B tests results*

In Figure 40, the graphs of force vs. displacement in type B tests (tension with double lap joints) are shown. The apparent initial non-linear behavior is due to gap adjustments and the finite rigidity of the testing machine and load cell. It is clearly appreciated that an increase in the adhesive length implies a rigidity and strength increase in the specimens. The failure was catastrophic and occurred spontaneously with an abrupt noise. For each adhesive length, 3 repetitions were performed. The averages of the force values at the failure moment are given in Table 2. In spite of the careful preparation of specimens, the failure scenario was very complex and variable even between specimens having the same adhesive length. Adhesive and cohesive failures occurred and sometimes the interfaces with longer adhesive failed as well. Despite this variability, a constant in all the tests was the failure of interface 2 or 3 indicated in Figure 41. In this figure, a picture showing the failure of a specimen with a 10mm adhesive length is shown.

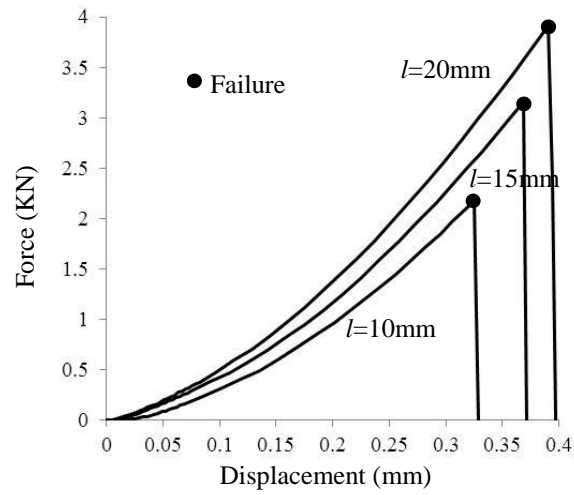


Figure 40. Force vs. displacement curves (tests B)

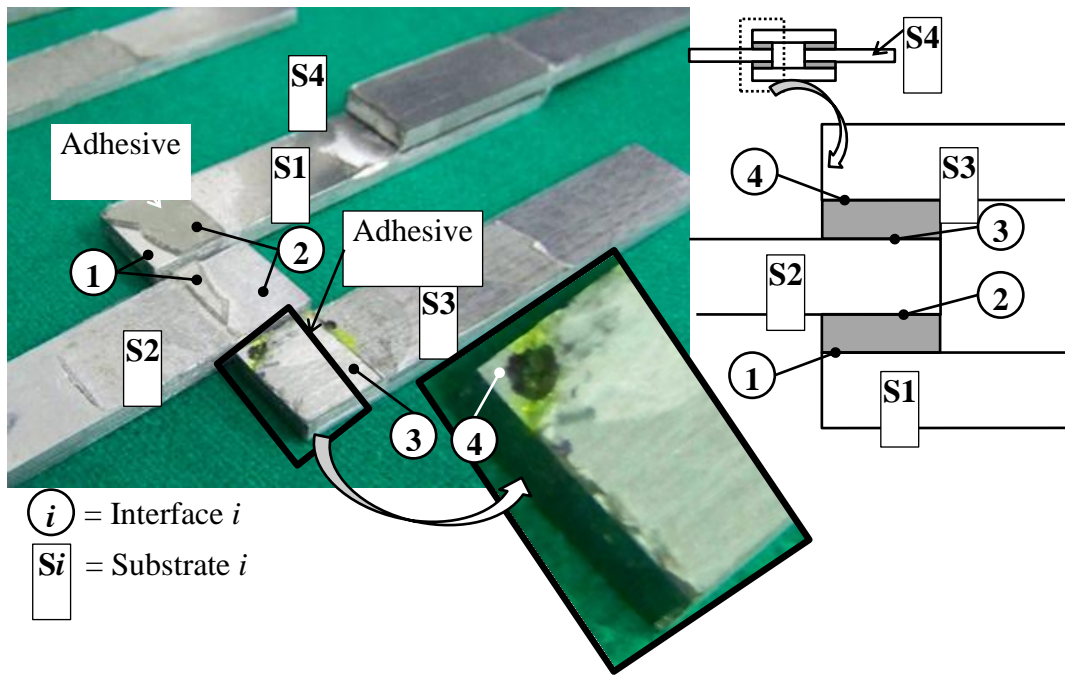


Figure 41. Adhesive and cohesive failures (test B,  $l=10\text{mm}$ ).



Adhesive length (mm)	Failure load - tests B	Failure load- tests C
10	$2374^{+406}_{-613}$ N	$45.1^{+5.3}_{-8.3}$ N
15	$3374^{+948}_{-626}$ N	$48.7^{+3.2}_{-6.4}$ N
20	$3632^{+1659}_{-1298}$ N	$51.6^{+9.5}_{-5.6}$ N

Table 4. Failure loads for tests B and C.

### 2.1.3 Type C tests results

For each adhesive length, three repetitions were performed. In Figure 42, the graph of force vs. displacement for a representative test of each adhesive length is shown. It is possible to appreciate one more time that an increase in the adhesive length implies an increase in rigidity and strength. Adhesive failures occurred spontaneously at interfaces 1 or 4 and in some cases a cohesive failure also occurred as shown in Figure 42. In Table 4, the averages of the forces leading to failure for every specimen are shown.

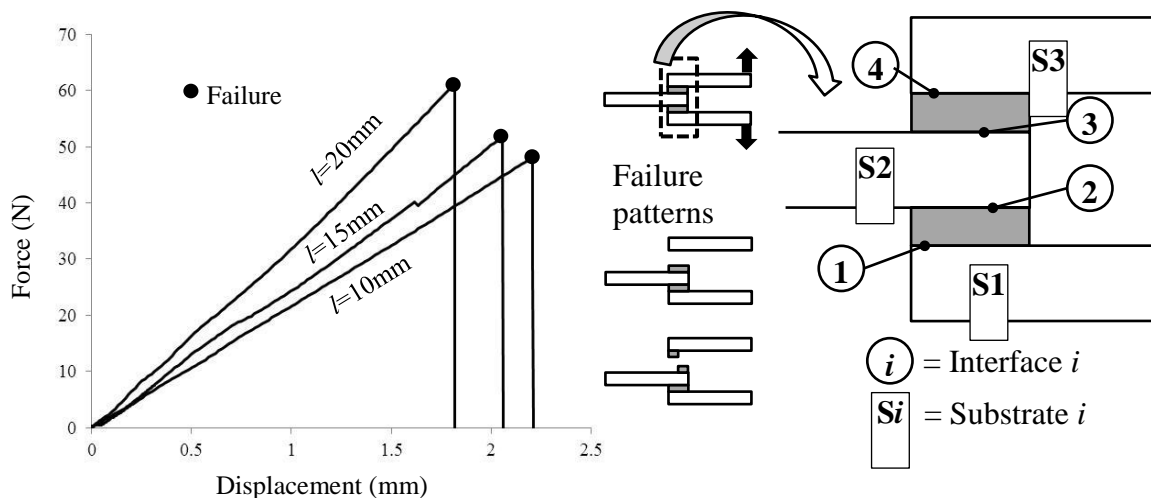


Figure 42. Force vs. displacement curves and failure patterns (tests C)



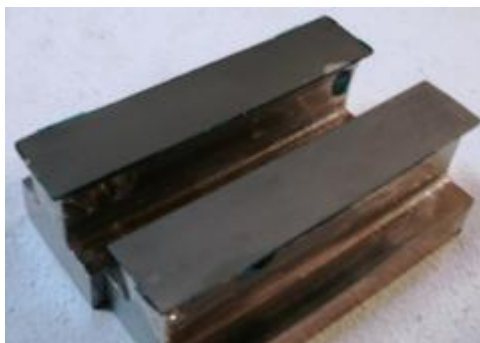
## 2.2 Joints bonded with Hysol adhesives

### 2.2.1 Type D and E tests results

The failure loads obtained for specimens D for each angle  $\alpha$  considered are shown in Table 5. Two repetitions per angle were performed. The specimens failed spontaneously with an abrupt noise. This is a characteristic of an unstable failure mechanism. The failure was essentially an interfacial failure as shown in Figure 43. In Figure 44, the example of two force vs. displacement curves is shown for type D specimens loaded with an inclination of 30 and 45°. It is worth mentioning that gaps between the parts of the ARCAN device affect the curve shape for loads lower than 200 Kg. In this Figure 44, one can notice that failure occurs abruptly. Similar curves were obtained for the other specimens even for type E specimens.

Angle $\alpha$	0	15	30	45	60	75	90
Failure load (Kg )	1573	1302	1364	2069	1053	1507	1485
	1459	1648	1850	1354	1503	1284	1851

Table 5. Failure loads for tests D.



$\alpha = 0^\circ$  , pure interfacial failure



$\alpha = 90^\circ$  , interfacial and cohesive failure

Figure 43. Example of two failures in type D specimens.

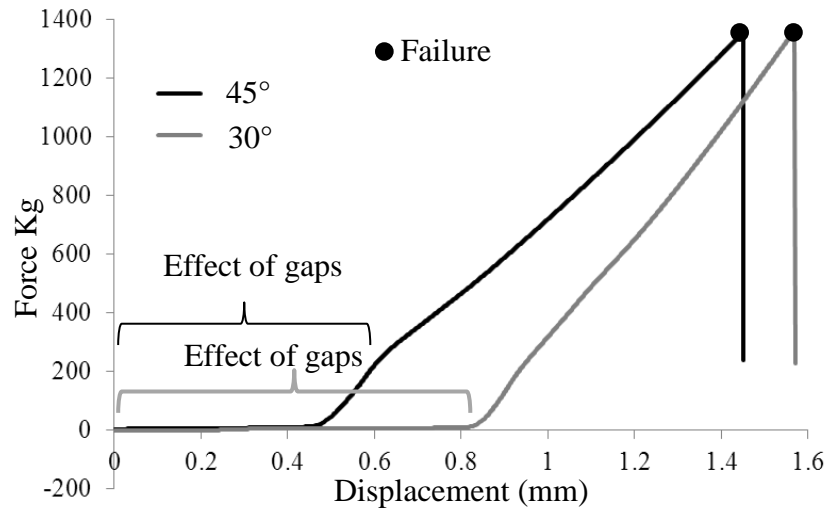


Figure 44. Force vs. displacement curve of two type D specimens loaded at 30° and 45° angles

The failure loads obtained for specimens E for each angle  $\alpha$  considered are shown in Table 6. Three repetitions per angle were performed. An important scattering is observed. The specimens failed once again spontaneously with an abrupt noise and the failure was essentially an interfacial failure as shown in Figure 45. In Figure 46, an example of flaws detected in some specimens is shown. The maximum size of flaws was 3mm. These flaws and manufacturing defects near the edges may be the cause of the scattering of results.

Angle $\alpha$	0	15	30	45	60	75	90
Failure load (Kg)	951	689	900	517	868	1095	851
	601	534	622	548	729	779	562
	317	500	665	452	722	450	462

Table 6. Failure loads for tests E.



Figure 45. Example of two failures in type E specimens.

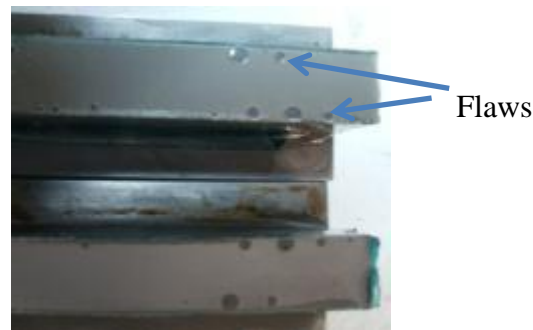


Figure 46. Flaws in some type D and E specimens.

### 2.2.1 Type F tests results

In Table 7, the averages of torsional moments at failure are provided. For each type of specimen, 8 repetitions were performed. The torque vs. rotational angle curve of a representative test for each type of specimen is shown in Figure 47. It is important to recall that the diameter of aluminum specimens is 28.575 whereas that of steel specimens is 31.75mm. In Figure 47, one may observe that for aluminum specimens the failure occurs progressively whereas for steel specimens failure occurs abruptly. These may be due to important plastic phenomena that take place in the aluminum specimens. In Figure 48, a typical failure (essentially interfacial failure) of type F specimens is shown.

Substrate \ Adhesive	D609	E20HP
Steel	$192^{+8}_{-20}$ Nm	$167^{+3}_{-2}$ Nm
Aluminum	$192^{+5}_{-18}$ Nm	$170^{+5}_{-7}$ Nm

Table 7. Failure torques for tests F.

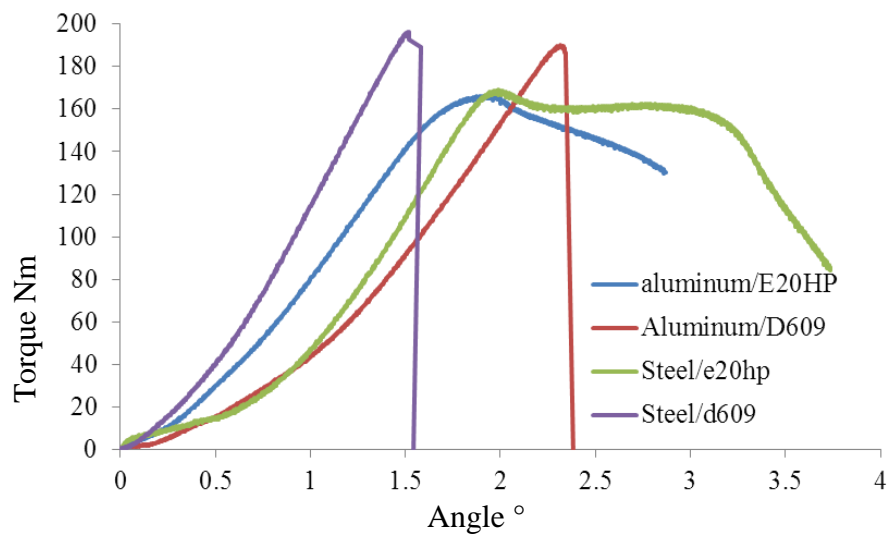


Figure 47. Example of torque vs. rotation angle curves obtained for type F tests.



Figure 48. Typical failure of type F tests (example of an aluminum/E20HP specimen).

### **3. Conclusions**

Mechanical tests with adhesive joints with three types of adhesive and two types of substrates were performed. Different geometries and loading conditions were considered. The results represent an important set of experimental data to test the accuracy of any method which aims to predict failure onset for any geometry and loading condition. Except for type F tests, the results will be applied on chapter IV to predict failure initiation. Type F tests are not applied because the curing process of the adhesive was not correctly controlled as described in section 4.1 of chapter 1. These tests will be repeated with completely cured adhesives.

### **III. Stress calculation in structural adhesive joints**

In this chapter, the recommended methods to calculate stresses in adhesive joints are described. The stress calculation is the first stage in a prediction of failure onset. Two types of methods are described: solid finite element modeling and a layer-wise modeling in the case of plate-like joints. It is worth mentioning that two papers were published in the Composite Structures Journal dealing with the development and application of the layer-wise modeling was published in the Composite Structures Journal.

The solid finite element technique is applied to the analysis of stresses in the specimens tested in the previous chapter.

#### **1. Solid finite element modeling**

For all specimens considered, a 3D model would not be affordable taking into account the computational resources at CIMAV and the meshing refinements required at the intersections between interfaces and edges. For this reason, plane strain states or axial-like symmetries were considered.

##### **1.1 Linear elastic analysis for the tested adhesive joints**

###### ***1.1.1 Tests A, B and C***

##### **Validation of a linear elastic calculation of stresses in the adhesive joints**

The use of a linear elastic assumption streamlines considerably the stresses calculation and makes possible to use the theory of “linear elastic fracture mechanics”. Motivated by the fact that the polyester adhesive, in tension, had a quasi linear elastic behavior before its failure, we calculated for every type of specimen the stresses in the interfaces using a linear elastic model for the adhesive behavior and we compared it with the ones obtained using the same elastoplastic model of the adhesive determined in the previous section. The two types of calculation (linear elastic and elastoplastic) used the same boundary conditions. The load values used were the average critical values experimentally measured. Calculations were carried out with finite element software COMSOL Multiphysics 3.3. Stress singularities exist at the intersection between the interfaces and the free edges and for this reason a finer mesh density was used around these stress singularity points. Triangular elements were selected for the analysis and the smallest element size was  $2\mu\text{m}$  (the roughness measured on the substrates was  $R_a = 2\mu\text{m}$ ). The use of an element size smaller than the roughness of the substrate surface has no sense since this roughness is not taken into account in the modeling.

For type B and C specimens, a plane strain state was considered. In Figure 49, the meshing example of type B and C specimens is shown with an adhesive length of 10 mm. For the same specimens of Figure 49 and using both calculation techniques (linear elastic and elastoplastic), in Figure 50 shear and normal stresses in the critical interfaces which failed in the tests are shown. It is possible to appreciate that the interface stresses calculated with the two calculation methods are practically the same. This happens because the areas having plastic strains in the adhesive are limited to zones that are very close to the stress singularity points. The size of these zones is about  $10\mu\text{m}$  (dimensions that are similar to the substrate roughness, which is not taken into account in the analysis). For the other B and C specimens, we reach to the same conclusions as for the equivalence between the calculation methods we used. The same conclusion was also obtained with type A tests.

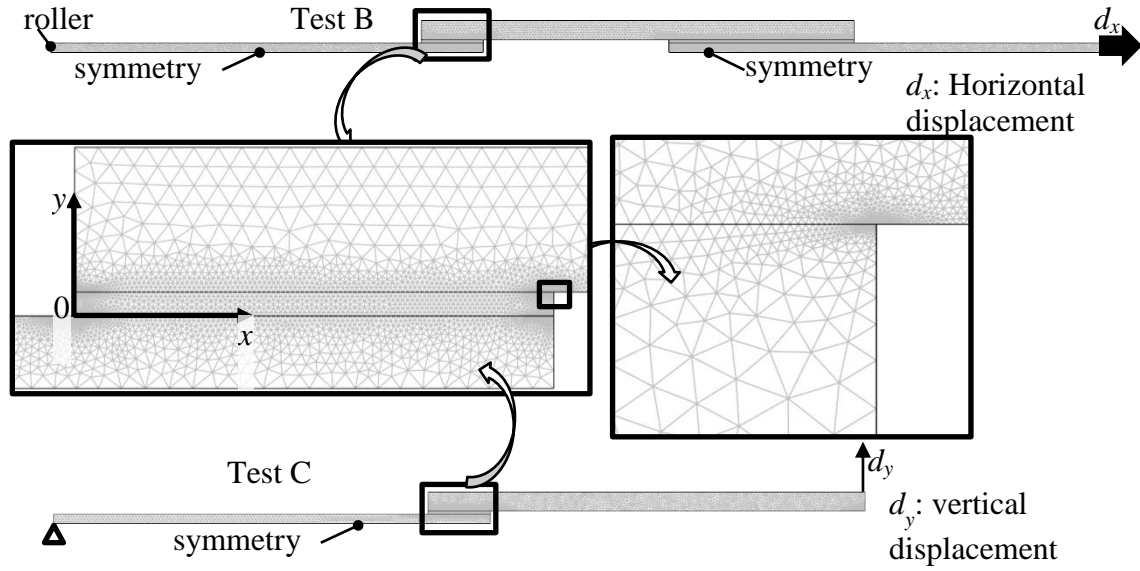


Figure 49. Meshing and boundary conditions (tests B and C)

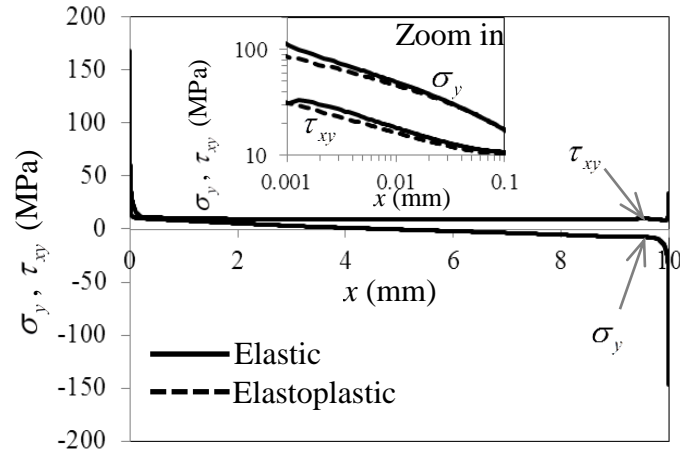


Figure 50. Interfacial shear and normal stresses (test B,  $l=10\text{mm}$ ).

From these comparisons, it is concluded that it is valid to use a linear elastic model for calculating stresses in adhesive joints assayed in this work because at the failure moment of interfaces, the stress level virtually in all the adhesive layer does not reach the necessary magnitude to cause considerable plastic strains. Thanks to this conclusion, it is possible to



carry out linear calculations to perform an analysis of stresses at the joints or to calculate interface stresses and challenge adhesive failure criteria.

### Boundary conditions applied and stress results

Let us consider tests A. In order to calculate stresses in cylindrical butt joints subjected to tension and torsion, we adopt a cylindrical coordinate system  $(r, \theta, z)$ . The boundary conditions are:

- $U_z = U_\theta = \sigma_{rz} = 0$  at the bottom boundary,
- $U_z = D$ ,  $U_\theta = r\alpha$ , and  $\sigma_{rz} = 0$  at the top boundary,
- $\sigma_{rr} = \sigma_{r\theta} = \sigma_{rz} = 0$  at the vertical boundary,

where  $\mathbf{U}$  is the displacement vector,  $\boldsymbol{\sigma}$  is the stress tensor,  $D$  is the imposed elongation and  $\alpha$  is the imposed torsional angle. A resolution of the mechanical equations in an  $(r, z)$  plane is proposed because displacements, strains and stresses do not depend on the angular coordinate (see Figure 51). The equations were programmed and solved in COMSOL. Owing to this simplification of the 3D problem, an important saving in computing time and memory required is achieved. In Figure 51, the meshing used in COMSOL is shown. The stress state is a result of a superposition of the stresses obtained from the torsion problem and those from the tension problem. In Figure 52, the plots of the interfacial  $\sigma_{zz}$  normal and  $\sigma_{rz}$  shear stresses against the radial position at one interface are shown for the case of a 1kN axial load. An important edge effect is observed. In this loading case, results at the edge do not converge. In Figure 52, the  $\sigma_{\theta z}$  shear stress is plotted against the distance from the edge for the case of a 1Nm torsional load. It is worth mentioning that for this torsion case no singularities appear and the calculations of stresses converge. The shear stresses may be obtained by the classical torsion formula:

$$\sigma_{\theta z} = \frac{T}{J} r \quad (15)$$

where  $T$ ,  $J$ ,  $r$  stand for the torque, the polar moment of inertia and the radial position, respectively. Type A tests exhibit then mode III, mixed-mode I-II and mixed-mode I-II-III failures.

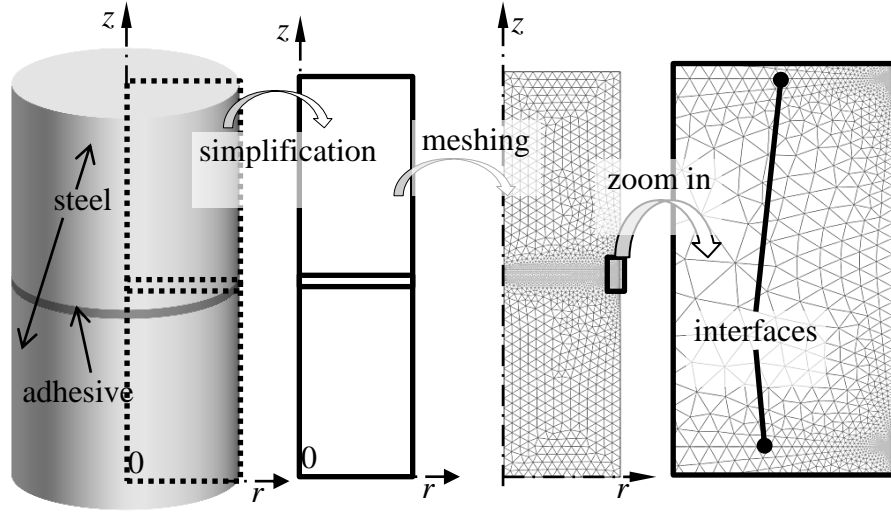


Figure 51. Modeling and meshing of type A specimens.

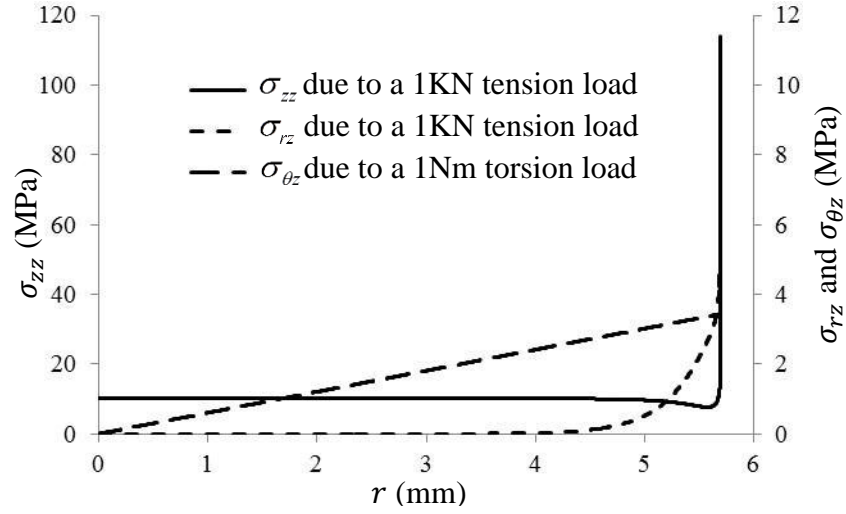


Figure 52. Interfacial normal and shear stresses (test A)

For type B and C specimens, a plane strain state was considered. In Figure 53, the meshing example of type B and C specimens is shown with an adhesive length of 10 mm. Let us consider this adhesive length for the results analyzed in this paragraph. In Figure 54, shear and normal stresses at the upper and lower interfaces (shown in Figure 53) are displayed for the type B specimen subjected to a 2.37KN load. Higher interfacial stresses appear near the bottom left stress singularity point for specimen B. In Figure 55, shear and normal stresses are plotted along the upper and lower interfaces of specimen C subjected to a 45.1N load. Higher interfacial stresses appear near the stress singularity point at the right edge of the upper interface of specimen C. It is for these reason, from a stress point of view, that these points (or their symmetric ones) with a higher stress concentration were connected to a crack in the experiments with specimens B and C shown in section 2. The results in Figure 54 Figure 55 prove that type B and C tests exhibit mixed-mode I-II failures.

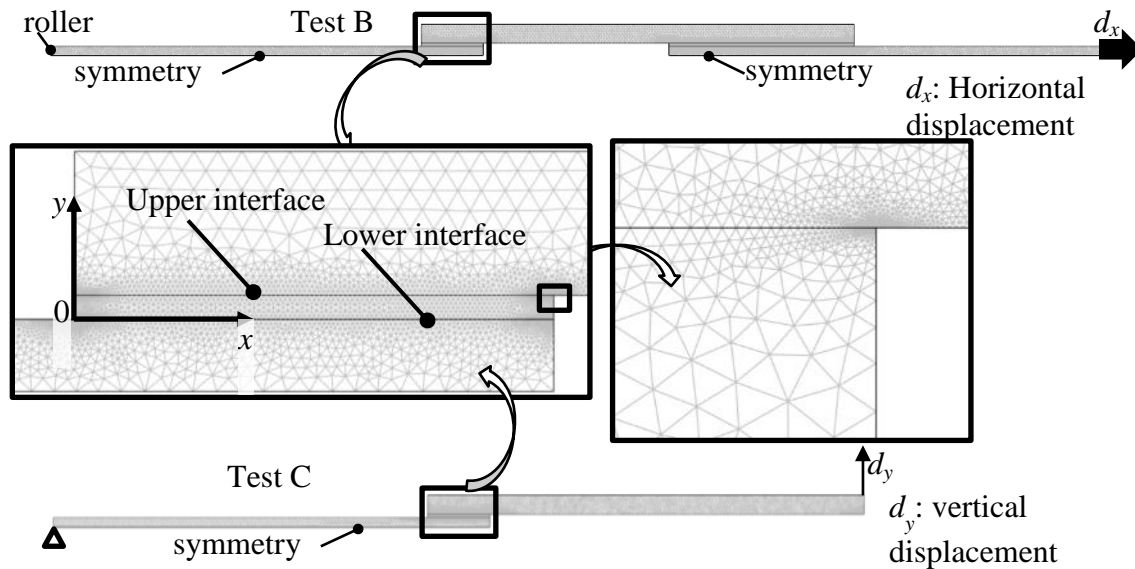


Figure 53. Meshing and boundary conditions (tests B and C)

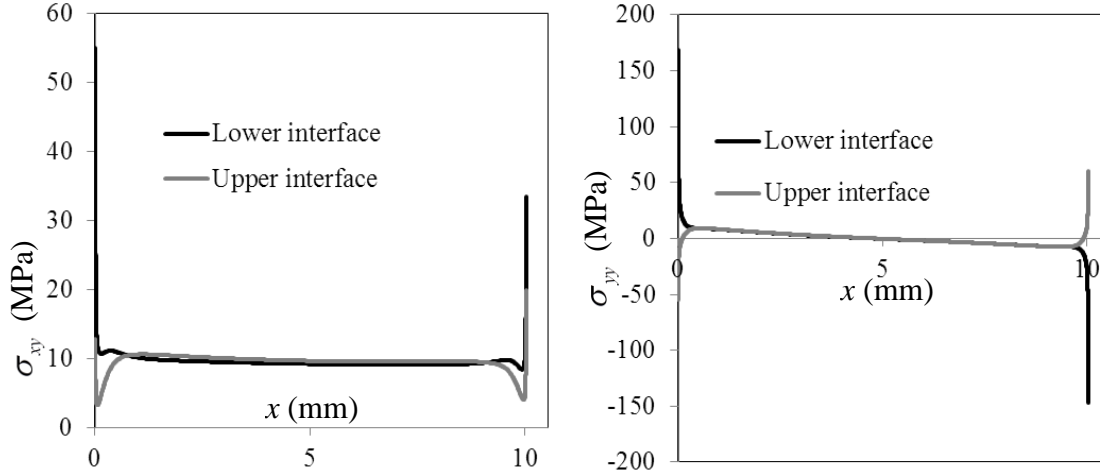


Figure 54. Interfacial normal and shear stresses (test B,  $l=10\text{mm}$ ).

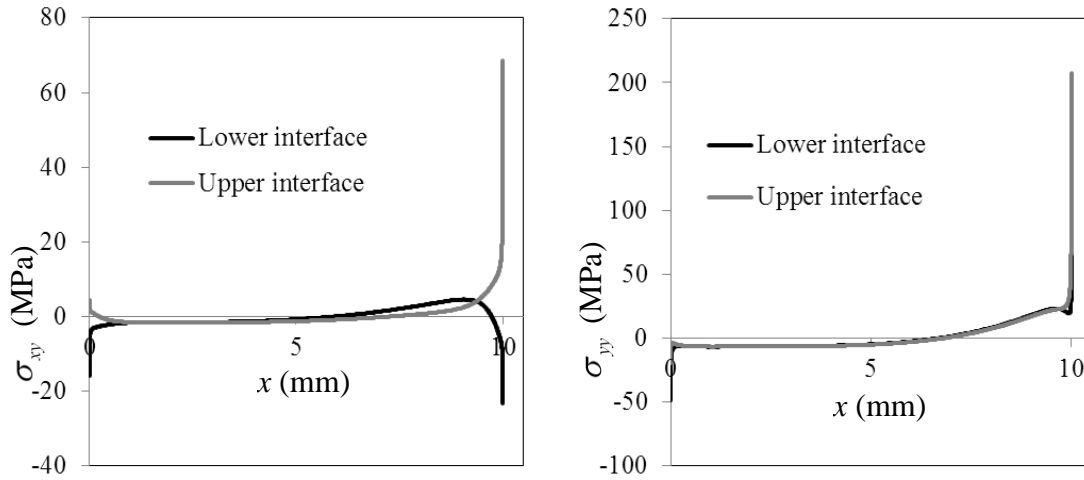


Figure 55. Interfacial normal and shear stresses (test C,  $l=10\text{mm}$ ).

### 1.1.2 Tests D, E and F

In Figure 56, the studied geometry and the selected boundary conditions are shown. Displacements are zero at the bottom of the geometry and the displacements of the top of the geometry are

$$U_x = D \sin(\alpha) \text{ and } U_y = D \cos(\alpha) \quad (16)$$

where  $D$  is the total displacement of the top edge. The meshing of specimens of tests D and E is shown in Figure 57. As will be shown in the next chapter, the failure prediction requires the analysis of cracked specimens. A finer meshing is chosen near the stress singularity points and at the crack tip of specimens E as shown in Figure 57. Once again the mesh size was greater than  $2\mu\text{m}$ .

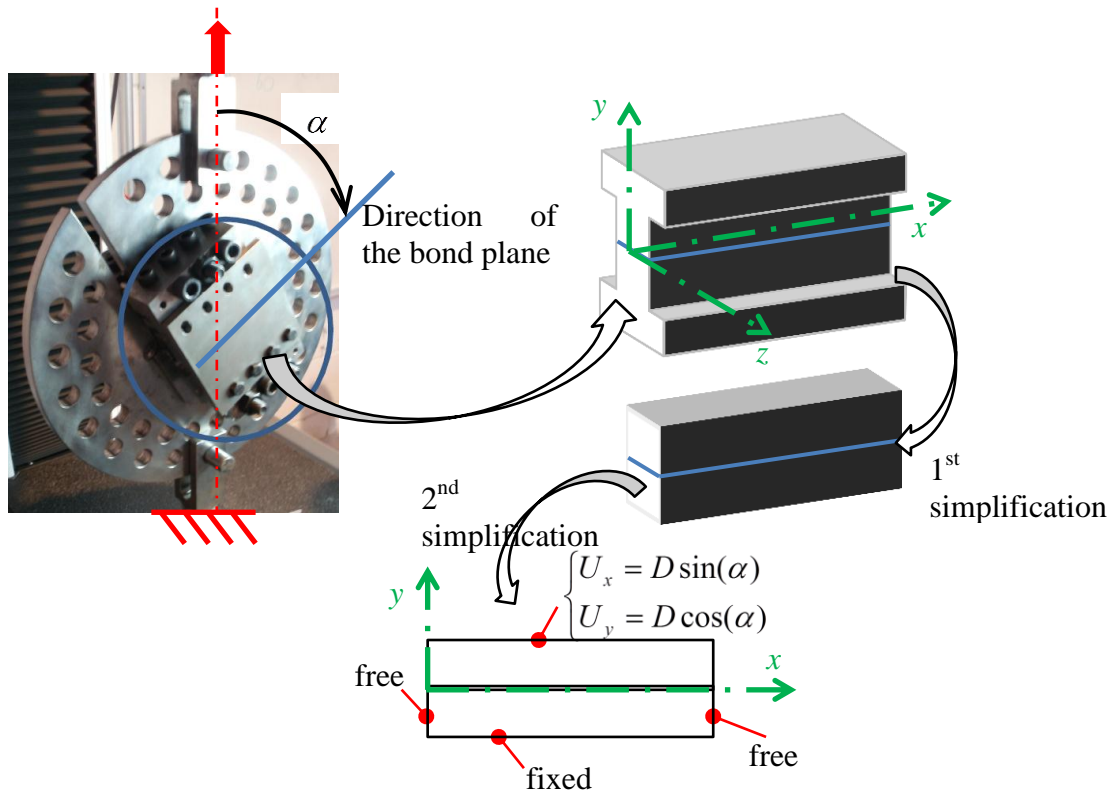


Figure 56. Modeling and boundary conditions for ARCAN specimens

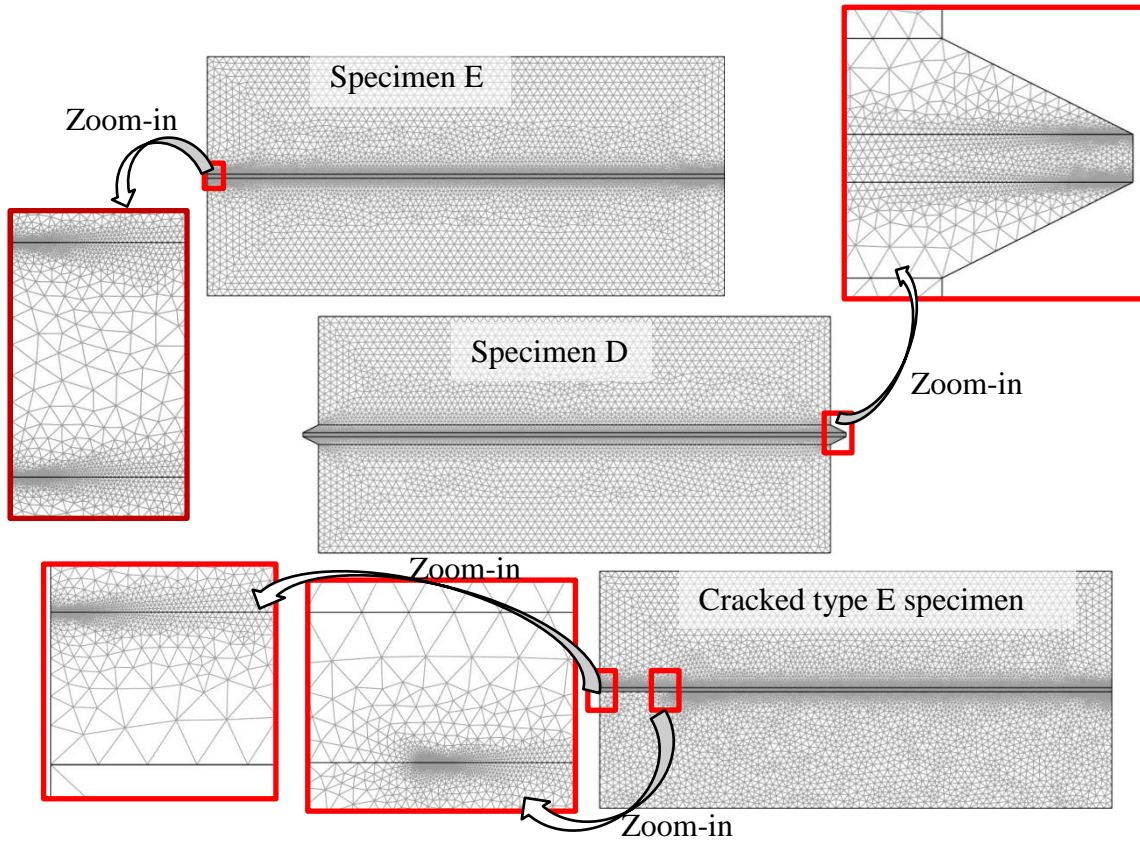


Figure 57. Meshing of specimens D and E.

For a specimen D tested at different angles and for a  $D$  load generating a 1Ton tensile force, the interfacial normal and shear stresses are shown in Figure 58 and Figure 59, respectively. These stresses are calculated at the bottom interface between the D609 adhesive and steel. Analogue curves for a specimen E are shown in Figure 60 and Figure 61. One may observe that an important reduction of the stress concentrations is performed by the shape of the edges of specimen D. In most cases, the stress singularities are negligible in specimens D whereas in specimens E an important stress concentration occurs at the intersection between edges and interfaces.

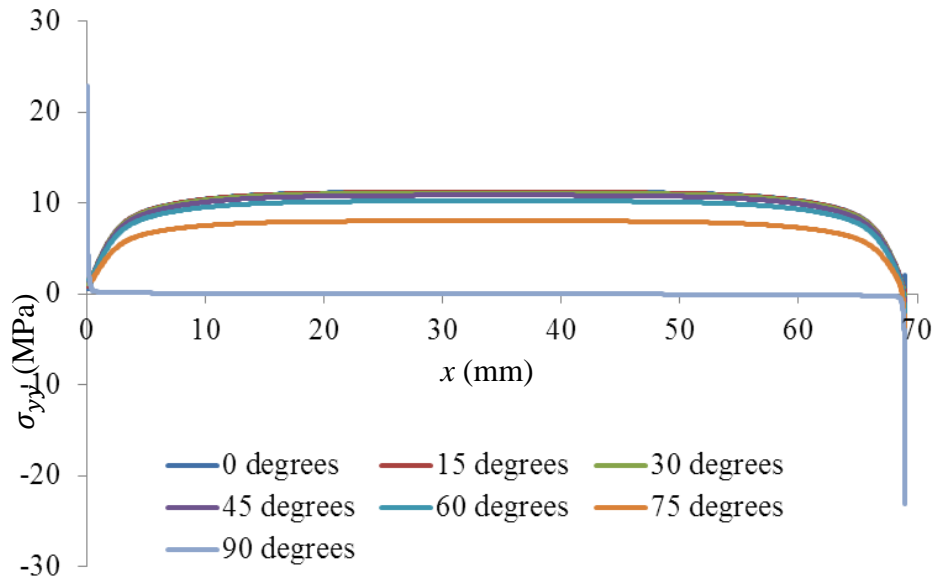


Figure 58. Interfacial normal stresses at the bottom interface for a 1Ton load (specimen D)

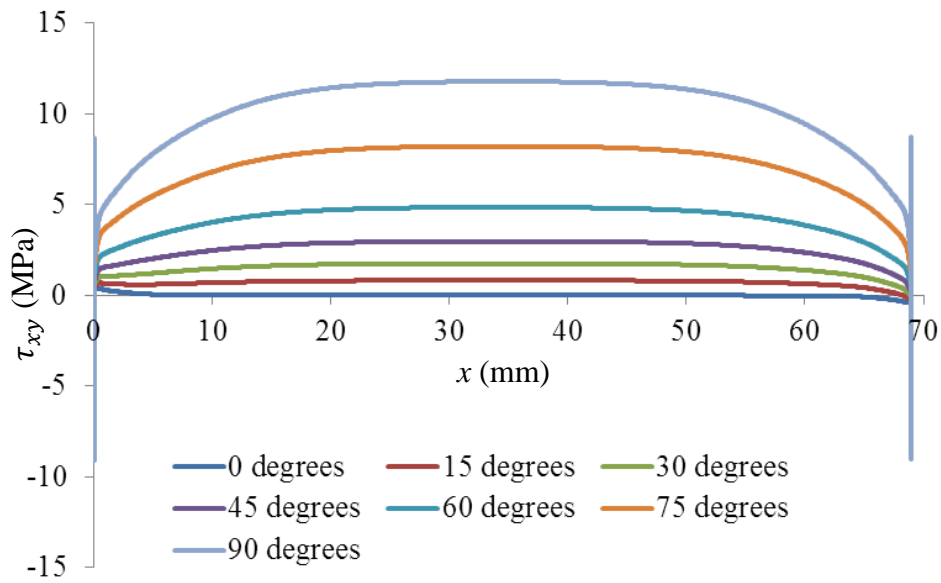


Figure 59. Interfacial shear stresses at the bottom interface for a 1Ton load (specimen D)

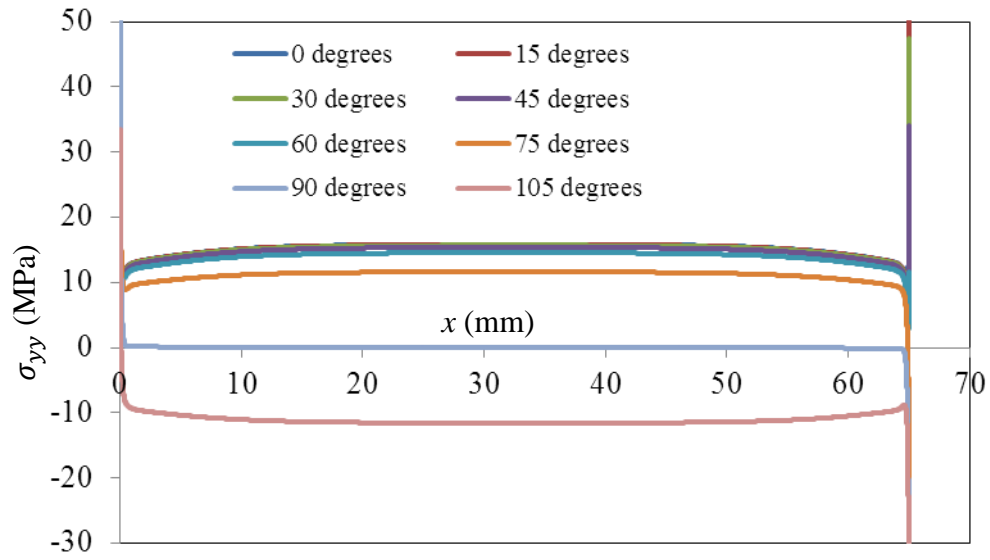


Figure 60. Interfacial normal stresses at the bottom interface for a 1Ton load (specimen E)

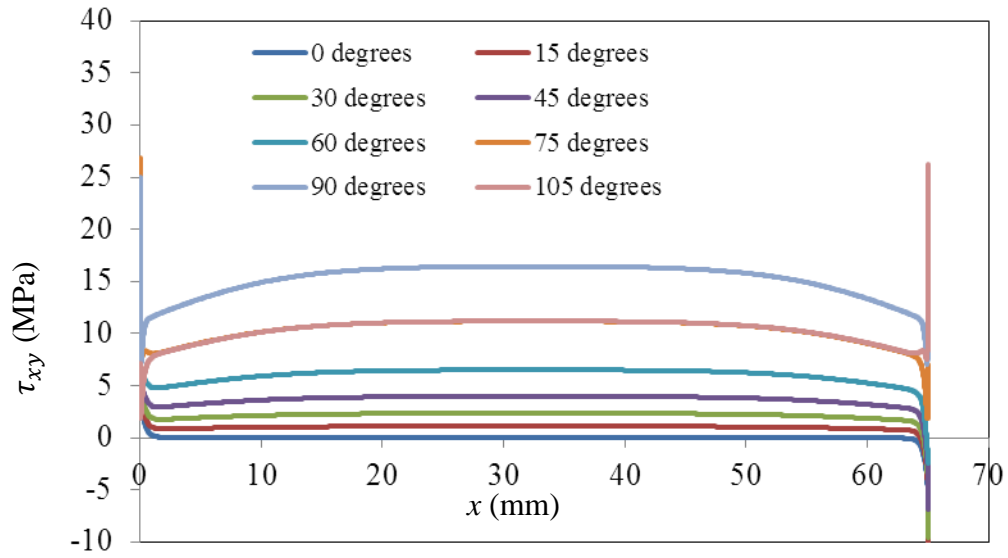


Figure 61. Interfacial shear stresses at the bottom interface for a 1Ton load (specimen E)



## 1.2 Non-linear analysis

Currently, a correct and complete modeling of the non-linear behavior of the structural adhesives considered in this project has not been developed yet. Hysol D609 and E20HP exhibit a complex viscoplastic behavior and an operational model is not available yet so as to predict stresses, strains and failure in an adhesive joint applying these materials. Awaiting for such models, we decided to program in COMSOL Multiphysics 3.5 (a commercial finite element software) a conventional viscoplastic model for the adhesive in order to show our ability to take into account complex constitutive models to determine accurately stresses and strains in adhesive joints. Also, this application shows the important effects of load rates on the behavior of structural adhesive joints.

The constitutive model considered herein for the adhesive is summarized as follows [2]:

- Linear elastic constitutive equation:

$$\sigma_{ij} = \frac{E}{1+\nu} (\varepsilon_{ij} - \varepsilon_{ij}^p) + \frac{\nu E}{(1+\nu)(1-2\nu)} (\varepsilon_{kk} - \varepsilon_{kk}^p) \delta_{ij} \quad (17)$$

where  $E$  and  $\nu$  are the Young's modulus and the Poisson's ratio, respectively;  $\boldsymbol{\sigma}$ ,  $\boldsymbol{\varepsilon}$  and  $\boldsymbol{\varepsilon}^p$  are the stress, strain and plastic strain tensors;  $\delta$  is the Kronecker delta function.

- Yield function:

$$f(\boldsymbol{\sigma}, \mathbf{X}) = \left( \frac{3}{2} \sum_{1 \leq i, j \leq 3} (\sigma_{ij}^d - X_{ij}^d)^2 \right)^{1/2} - \sigma^y \quad (18)$$

where  $\sigma^y$  is the yield stress,  $\mathbf{X}$  is the kinematic hardening stress, the superscript  $d$  stands for the deviatoric part of a tensor.

- Odqvist's law

$$\dot{\varepsilon}_{ij}^p = \frac{3}{2} \left( \frac{f(\boldsymbol{\sigma}, \mathbf{X})}{K} \right)^N \frac{\sigma_{ij}^d - X_{ij}^d}{(\boldsymbol{\sigma} - \mathbf{X})^{eq}}, \quad \dot{p} = \left( \frac{f(\boldsymbol{\sigma}, \mathbf{X})}{K} \right)^N \quad (19)$$

where  $p$  is the cumulative plastic strain,  $K$  and  $N$  are material parameters defining the viscoplastic behavior

- Kinematic hardening rule

$$\dot{X}_{ij}^d = \gamma \left( \frac{2}{3} X_{\infty} \dot{\varepsilon}_{ij}^p - X_{ij}^d \dot{p} \right) \quad (20)$$

where  $\gamma$  and  $X_{\infty}$  are constants.

The case of the D609 adhesive is analyzed. The material parameters involved in the equations were determined by fitting the experimental results obtained in the uniaxial tests as shown in section 4.2 of chapter I ( $E = 3.4\text{GPa}$ ,  $\nu = 0.33$ ,  $\sigma^y = 1\text{MPa}$ ,  $\gamma = 200$ ,  $X_{\infty} = 24\text{MPa}$ ,  $K = 2000\text{MPa s}^{1/N}$  and  $N = 2.11$ ).

The structure considered in this case is a double lap adhesive joint which dimensions are shown in Figure 62. The joint is subjected to a tensile load on its edges. Owing to symmetries and to a plane strain assumption, the problem can be reduced to the analysis of the structure in Figure 63. In this figure, the boundary conditions applied and the meshing of the geometry are shown. At the left end of the joint a displacement  $D$  is applied. The resultant force is then  $F$ . Six loading rates are considered: 0.125, 0.25, 0.5, 1, 2 and 4 mm/min.

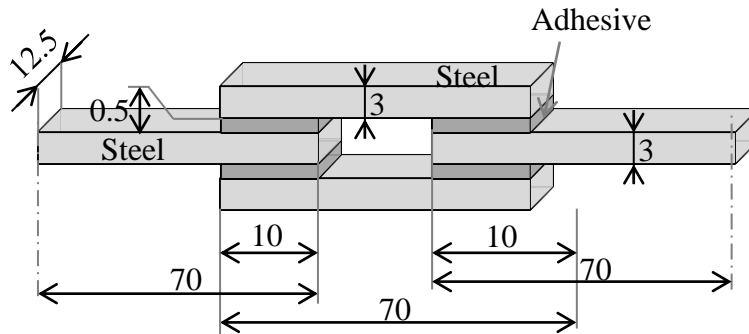


Figure 62. Dimensions of the double lap joint considered for the non-linear calculations

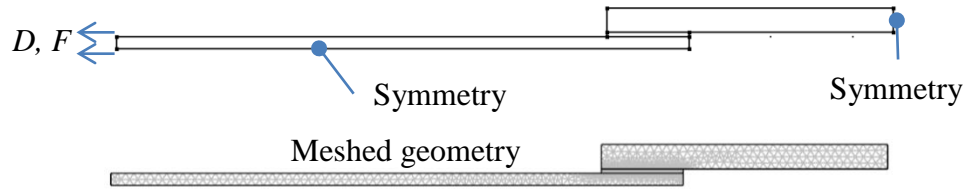


Figure 63. Geometry simplification, boundary conditions and meshing

In Figure 64, the force vs. displacement curves predicted by COMSOL are shown for each loading rate considered. An important effect of the load rate is observed. If the failures of interfaces, adhesive or substrates were not considered, the maximum values of the force in the previous curve would provide the strength of the joint. With these values, we have plotted in Figure 65 the upper bounds of the strength of the joint against the displacement rate.

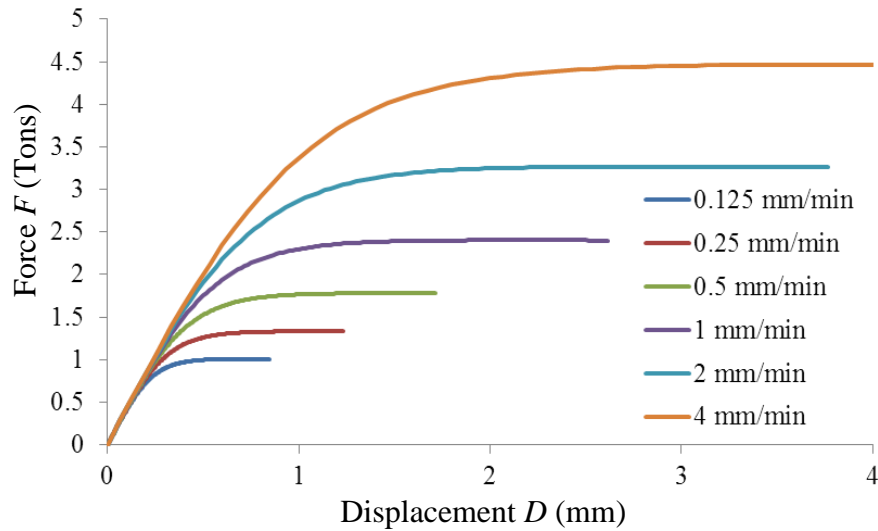


Figure 64. Predicted force vs. displacement curves with different loading rates.

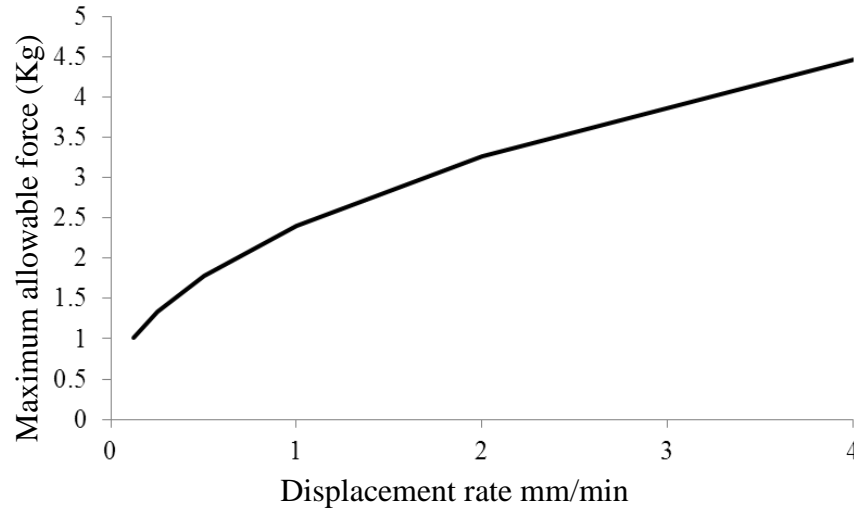


Figure 65. Maximum allowable force vs. loading rate curve.

The previous example shows our capacity to carry out a structural analysis for adhesive joints having an adhesive with a viscoplastic behavior. Once the final 3D constitutive model for the adhesive will be obtained, we will implement the model in COMSOL so as to predict the behavior and stresses within adhesive joints. This task will be carried out on 2013.

## 2. A layer-wise model for plate-like adhesive joints

In the case of plate-like adhesive joints, a solid finite element technique may become unaffordable owing to the computational cost. A plate model is an alternative to analyze stresses in these types of structures. In this section, the enhancement of a layer-wise model considering thin layers of adhesive with a nonlinear behavior is briefly described. A thorough description of the model equations and its validation has been published in [10] and [11].

## 2.1 Model description

In [12], Aquino de Los Rios et al proposed an adaptation of a layerwise model to analyze laminated structures with elastic-plastic interfaces made up of a thin layer of an isotropic material. This model is called the M4-5N model. An approximation of the 3D strains and its integration through the thickness of the thin layer provided the displacement discontinuities across the imperfect interface. The equations of the model were solved by means of a Newton-Raphson-like technique and a finite element method in the case of a plane strain state. A first validation of the model and its numerical tool was proposed by comparing the results of the model to those of a 3D finite element model applied to a double lap adhesively bonded joint with an elastoplastic adhesive. The cumulative plastic strains, the interfacial stresses and the displacement discontinuities were accurately predicted by the M4-5N model. In spite of this, Aquino de Los Rios et al remarked the necessity to provide a more rigorous theoretical support of the proposed equations of interlaminar plasticity. This rigorous determination should evoke the Hellinger Reissner functional and the approximation of 3D stresses which is the starting point of the M4-5N model and not the approximation of 3D strains and displacements. Actually, the original elastic model developed in [13] [14] does not make any approximation of 3D strains and displacements. The layerwise model proposed by Aquino de los Rios et al was adopted by Duong et al in [15] to develop a layerwise finite element for laminates with imperfect interfaces in a general 3D case (not only the plane strain state assumed in [12] for the numerical resolution of the equations).

In this project, a rigorous theoretical support and an enhancement of the equations of interlaminar plasticity obtained by Aquino de los Rios et al [12] were proposed. The enhancement consists on a better description of the stress field in the adhesive and taking into account the out-of-plane Poisson's effect which is neglected in most plate theories. To obtain the equations of the enhanced model of laminates with imperfect interfaces, two steps are proposed (see Figure 66). In the first step, a version of the M4-5N model where the thin adhesive layers are modelled as layers is obtained by applying an asymptotic

expansion method. In the second step, the equations in the previous step are arranged to obtain the equations of the model with imperfect interfaces.

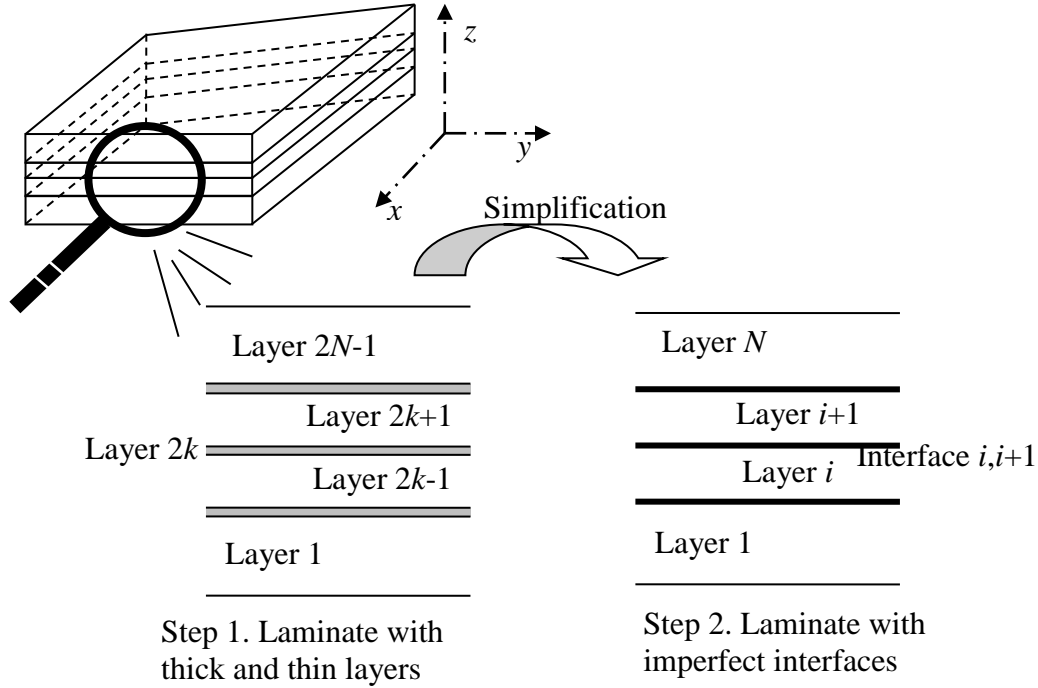


Figure 66. Laminated structure considered and two steps for its modeling.

A laminate made up of  $N$  thick layers bonded by  $N-1$  thin layers is considered (see step 1 in Figure 66). The layers are numbered as shown in Figure 1. An odd number corresponds to a thick layer whereas an even number indicates a thin layer. The interfaces between thin and thick layers are perfect. The thick layers are made up of an orthotropic elastic material whereas the thin ones are made up of an elastic-plastic isotropic material. The thin adhesive layers are modeled as imperfect interfaces across which displacement discontinuities exist (see step 2 in Figure 66).

The construction of the model starts with an approximation of the stress field  $\sigma^*$  in each layer by means of  $z$ -polynomials. The coefficients of these polynomials are the generalized

forces, moments and interfacial stresses [11]. Then this stress approximation is introduced into the Hellinger-Reissner functional. Assuming that volume forces are negligible, the Hellinger-Reissner functional for elastic problems applied to the laminate is:

$$H.R.(\mathbf{U}^*, \boldsymbol{\sigma}^*) = \sum_{m=1}^{2N-1} \int_{\Gamma} \int_{h_-^m}^{h_+^m} \left[ \sigma_{op}^* (\varepsilon_{op}(\mathbf{U}^*) - \varepsilon_{op}^p) - \frac{1}{2} \sigma_{op}^* S_{opqr} \sigma_{qr}^* \right] dz d\omega + F(\mathbf{U}^d, \mathbf{T}^d) \quad (21)$$

where  $\varepsilon_{op}^p$  is the  $op$  component of the plastic strain tensor  $\boldsymbol{\varepsilon}^p$  (it is zero in the thick layers),  $\mathbf{U}^*$  is a piecewise  $C^1$  first order tensor field,  $\boldsymbol{\sigma}^*$  is a piecewise  $C^1$  second order symmetric tensor field,  $F(\mathbf{U}^d, \mathbf{T}^d)$  is a boundary integration term which involves the imposed displacement vector  $\mathbf{U}^d$  and stress vector  $\mathbf{T}^d$  at the boundaries of the structure.

Generalized displacements and strains in each layer are then identified by making use of the  $H.R.$  functional. The variational property of the  $H.R.$  functional with respect to the generalized displacements of the thick layers yields the generalized equilibrium and boundary conditions established in the original elastic model [14]. These equilibrium equations involve the generalized forces, moments and interfacial stresses. The variational property of the  $H.R.$  functional with respect to the generalized forces and moments yield the generalized elastic equations. A pertinent asymptotic expansion method provides the generalized displacements, displacement discontinuities and stresses at the “interface layers”. An analysis of the power dissipated by plasticity and the generalized stresses provides the generalized plastic flow rules and yield functions. The asymptotic expansion method yields a generalized interfacial cumulative plastic strain and the generalized plastic strains which allow to define the plastic displacement discontinuities at the interfaces.

The model equations are solved by making use of a finite element technique and a Newton-Raphson-like method.

## 2.2 Theoretical validation

Let us now make a theoretical validation of the model by comparing its results to those of a solid finite element (FE) resolution performed by the commercial software called COMSOL Multiphysics 3.1. A first validation (not shown in this paper) consists on considering the case of a double-lap joint subjected to a tensile load (the same case was considered by Aquino de los Rios et al [12]). In this case, the adhesive is subjected essentially to a shear loading and the enhanced version of the model yields practically the same results as those of the previous one and both are very similar to the solid finite element results. For simplicity sake, this case is not shown in this report. Let us now consider the case of a peel dominated loading. The structure considered is a T-peel joint (see Figure 67) with elastic steel substrates and an elastic-plastic adhesive which plastic behavior is modeled by a Von-Mises yield function, a normal flow rule and an associative plasticity consideration. The width of the joint is 25mm. The material properties are shown in Table 8. A plane strain state is assumed. In Figure 68, the mesh considered in the solid FE calculation is shown; let us point out the high number of elements required due to the important difference in thicknesses for the adhesive and the adherend. In order to apply our layerwise model to analysis of this joint, symmetry is applied as shown in Figure 67. At the left end of the adherend, a force  $F$  and a bending moment  $M = b \times F$  are applied. A monotonic load  $F$  is considered. According to Castagnetti et al [16], this joint fails for a 487.5N load. A reasonable set of load values to be considered is then  $F=118\text{N}$  (when plasticity initiates for the layerwise model),  $F=300\text{N}$  and  $F=500\text{N}$ . The generalized stresses calculated by the M4-5N model at the “interface layer” are compared to the stresses calculated by COMSOL in the adhesive at the symmetry axis (the y-axis, see Figure 67). It is not worthy to use in this comparison the stresses calculated by COMSOL at the adhesive/steel interface because the left edge exhibits singularities.



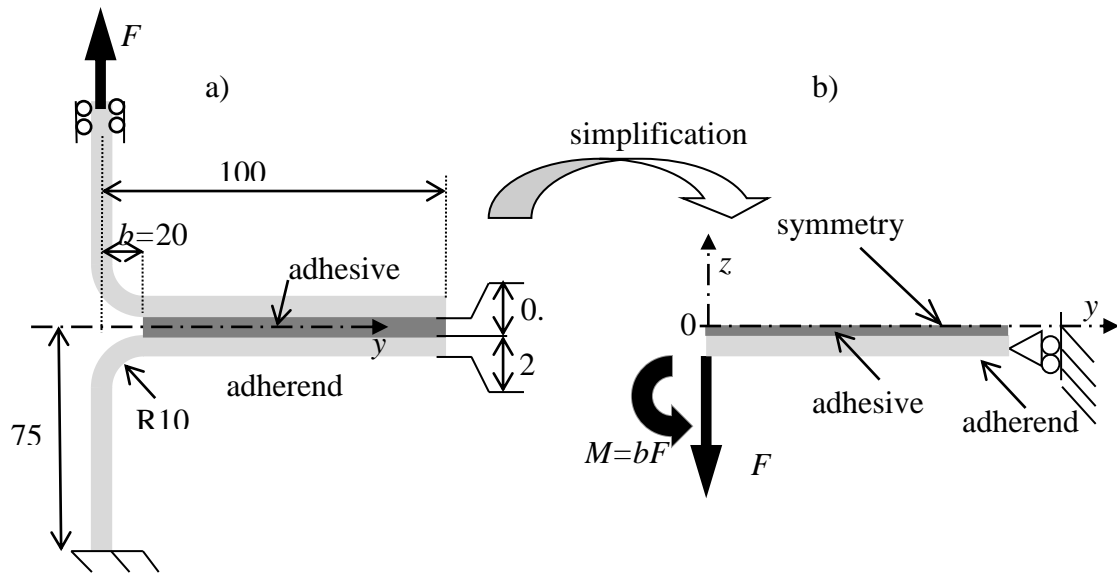


Figure 67. T-peel joints: geometry a) and modeling b) (dimensions are in mm).

Property \ Material	Adhesive	Adherend
Young's modulus (GPa)	1.7	206
Poisson's ratio	0.3	0.3
Yield stress (MPa)	30	

Table 8. Properties of involved materials.

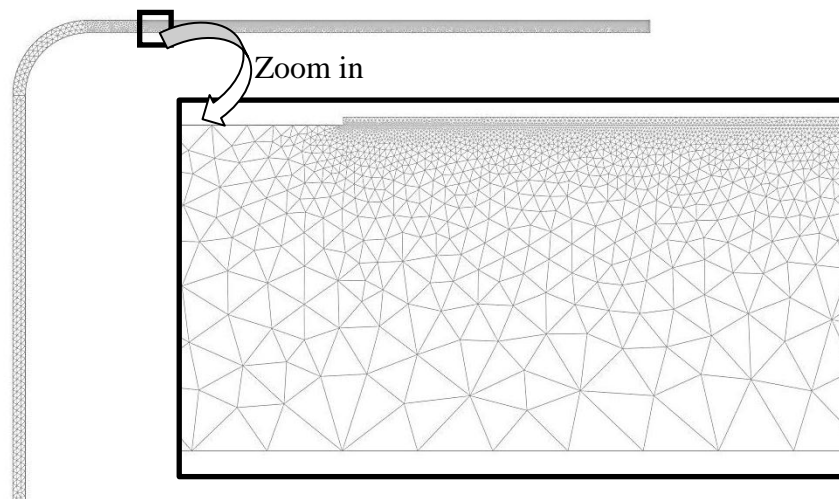


Figure 68. Meshed geometry in COMSOL.

In Figure 69, the equivalent Von-Mises stresses  $\sigma^{eq}$  in the adhesive calculated by the M4-5N model and COMSOL are plotted against the y coordinate for the three load levels considered. At a 118N, the equivalent stress calculated by the M4-5N model at the left edge reaches the yield stress and plasticity onset is predicted. For the three considered loads, an excellent agreement between the two calculation techniques is observed.

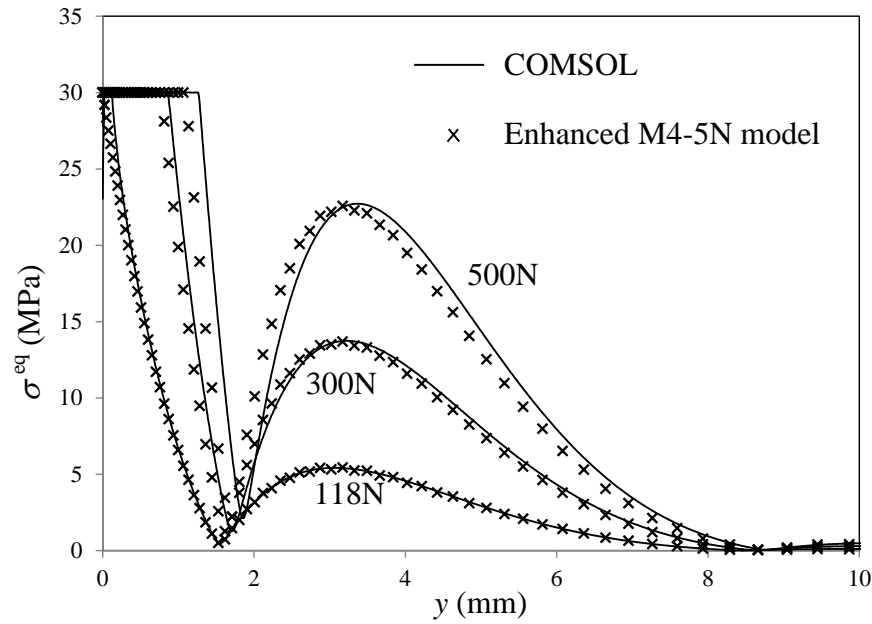


Figure 69. Equivalent  $\sigma^{eq}$  stress in the adhesive for three loads (118, 300 and 500N).

In Figure 70, the normal stresses  $\sigma_3$  in the adhesive calculated by the M4-5N model and COMSOL are plotted against the y coordinate. Once again, a very good agreement between the two calculation techniques is observed. Let us point out that these stresses reach much higher values (up to 188MPa) than the yield stress (30MPa) because the presence of the other normal stresses  $\sigma_1$  and  $\sigma_2$  reduces the equivalent stress level (the hydrostatic stress does not affect the equivalent stress). In Figure 71, the normal stresses  $\sigma_2$  in the adhesive computed by the two calculation methods are plotted against the y coordinate. The solid FE

(COMSOL) values at the left edge for this stress are zero ( $\sigma_2 = 0$ ) because of the free boundary condition. This condition is not verified by the  $\sigma_2$  stress of the M4-5N model since the adhesive is modeled by an interface. This causes a slight difference between the values of the normal stresses near the left edge. In spite of this, the M4-5N results are very accurate over a wide range in the adhesive. For the other stress  $\sigma_1$  in the adhesive, the layerwise model and COMSOL provide also very similar results.

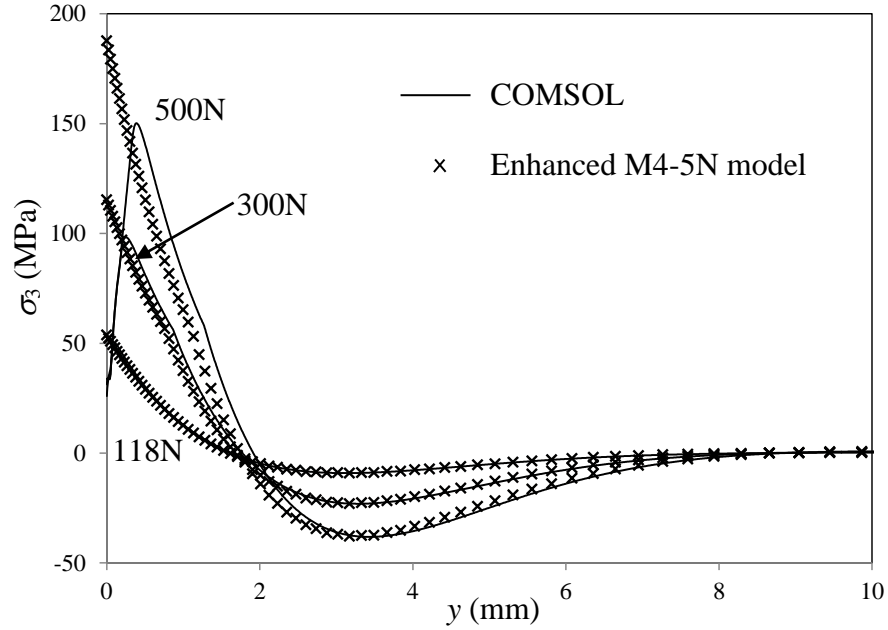


Figure 70.  $\sigma_3$  stress in the adhesive for three loads (118, 300 and 500N).

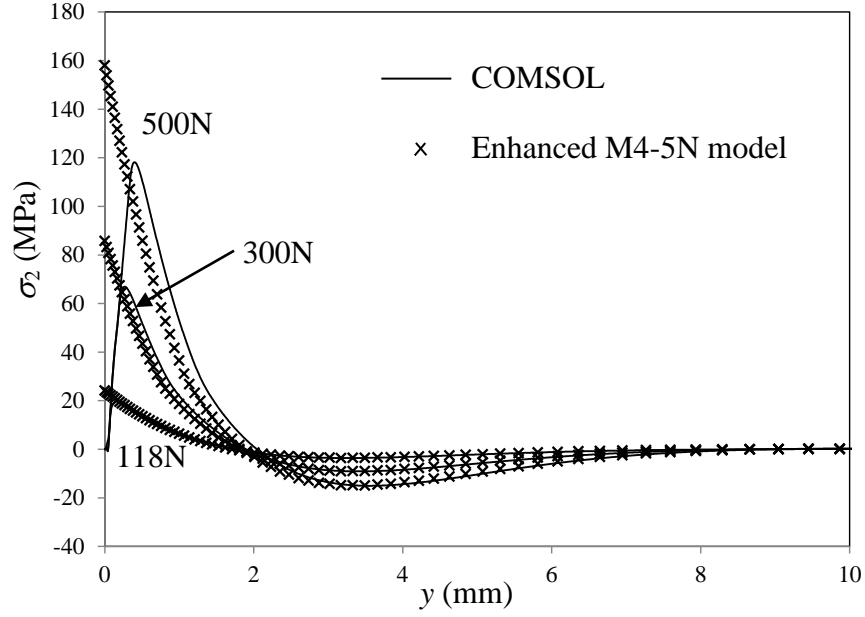


Figure 71.  $\sigma_2$  stress in the adhesive for three loads (118, 300 and 500N).

Let us now compare the predictions of the opening displacement  $\gamma_3$  at the imperfect interface of the M4-5N model to the elongation  $e$  in the thickness direction of the adhesive computed by COMSOL ( $e = -2v$  where  $v$  is the displacement of the interface in the  $z$ -direction according to the drawing in Figure 67). In Figure 72, these displacements are plotted against the  $y$  coordinate for the three load levels considered. Once again, very accurate results are observed for the M4-5N model.

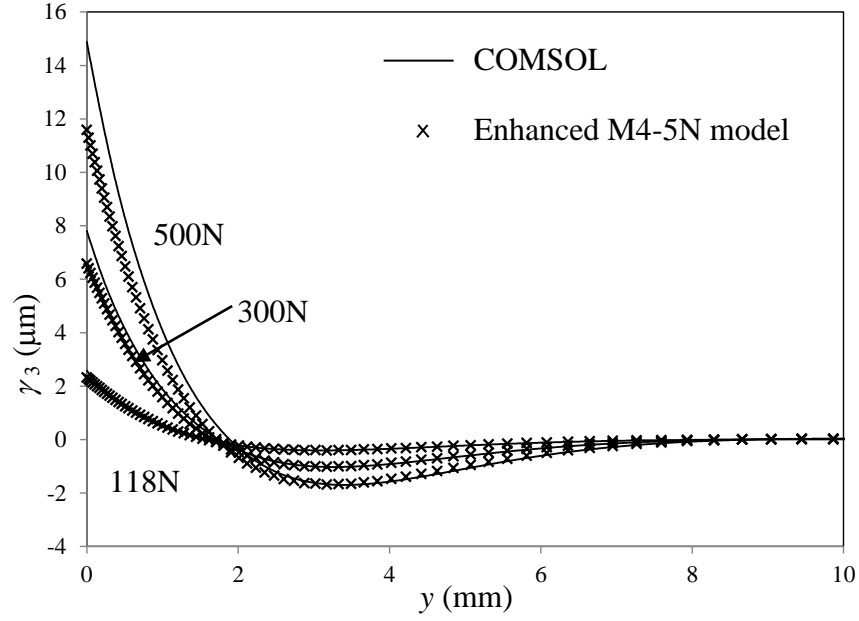


Figure 72. Elongation  $\gamma_3$  in the thickness direction of the adhesive layer for three loads (118, 300 and 500N).

Finally, let us compare the results of the new version of the M4-5N with those of the previous one developed by Aquino de los Rios et al in [12]. In the previous version of the M4-5N, the sole peel stress  $\sigma_3$  controls plasticity onset for the T-peel joint and  $\sigma_3$  cannot overpass the yield stress (the in-plane stresses  $\sigma_1$  and  $\sigma_2$  were not taken into account). In Figure 73, the normal stresses  $\sigma_3$  in the adhesive calculated by the two versions of the M4-5N model and COMSOL are plotted against the  $y$  coordinate for the 500N load. An important difference between the predicted peel stress values by the two versions is observed. A comparison of the predictions of the two models with those of COMSOL allows us to state that in the case of a peel dominated loading, the previous M4-5N model yields erratic results whereas the enhanced layerwise model provides very accurate results.

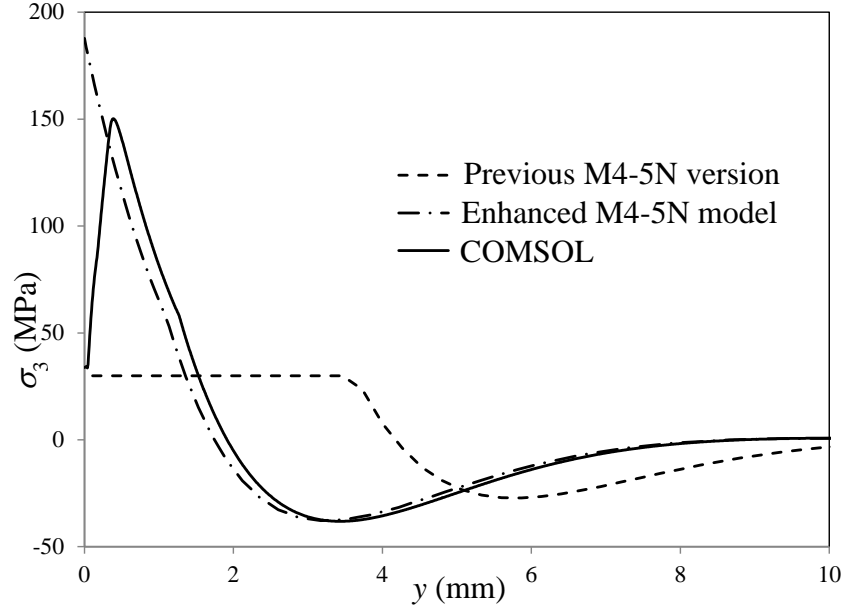


Figure 73.  $\sigma_3$  stress in the adhesive for a 500N load calculated by COMSOL and the two versions of the M4-5N model.

Additionally to the accuracy of the enhanced version of the model, the layerwise technique has the quality to perform the calculations faster (at least 30 times faster than the solid FE technique for the structure above considered) and with less memory requirements.

### 2.3 Experimental validation

In [12], a comparison of the model results with the interlaminar sliding observed by Diaz and Caron [17] at the free edge of cross-ply carbon-epoxy laminates subjected to a tension load was proposed to identify the model parameters and test the accuracy of the model. In these laminates the “interface layer” was a thin matrix layer and its properties appearing in the model were those of an elastic, perfectly plastic material: the Young's modulus, the Poisson's ratio and the yield stress. In these experiments the interlaminar sliding was uniform along the edge of the laminate and was mainly due to interfacial shear stresses. The

interface properties were obtained by predicting the interfacial sliding and fitting the plot of the measured sliding against the tensile load. A good prediction of the plot was observed.

In the present paper, more complex experimental observations and measurements in adhesive joints are used to validate the enhanced layerwise model. The experiments carried out by Chataigner et al. in [18] consisted on tensile tests on double lap adhesive joints with an elasto-plastic adhesive exhibiting important plastic strains prior to adherend failure. The UD carbon epoxy adherends were bonded with an epoxy adhesive. The properties of the involved materials are shown in Table 9. In Figure 74, the behavior of the adhesive subjected to a tensile load is shown. Plasticity with hardening is observed. The geometry of the adhesive joints is shown in Figure 75. In order to ease the measurement of the sliding between the inner and outer adherends, vertical lines were drawn along the lap length as shown in Figure 75 and Figure 76. As will be shown later, the sliding is not uniform along the adhesive length.

Property \ Material	Adhesive	Adherend
Young's modulus (GPa)	2.5	162 (fibre direction) 10.6 (transverse direction)
Poisson's ratio	0.3	0.3
Out-of- plane shear modulus (GPa)		4.1

Table 9. Elastic properties of involved materials [18].

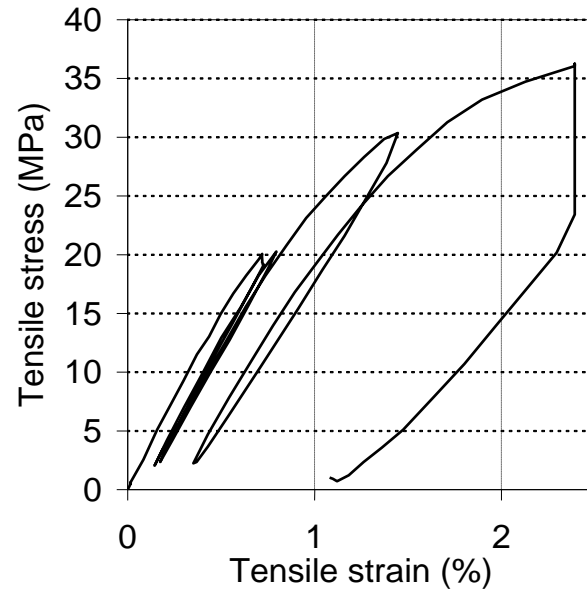


Figure 74. Stress strain curve of the elasto-plastic adhesive [18].

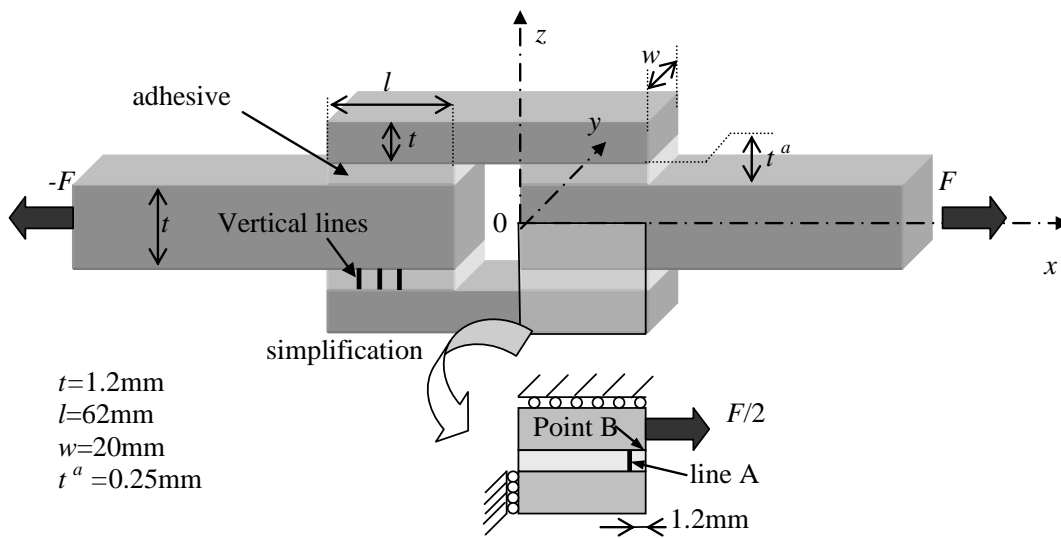


Figure 75. Geometry of the double lap joint and boundary conditions.



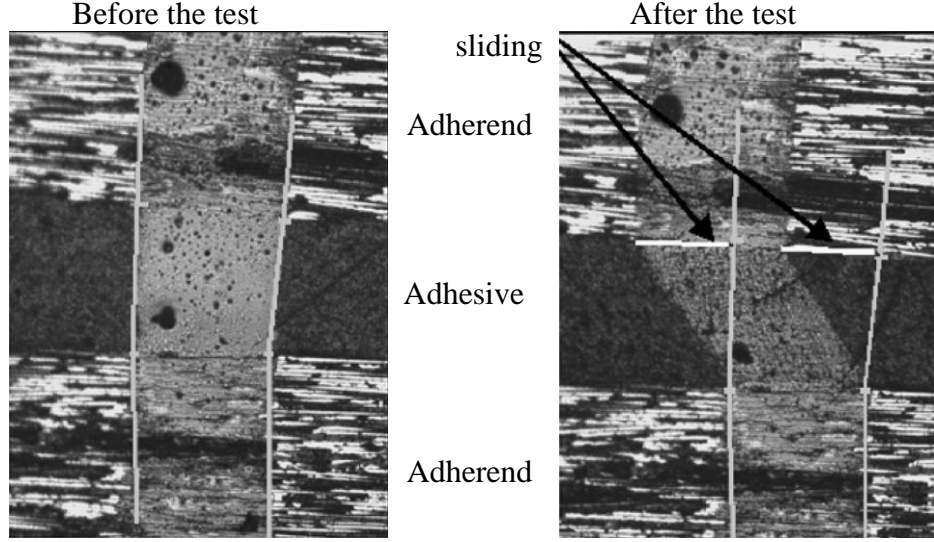


Figure 76. Measuring the sliding between adherends [18].

With our layerwise model, owing to its small thickness, the adhesive layer is modeled as an imperfect interface. The predicted displacement discontinuity  $\gamma_1$  across the imperfect interface is to be compared to the measured sliding between adherends. The stress state at the imperfect interface is deduced from the generalized stresses:

- the in-plane normal stresses are  $\sigma_{xx} = \sigma_1$  and  $\sigma_{yy} = \sigma_2$
- the in-plane shear stress is  $\sigma_{12}$
- the peel stress is  $\sigma_3$
- the out-of plane shear stresses  $\sigma_{xz} = \tau_{13}$  and  $\sigma_{yz} = \tau_{23}$ .

These generalized stresses are  $z$ -independent.

It is well known that the adhesive behavior may exhibit a strong dependence on the hydrostatic stress and that a Drucker-Prager-like model would predict it accurately. This type of model would require more tests for the parameters identification. For the sake of simplicity, an elastic-plastic model with isotropic hardening is adopted in this paper. The yield function is

$$f(\boldsymbol{\sigma}) = \sigma^{eq} - Kp^a - \sigma_0 \quad (22)$$

where  $\sigma^{eq}$  is the equivalent Von-Mises stress in the “interface layer”;  $K$ ,  $a$ , and  $\sigma_0$  are properties of the adhesive which are identified by fitting the experimental curve in Figure 1. After identification we obtain  $K=60\text{MPa}$ ,  $a=0.2$  and  $\sigma_0=11\text{MPa}$ . A plane strain state is assumed. The considered geometry and the boundary conditions are shown in Figure 75.

In Figure 77, the experimental and theoretical slidings are plotted against the position  $x$  along the lap length for a load of 26KN. It can be observed that the sliding is not uniform along the lap length and the layerwise model provides accurate predictions of the sliding. In Figure 78, the applied load is plotted versus the sliding deduced from line A in Figure 75 (located at 1.2mm from the end). One may observe that the sliding at the given point is not proportional to the applied load (plasticity has an important effect). Once again, the layerwise model provides very accurate predictions.

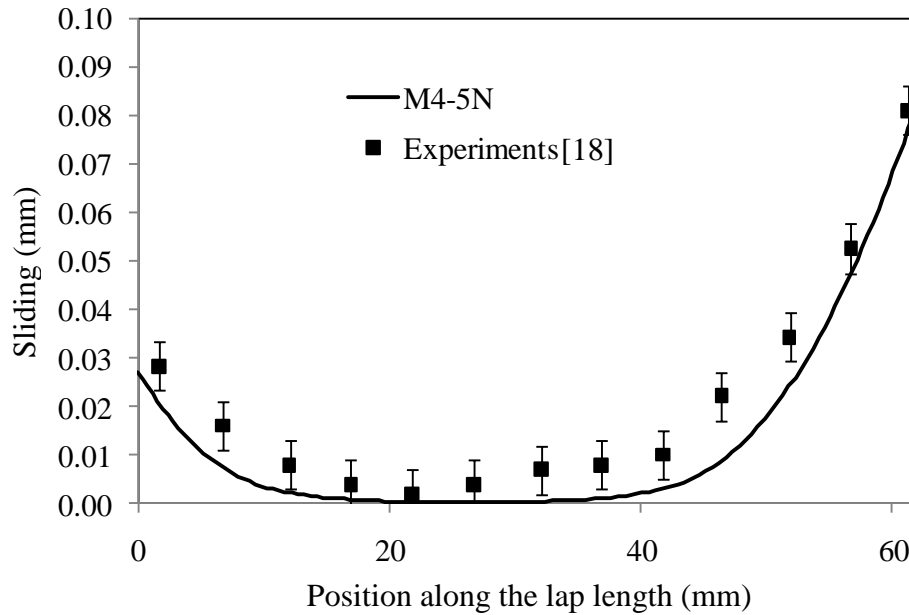


Figure 77. Slidings along the lap length (experiments [18] and predictions).

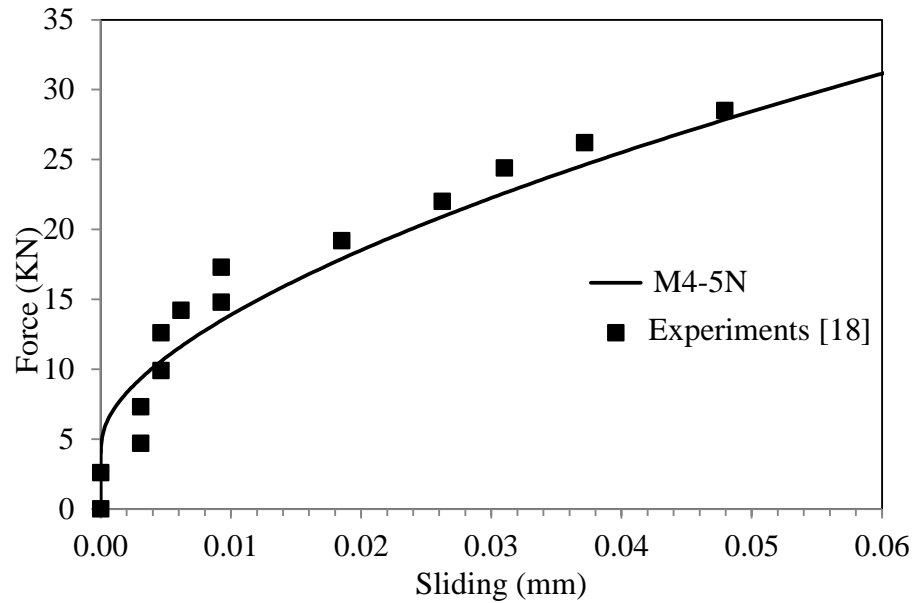


Figure 78. Applied force vs. slidings on line A in Figure 2 (experiments [18] and predictions).

It is clear that the evaluation of the accuracy of the model in the present paper uses more complex results than those used by Aquino de los Rios et al in [12]. Moreover, in the present paper, the interface properties are obtained from bulk material tests instead of an identification based on fitting the sliding measurements.

### 3. Conclusions

A solid finite element analysis was proposed to compute stresses in the specimens tested in this project. COMSOL software was used to perform these calculations and a preliminary viscoplastic model for the adhesive was implemented. Owing to a case study, our capacity to carry out a structural analysis for adhesive joints having an adhesive with a viscoplastic

behavior was proved. Once the final 3D constitutive model for the adhesive will be obtained, it will be implemented in COMSOL so as to predict the behavior and stresses in adhesive joints. This task will be carried out on 2013.

In the case of plate-like adhesive joints, a solid finite element method is not the best option to their structural analysis. An operational layer-wise model was proposed to calculate stresses in adhesive joints with elastoplastic adhesives. The final 3D constitutive model of the viscoplastic adhesive will be implemented in the layer-wise model on 2013.

The methods described in this chapter to compute stresses and strains are applied in the next chapter to predict failure onset.

## **IV. Failure prediction**

Failure prediction usually starts by analyzing linear elastic structures so as to simplify the analysis and state that the only dissipative process is fracture. When non-linear phenomena such as plasticity occur prior to failure initiation linear analysis may not provide accurate predictions. In this project, failure prediction by means of a linear analysis is first considered. Then, some non-linear failure prediction strategies are shown when considerable non-linear phenomena take place before failure onset. It is worth mentioning that a paper describing the failure prediction of interfaces within linear elastic structural adhesive joints has been submitted for publication in the International Journal of Adhesion and Adhesives.

### **1. Predictions based on a linear analysis**

The only type of failure considered in this section is adhesive failure (failure at the interface between the adhesive and the substrates).

#### **1.1 Selection of a failure criterion**

Recently, Cognard et al. [9] made a modification of the classical Arcan test in order to vanish the edge effects and to cause failure at the center of adhesive joints. The authors tested several load directions and observed both adhesive and cohesive failures. In Figure 79, the failure envelope obtained for aluminum substrates and an epoxy adhesive (Vantico Redux 420) is shown. In this Figure 79,  $\tau$  and  $\sigma$  are the interfacial shear and normal stresses, respectively. A moderate scattering of results is observed. We assume that the failure is initiated by an interfacial crack. It is clear that the experimental values are best

fitted by a parabola rather than an ellipse (see Figure 79). For this reason, we select the following stress criterion to predict stress controlled failures:

$$\tau^2 + a\sigma = \tau_c^2 \quad (23)$$

where  $a$  and  $\tau_c$  are interfacial properties. Let us point that out that the strength predicted by this criterion is sensitive to the sign of the peel stress, the same as the experiments performed by Cognard et al [9]. A classical quadratic stress criterion is not able to predict this sensitivity and in spite of this, several authors apply this criterion to predict interfacial failures.

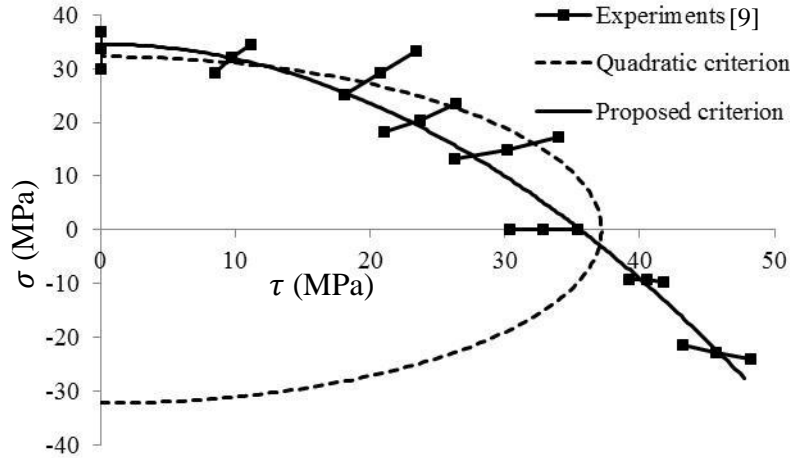


Figure 79. Failure envelope of the adhesive joints tested in [9].

In real world applications, stress singularities exist at the intersection of interfaces with edges and a sole maximum stress criterion is not suitable to predict failure because the failure criterion is verified at the stress singularity points for any load applied. Also, it is well known that a criterion involving a differential strain energy release rate is not suitable to predict failure initiation because the strain energy release rate tends to zero for vanishing cracks. Leguillon et al [19] proposed an original approach to predict free edge delamination initiation in composite laminates by making use of an energy criterion. Failure onset is

associated by the appearance of a non-zero length crack. This crack appears in an unstable manner and Leguillon proposes to use the following energy criterion:

$$G^{\text{inc}} = -\frac{W_p(A) - W_p(0)}{A} = G^c \quad (24)$$

where  $A$  is the area of the crack,  $W_p(A)$  is the potential energy in the cracked structure,  $W_p(0)$  is the potential energy in the uncracked structure,  $G^{\text{inc}}$  is the incremental strain energy release rate and  $G^c$  is the critical strain energy release rate (a property of the interface related to its toughness). Notice that  $G^{\text{inc}}$  is equivalent to the strain energy release rate when  $A$  tends to zero. In [20], Leguillon proves then that a sole criterion (an energy criterion or a maximum stress criterion) do not suffice to predict failure onset in any geometry or loading condition. The author proves that in order to create a crack of area  $A$ , the following conditions must be met simultaneously:

- the incremental strain energy condition in equation (24),
- the stress criterion  $f(\tau, \sigma) = 0$  at every point where the crack appears;

where  $\tau$  and  $\sigma$  are the interfacial shear and normal stresses, respectively. In [21], Martin et al show that the use of the previous twofold criterion predicts accurately thickness and stacking sequence effects on delamination initiation in cross-ply composite laminates.

In this section, a spontaneous crack connected to a stress singularity point causes failure onset. In order to predict a spontaneous crack of surface  $A$ , Leguillon's approach [20] is adopted and the following twofold criterion is considered:

$$\begin{cases} G^{\text{inc}}(A) = G^c \\ \tau^2 + a\sigma = \tau_c^2 \end{cases} \text{ at every point of surface } A \text{ just before failure onset} \quad (25)$$

where  $G^{\text{inc}}$  is the incremental strain energy release rate;  $G^c$ ,  $a$ ,  $\tau_c$  are material parameters that will be determined by fitting the theoretical predictions to the experimental results obtained in chapter II.

## 1.2 Example of a failure prediction and determination of the failure parameters

### 1.2.1 Example of a failure prediction

The method to predict failure initiation is described by analyzing the example of a type A specimen made of steel substrates and the polyester resin as adhesive. For the other specimens, an analogue method is applied. The following parameters are chosen to carry out the failure prediction:  $\tau^c = 13.0\text{MPa}$ ,  $a = 15.2\text{MPa}$  and  $G^c = 52\text{J/m}^2$ . A monotonically increasing proportional loading is considered. The torque  $T$  and the axial tension force  $F$  are thus defined by:

$$F = Q \cos(\alpha) \bar{F} \text{ and } T = Q \sin(\alpha) \bar{T}, \quad (26)$$

where  $\alpha$  is a constant defining the loading direction,  $Q$  is an adimensional loading parameter,  $\bar{F} = 0.1\text{KN}$  and  $\bar{T} = 1\text{Nm}$ . In this example,  $\alpha = 84.3^\circ$ .

The prediction of failure onset requires the calculation of interfacial stresses in uncracked specimens. By means of the results of the finite element software COMSOL it is possible to determine the interfacial stresses for each value of the radial position  $r$ . For tests A, the distance to the free edge is thus defined by  $\rho = \frac{D}{2} - r$  (see Figure 80). Let us define the critical load  $Q^\sigma$  (from a stress criterion point of view) as the minimum positive load required to obtain:

$$\sqrt{\sigma_{rz}^2(\rho) + \sigma_{\theta z}^2(\rho) + \alpha \sigma_{zz}(\rho)} = \tau^c \quad (27)$$



In Figure 81, the critical load  $Q^\sigma$  is plotted versus the distance  $\rho$  to the edge. It is worth mentioning that  $Q^\sigma$  tends to zero when  $\rho$  tends to zero. If the model assumes that only the strength criterion governs failure, it would predict meaninglessly that any load would cause failure initiation.

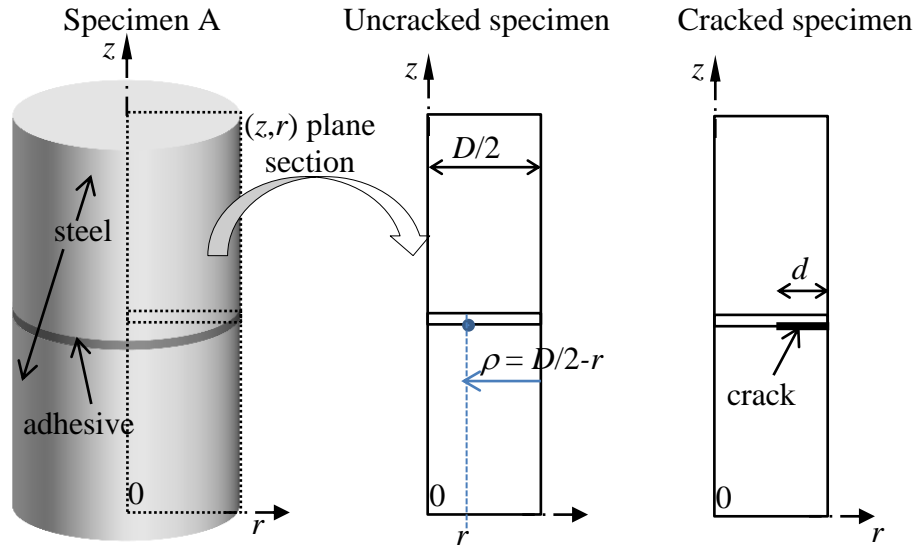


Figure 80. Notations for the example of a specimen A.

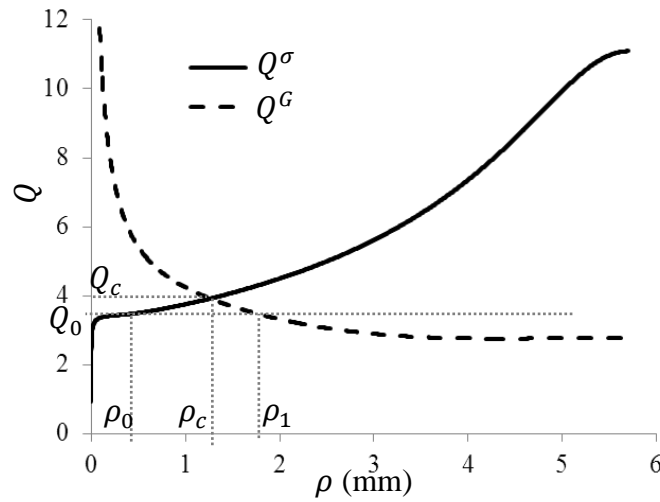


Figure 81. Critical load parameters vs. crack depth or distance to the edge.

The prediction of failure onset requires also the computation of strain energies in cracked specimens so as to determine the incremental strain energy release rate  $G^{\text{inc}}$  in equations (24) and (25). The incremental strain energy release rate  $G^{\text{inc}}$  is defined by [19], [20]:

$$G^{\text{inc}} = -\frac{W_p(d) - W_p(0)}{A(d)} = G^c \quad (28)$$

where  $W_p(0)$  is the potential energy in the uncracked specimen,  $W_p(d)$  is the potential energy in the specimen with a crack of depth  $d$ ,  $A(d)$  is the area of the crack. The crack depths are measured from the points which exhibit a higher stress concentration. For a type A specimen, a circumferential crack with a depth  $d$  in the radial direction is considered (see Figure 80). For the other types of specimens, rectangular cracks with a depth  $d$  measured from the specimens edge are considered as shown in Figure 82. It is worth mentioning that only one interfacial crack is modelled for each specimen. In Figure 83, the example of the meshing of a cracked type A specimen is shown. Owing to COMSOL calculations, for a given loading parameter  $Q_1$ , the incremental strain energy release rate  $G_1^{\text{inc}}(\rho)$  related to an interfacial crack connecting the free edge of the specimen A and a point located at the radial position  $r = \frac{D}{2} - \rho$  is calculated ( $\rho = d$ ). The critical load  $Q^G(\rho)$  required to obtain  $G^{\text{inc}}(\rho) = G^c$  is then

$$Q^G(\rho) = Q_1 \sqrt{\frac{G^c}{G_1^{\text{inc}}(\rho)}}. \quad (29)$$

This critical load  $Q^G(\rho)$  (from an energy point of view) is the minimum load required to create a spontaneous interfacial crack of depth  $\rho$ . In Figure 81, the critical load  $Q^G(\rho)$  is plotted versus the depth  $\rho$ . If only the energy criterion  $G^{\text{inc}} = G^c$  governed failure initiation, the load that would cause failure would be  $Q^G\left(\frac{D}{2}\right)$  and the crack would separate

the specimen into two pieces. Nevertheless, the stress condition for breaking the whole interface is not met since  $Q^G\left(\frac{D}{2}\right) < Q^\sigma\left(\frac{D}{2}\right)$ .

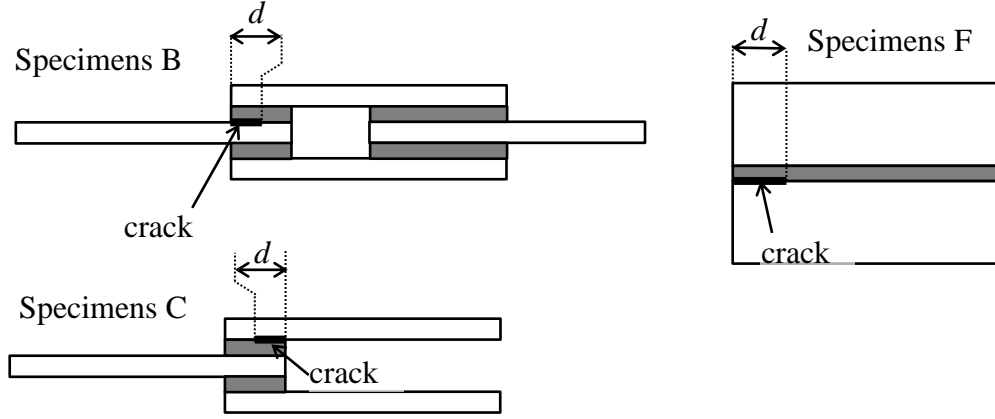


Figure 82. Configuration of cracks considered to compute  $G^{\text{inc}}$ .

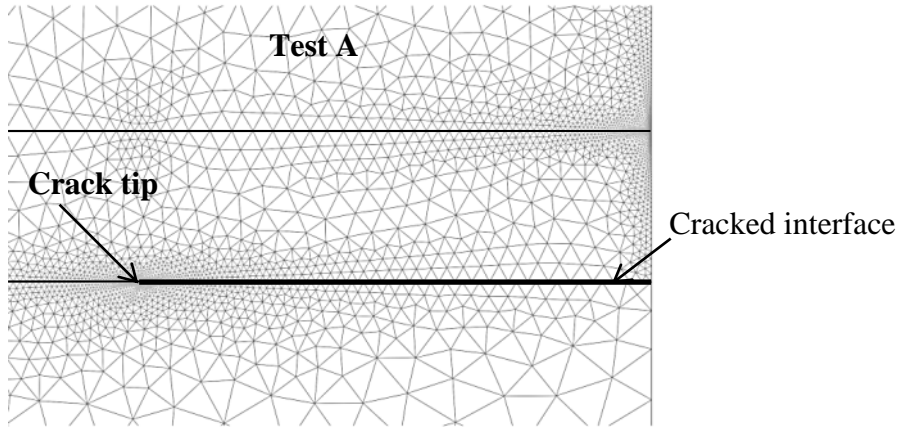


Figure 83. Mesh for a cracked type A specimen

Now, let us analyze failure initiation by making use of the stress and energy criteria simultaneously. In Figure 81, we observe that the curves of  $Q^G$  and  $Q^\sigma$  intersect at  $\rho = \rho_c = 1.26\text{mm}$  and  $Q = Q_c = 3.92$ . For a loading level  $Q_0$  ( $Q_0 < Q_c$ ), a small crack

(depth  $\rho_0 < \rho_c$ ) may appear from a stress point of view but this crack would not release enough energy to verify the energy criterion since  $Q^G(\rho_0) > Q^\sigma(\rho_0)$ . Besides, for this same value of the load parameter  $Q = Q_0$  the load may be enough to create from an energy point of view a larger crack of depth  $\rho_1$  but not from a stress point of view since the stress criterion is not verified for  $\rho > \rho_0$  (see Figure 81). Now, if the load parameter  $Q$  increases and attains  $Q_c$ , the load is enough to create a  $\rho_c$  deep crack from stress and energy point of views. The value of the load parameter that would cause failure initiation is then  $Q_c = 3.92$  (i.e.  $F = 0.392\text{KN}$ ,  $T = 3.92\text{Nm}$ ).

It is worth mentioning that in the above example the curves of  $Q^G$  and  $Q^\sigma$  intersect. If in a particular prediction this does not happen (the curve of  $Q^G$  would be above the curve of  $Q^\sigma$  for any crack size), the stress condition would be met at any point of the interface before the fulfillment of the energy condition. The minimum value of  $Q^G$  would provide the critical load that would cause failure onset.

### ***1.2.2 identification of the failure parameters***

Parameters  $G^c$ ,  $a$  and  $\tau_c$  are determined by fitting the predictions to the experimental data and applying a least square method. The values of these parameters are

- $\tau^c = 13.0\text{MPa}$ ,  $a = 15.2\text{MPa}$  and  $G^c = 52\text{J/m}^2$  for the steel/polyester specimens
- $\tau^c = 19.7\text{MPa}$ ,  $a = 23.2\text{MPa}$  and  $G^c = 6.6\text{J/m}^2$  for the D609/steel specimens

### 1.3 Failure prediction for the tested adhesive joints

#### 1.3.1 Polyester/steel specimens

The failure envelope for tests A predicted by the twofold criterion is plotted in Figure 84. The criterion predicts correctly failure onset even for small positive axial forces. It seems that these predictions would have the same quality for negative axial forces. This will be confirmed in a subsequent study. In Figure 85, the experimental and theoretical forces that lead to failure of type B and C specimens are plotted against the overlap length  $l$ . Once again the predictions are accurate and lie within the range defined by the experimental data. Thus, the twofold criterion in equation (25) provides good quality predictions of failure and not only for butt joints but also for double lap joints.

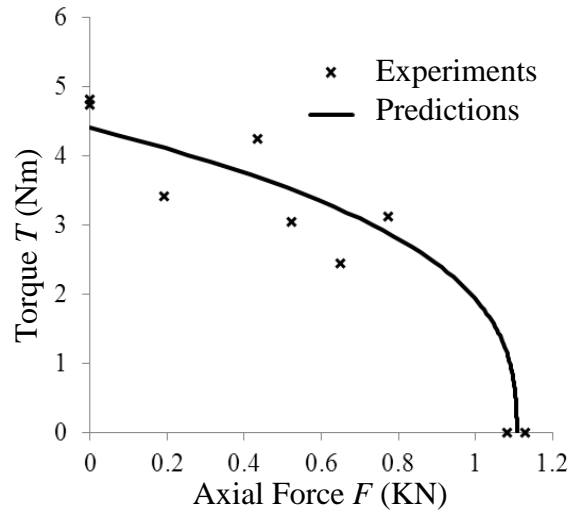


Figure 84. Failure envelope for tests A

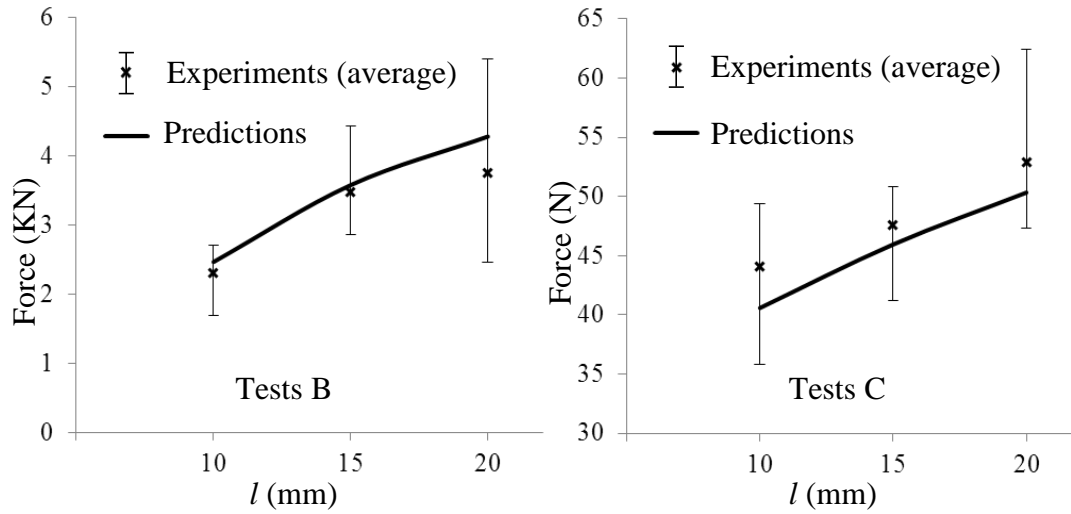


Figure 85. Experimental and theoretical failure loads vs. overlap length  $l$  (tests B and C).

### 1.3.2 D609/steel specimens

Let us first apply the results of tests D (ARCAN tests without edge effects). These tests will allow us to determine the interfacial stress criterion (adhesive failure was observed in these tests). Owing to COMSOL calculations and to the experimental values obtained in Table 5, the interfacial stresses predicted by the analysis at failure onset are obtained. In Figure 86, these stresses are plotted on the  $\tau$  vs.  $\sigma$  plane ( $\tau$  is the interfacial shear stress and  $\sigma$  is the interfacial normal stress). The points defined by these experimental results define a failure envelope which is best fitted by a parabola. The equation of this parabola defines the stress criterion:

$$0.04\tau^2 + \sigma = 16.7 \text{ MPa}. \quad (30)$$

This criterion does not suffice to predict failure onset when stress singularities exist (this is the case of tests E).

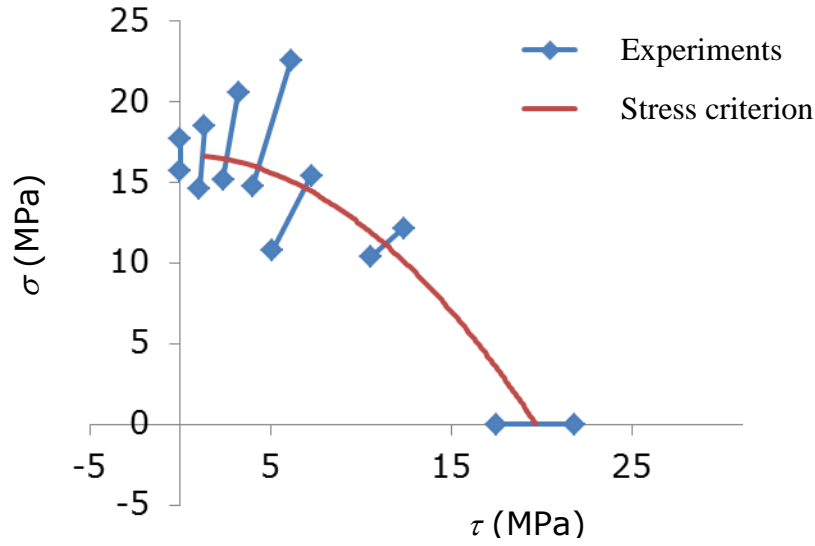


Figure 86. Experimental failure envelope (specimens D) and stress criterion.

The twofold criterion in equation (25) requires not only the determination of parameters involved in the stress criterion but also the parameters appearing in the energy criterion. Up to this point, the only parameter that is missing is the critical strain energy release rate  $G^c$ . For specimens E which exhibit stress singularities at the edges of the interfaces, an important scattering of results was observed. As already mentioned, this scattering may be due to the flaws in the specimens. The maximum size of the flaws observed in the specimens was 3mm. For these reasons, two modelling cases are proposed for the analysis and failure prediction of specimens E:

- The first considers a perfect specimen without flaws. The energy criterion applied is  $G^{inc} \geq G^c$ , where  $G^{inc}$  is the incremental strain energy release rate. With this modelling, the theoretical failure loads obtained should be greater than the experimental failure loads because physically all the specimens made contain defects.
- The second considers an existing interfacial flaw (a precrack). The size of this precrack is 3mm (this size corresponds to that measured for the largest flaw in the

tested specimens). The energy criterion applied is  $G \geq G^c$ , where  $G$  is the differential strain energy release rate. The theoretical failure loads obtained in this modelling should be lower than the experimental failure loads for specimens F because the theoretical analysis takes into account a greater flaw than the real ones.

The two conditions described above in the two types of modelling yield the bounds for the selection of the value of  $G^c$ . The best choice for the value of the critical strain energy release rate is  $G^c = 6.6\text{J/m}^2$ . In Figure 87, the obtained failure load predictions with the two modellings above are shown. The range of the experimental failure loads (provided in Table 6) is correctly predicted except for the  $75^\circ$  angle. The cause of this difference may be due to significant non-linearities

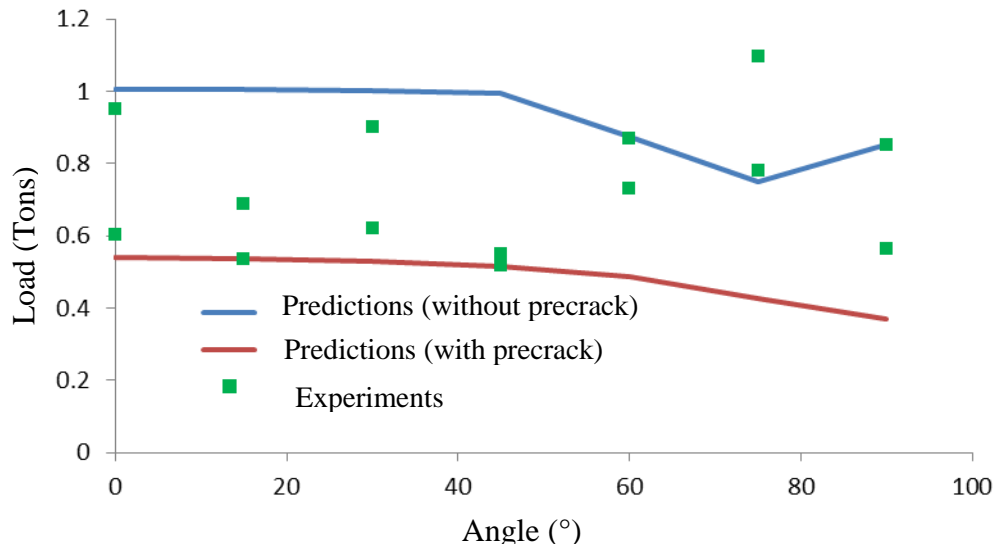


Figure 87. Failure load predictions for specimens E.

The predictions made in this subsection show how the twofold criterion may be applied to the failure onset prediction when an important scattering of critical loads is expected due to the presence of flaws. In this case, we have shown that the maximum expected size of flaws helps to determine a range in which the critical load values may lie.



## 2. Predictions based on a non-linear analysis

When important material non-linearities occur before failure onset, a correct modeling of the behavior of the materials is required in order to propose pertinent failure criteria and predict accurately failure onset. Few tests were performed in this case during this project (torsional tests with metal substrates bonded with E20HP and D609 adhesives) and since a correct model of these adhesives has not been obtained yet, other experimental results gathered from literature were employed to determine a failure criterion and make a failure onset prediction. The failures considered were failures within the adhesive layer (cohesive failure) and adherend failure. Two types of adhesive joints subjected to tension were studied: double lap composite joints and T joints. In both cases, the layer-wise model called *M4-5N* and presented in section 2 of chapter III was applied.

### 2.1 Failure of a family of composite double lap joints

In this subsection, we analyze once again the experimental results obtained by Chataigner et al [18] with double lap joints with an elastoplastic epoxy adhesive. The geometries and material properties were already described in section 2.3 of the previous chapter where the plastic sliding calculated by the model was compared to the experimental measurements. Three adhesive lengths were tested (62mm, 40mm and 20mm). In these joints, the failure initiation occurred at the inner composite adherends (delaminations within the adherend and near the composite/adhesive interface). Our model reveals that shear and normal stresses that would cause delamination reach their maximum at the vicinity of point B in Figure 75. These stresses and the interfacial stresses at the adherend/adhesive interface are practically the same. Let us now employ a Von-Mises-like criterion involving the out of plane stresses to predict delamination onset within the adherends:

$$\sqrt{\sigma_3^2 + 3\tau_{13}^2} - \sigma^f > 0 \quad (31)$$

where  $\sigma^f$  is the out-of plane strength of the adherend. The axial stress that leads to failure onset in the longer specimens is 1700MPa [18]. The model predicts 57MPa for the  $\sqrt{\sigma_3^2 + 3\tau_{13}^2}$  stress. We thus choose  $\sigma^f = 57\text{MPa}$  in our criterion for predicting failure for any other adhesive length. In Figure 6, the theoretical and experimental critical axial stresses are plotted against the adhesive length. In this Figure 6, we also added the plot of the predictions of Volkersen's theory [22] (a shear-lag model) widely used for adhesive joint design. This theory is based on linear elastic approximations of the stress field. The layerwise model reproduces accurately the experimental curve whereas the Volkersen's theory overestimates considerably the strength for small adhesive lengths. These results prove then that the model is suitable to predict a joint failure when plasticity in the adhesive layer is due predominantly to out of plane shear stresses.

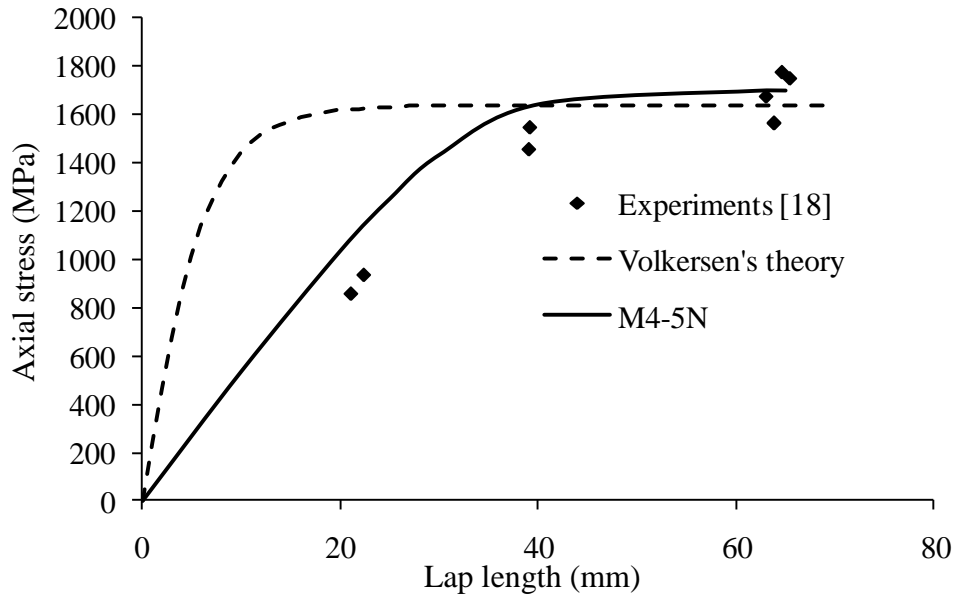


Figure 88. Critical stress vs. lap length (experiments [18] and predictions).

Let us point out that in this example the failure criterion in the adherend only considered delamination in the composite adherend layers. In a general case for composite adherends, the failure criterion should also be able to predict transverse cracking. The M4-5N model with a pertinent failure criterion offers the possibility to perform this task. For this, a more

complete characterization of the adherends is required in order to determine the critical generalized forces and stresses that would appear in the failure criterion.

## 2.2 Failure of a family of T-joints

In this subsection, we analyze the experimental results obtained by Castagnetti et al [16] with bonded T-peel joints. Steel adherends were bonded with an epoxy adhesive. The geometry of the specimens is shown in Figure 89 and the dimensions and notations of the coupons are detailed in Table 10. Two adherend thicknesses (2 and 3 mm) and two distances  $b$  (12 and 20mm) of the force axis to the left end of the adhesive were considered (see Figure 89). The adhesive thickness was  $s_a = 0.1$  mm and the specimen width was 25mm. The elastic properties of the materials involved are shown in Table 11. Five repetitions were performed for each specimen type. The averages of the failure forces (peak forces) measured during the tests are listed in Table 10. The specimens exhibited a cohesive failure.

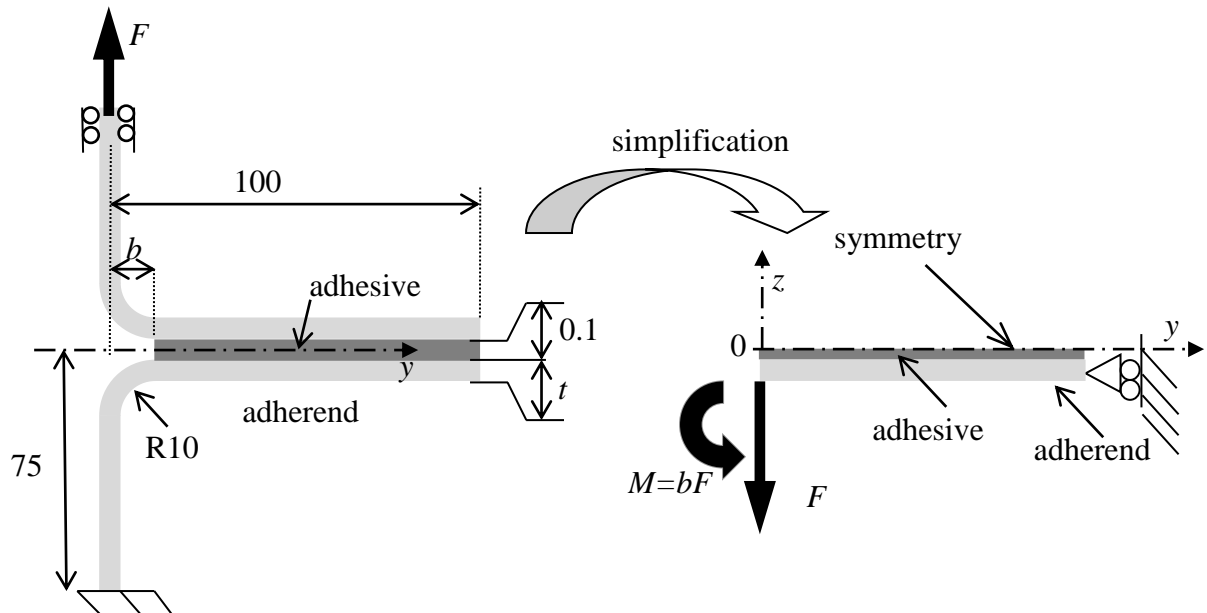


Figure 89. T-peel joints: geometry [16] and modeling (dimensions are in mm).

Specimen	1	2	3	4
$t$ (mm)	2	3	2	3
$b$ (mm)	20	20	12	12
$F$ (N)	487.5	779.2	794.5	1289.3

Table 10. Specimen notation, dimensions and failure forces [16].

	Steel	Adhesive
Young's modulus (GPa)	206	1.7
Poisson's ratio	0.3	0.3

Table 11. Elastic properties of the materials applied in the T-joints [16].

In order to apply our layerwise model to the prediction of failure in these joints, symmetry is applied as shown in Figure 89 (right part). At the left end of the adherend, a force  $F$  and a bending moment  $M = b \times F$  are applied. A plane strain state is assumed. In [16], Castagnetti et al. assumed a purely brittle response for the adhesive and didn't characterize its real mechanical behavior by means of a tensile test. In [23], Goglio et al. performed mechanical tests with bulk specimens of the same adhesive tested by Castagnetti et al. A quick analysis of experimental stress-strain curves during the quasi-static tests made in [23] proves that an elastic perfectly plastic model and a 34MPa yield stress are a reasonable choice for modeling the behavior of the adhesive.

To predict a cohesive failure, a criterion based on a maximum cumulative plastic strain is adopted. When the failure force is applied to steel specimens, the average of predicted maximum cumulative plastic strains  $p$  among the specimens is 0.0541. These maximum values are reached at the left edge of the joint. The cohesive failure criterion is then:  $p > 0.0541$ . With this criterion, the M4-5N model predicts the failure loads for each specimen. Figure 90 displays the plot of the experimental and theoretical failure forces. The M4-5N predictions are very accurate.

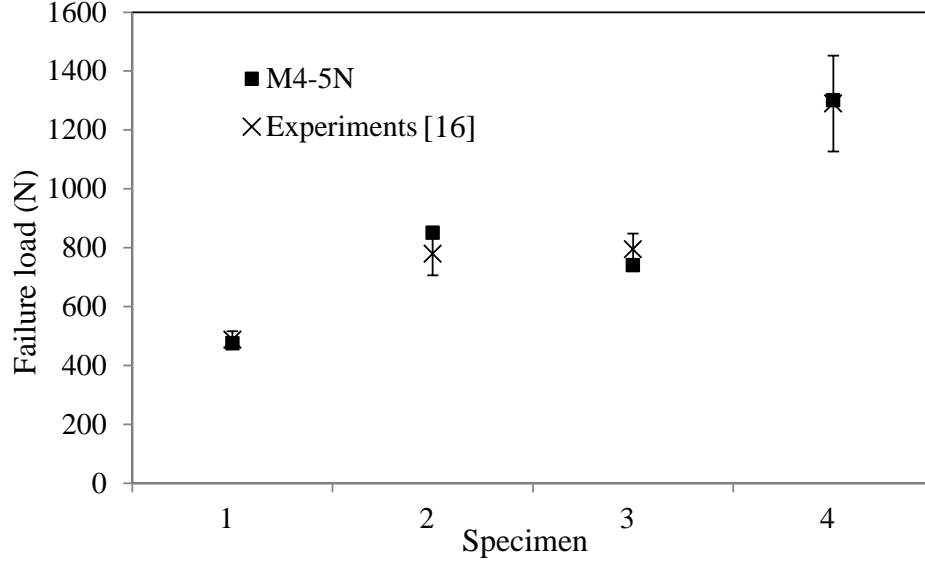


Figure 90. Failure loads for steel/epoxy specimens (experiments [16] and predictions)..

To predict an adhesive failure, we adopt a criterion similar to that obtained by Hart-Smith [24] to predict delamination onset based on a maximum “interfacial strain”. When the failure force is applied to aluminum joint specimens, the average of predicted maximum interfacial opening displacements  $\gamma_3$  among the specimens is  $1.63\mu\text{m}$  at the left edge of the

interface. The adhesive failure criterion is then:  $\varepsilon_z = \frac{\gamma_3}{s_a} > 0.0163$ , where  $\varepsilon_z$  is the interfacial

opening strain. With this criterion, the M4-5N model predicts the failure loads for each specimen. Let us point out that the M4-5N model predicts that the critical strain is reached without plasticity onset (the yield stress is not attained prior to the failure of aluminum joint specimens). Figure 91 displays the plot of the experimental and theoretical failure forces. The M4-5N predictions are correct but not as accurate as those for steel T-joint specimens. Let us remark that an important scattering of experimental data exists. This scattering is surely due to manufacturing defects and the sensitivity of the joint strength to the quality of the adhesive left edge as suggested by Castagnetti et al [16]. The important sensitivity of the joint strength to the manufacturing quality is a proof that failure occurs with negligible plastic strains in the adhesive which may smooth the stress concentrations. In this manner, the zero plastic strains calculated by the M4-5N model in the considered joints agree with the previous reasoning.

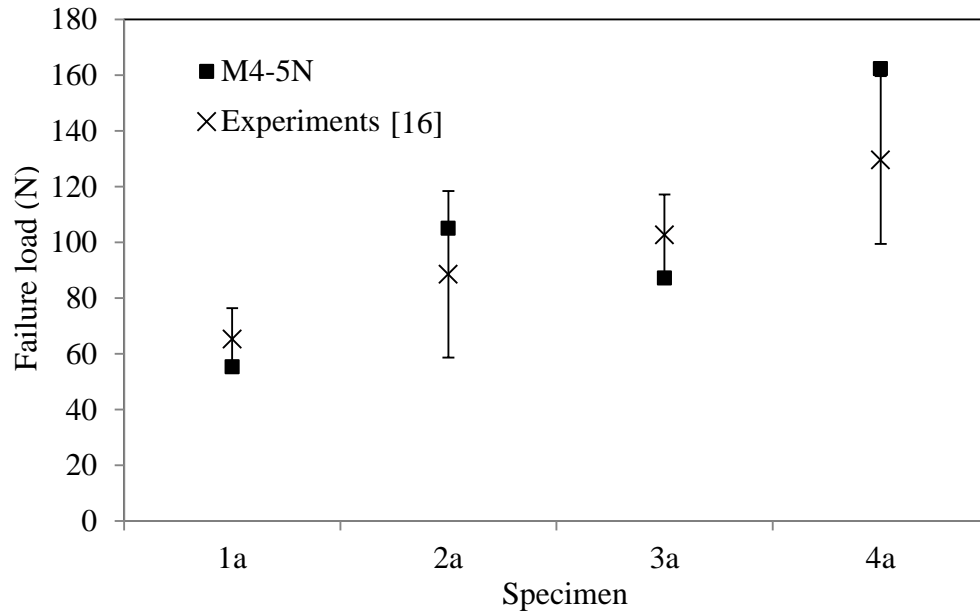


Figure 91. Failure loads for aluminum/epoxy specimens (experiments [16] and predictions).

The above examples prove then that the model is also suitable to predict cohesive and andherend failures due to peel stresses.

### 3. Conclusions

A linear approach and a non-linear approach were proposed to predict failure initiation in structural adhesive joints. The linear approach consists on the application of the twofold criterion proposed by Leguillon [20] to the prediction of failure of tests A, B, C, D and E shown in chapter II. The application of this criterion to the prediction of failure of adhesive joints has not been reported yet. Besides, an original stress criterion was proposed. The use of a classical fracture mechanics approach and the measurement of the size of defects helped to understand and predict the important scattering of the experimental results of tests E. The non linear approach was performed with the layer-wise model combined with a

criterion involving the plastic strains in the adhesive. This approach was applied to the prediction of failure of adhesive joints tested by other researchers.

Better predictions will be performed once the correct viscoplastic model will be developed. With this model, cohesive failure for different loading rates and conditions may be predicted.

## General conclusions

The main contributions of this project are:

- A rigorous proof of viscoplasticity and damage in Hysol adhesives
- A heat treatment (additional to the curing suggested by Hysol) to ensure a quasi-complete curing of Hysol adhesives
- A set of experimental data of adhesive joint failures which may help to determine failure criteria and test the accuracy of its failure predictions
- The implementation of a model of viscoplasticity with kinematic hardening in COMSOL Multiphysics software so as to compute more accurately stresses in adhesive joints
- The enhancement of a layer-wise model to calculate stresses in plate-like adhesive joints exhibiting non linearities in the adhesive layer
- A proposition of an original stress criterion for interfacial failure. This criterion is more adequate than a classic quadratic stress criterion
- The application of a twofold failure criterion involving simultaneously stress and energy conditions to predict failure initiation in adhesive joints.
- The application of the layer-wise model with pertinent failure criteria to predict failure in adhesive joints exhibiting significant material non-linearities.

For the next two years, an important effort will be made to include damage in the model of viscoplasticity shown in this project. This model will be validated with multiaxial tests at different loading rates with bulk adhesives. The model will be then implemented in COMSOL Multiphysics and the calculations will be validated by comparing the theoretical predictions to experimental data obtained from new experiments. The energy condition involved in the twofold criterion will be adapted so as to take into account other dissipations than cracking.



## References

- [1] C. Wang and P. Chalkley, "Plastic yielding of a film adhesive under multiaxial stresses.," *International Journal of Adhesion and Adhesives*, vol. 20, pp. 155-164, 2000.
- [2] J. Lemaitre and J. Chaboche, *Mechanics of solid materials*, Cambridge: Cambridge University Press, 1990.
- [3] E. Castillo González, "Modelado, Caracterización y Simulación del Comportamiento Elastoplástico de Adhesivos," Master's degree thesis. Centro de Investigación en Materiales Avanzados S.C., Chihuahua, Mexico., 2010.
- [4] J. Cognard, P. Davies, L. Sohier and R. Créac'hcadec, "A study of the non-linear behaviour of adhesively-bonded composite assemblies," *Composite Structures*, vol. 76, no. 1-2, pp. 34-46, 2006.
- [5] J. Cognard, R. Créac'hcadec, L. Sohier and P. Davies, "Analysis of the nonlinear behavior of adhesives in bonded assemblies—Comparison of TAST and Arcan tests," *International Journal of Adhesion and Adhesives*, vol. 28, no. 8, pp. 393-404, 2008.
- [6] J. Cognard, L. Sohier, R. Créac'hcadec, F. Lavelle and N. Lidon, "Influence of the geometry of coaxial adhesive joints on the transmitted load under tensile and compression loads," *International Journal of Adhesion and Adhesives*, vol. 37, pp. 37-49, 2012.
- [7] M. Zgoul, "Use of artificial neural networks for modelling rate dependent behaviour of adhesive materials," *International Journal of Adhesion and Adhesives*, vol. 36, pp. 1-7, 2012.
- [8] P. Pandey and S. Narasimhan, "Three-dimensional nonlinear analysis of adhesively bonded lap joints considering viscoplasticity in adhesives," *Computers & Structures*, vol. 79, no. 7, pp. 769-783, 2001.
- [9] J. Cognard, P. Davies, B. Gineste and L. Sohier, "Development of an improved adhesive test method for composite assembly design," *Composites Science and Technology*, vol. 65, no. 3-4, pp. 359-368, 2005.
- [10] L. Mendoza-Navarro, A. Diaz-Diaz, J. Caron and S. Chataigner, "Enhanced layerwise model for laminates with imperfect interfaces – Part 2: Experimental validation and failure prediction," *Composite Structures*, vol. 94, no. 3, pp. 1032-1037, 2012.
- [11] R. Alvarez-Lima, A. Diaz-Diaz, J. Caron and S. Chataigner, "Enhanced layerwise model for laminates with imperfect interfaces – Part 1: Equations and theoretical

- validation," *Composite Structures*, vol. 94, no. 5, pp. 1694-1702, 2012.
- [12] G. Aquino de Los Rios, R. Castañeda Balderas, V. Duong, S. Chataigner, J. Caron, A. Ehrlacher, G. Foret and A. Diaz Diaz, "Laminated materials with plastic interfaces: modeling and calculation," *Modeling and Simulation in Materials Science and Engineering*, vol. 17, no. 2, pp. 1-21, 2009.
- [13] A. Chabot, "Analyse des efforts à l'interface entre les couches des matériaux composites à l'aide des M4.," PhD thesis. Ecole Nationale des Ponts et Chaussées., France, 1997.
- [14] R. Carreira, J. Caron and A. Diaz Diaz, "Model of multilayered materials for interface stresses estimation and validation by finite element calculations.," *Mechanics of Materials*, vol. 34, no. 4, pp. 217-230, 2002.
- [15] V. Duong, A. Diaz Diaz, S. Chataigner and J. Caron, "A layerwise finite element for multilayers with imperfect interfaces," *Composite Structures*, vol. 93, no. 12, pp. 3262-3271, 2011.
- [16] D. Castagnetti, E. Dragoni and A. Spaggiari, "Failure analysis of bonded T-peel joints: Efficient modelling by standard finite elements with experimental validation," *International Journal of Adhesion and Adhesives*, vol. 30, no. 5, pp. 306-312, 2010.
- [17] A. Diaz Diaz and J. Caron, "Interface plasticity and delamination onset prediction," *Mechanics of Materials*, vol. 38, no. 7, pp. 648-663, 2006.
- [18] S. Chataigner, J. Caron, V. Duong and A. Diaz Diaz, "Experimental and numerical investigation of shear strain along an elasto-plastic bonded lap joint," *Construction and Building Materials*, vol. 25, no. 2, pp. 432-441, 2011.
- [19] D. Leguillon, G. Marion, R. Harry and F. Lécuyer, "The onset of delamination at stress-free edges in angle-ply laminates — analysis of two criteria," *Composites Science and Technology*, vol. 61, no. 2, pp. 377-382, 2001.
- [20] D. Leguillon, "Strength or toughness? A criterion for crack onset at a notch," *European Journal of Mechanics - A/Solids*, vol. 21, no. 1, pp. 61-72, 2002.
- [21] E. Martin, D. Leguillon and N. Carrère, "A twofold strength and toughness criterion for the onset of free-edge shear delamination in angle-ply laminates," *International Journal of Solids and Structures*, vol. 47, no. 9, pp. 1297-1305, 2010.
- [22] O. Volkersen, "Die nietkraftverteilung in zugbeanspruchten mit konstanten laschenquerschnitten," *Luftfahrtforschung*, vol. 15, pp. 41-47, 1938.
- [23] L. Goglio, L. Peroni, M. Peroni and M. Rossetto, "High strain-rate compression and tension behaviour of an epoxy bi-component adhesive," *International Journal of*

*Adhesion and Adhesives*, vol. 28, no. 7, pp. 329-339, 2008.

- [24] L. Hart-Smith, "Adhesive bonded double lap joints. Technical Report NASA-CR-112235," NASA-Langley Contract Report, 1973.

## Appendix 1. Drawings and dimensions of devices.

### 1. Parts of the Arcan device.

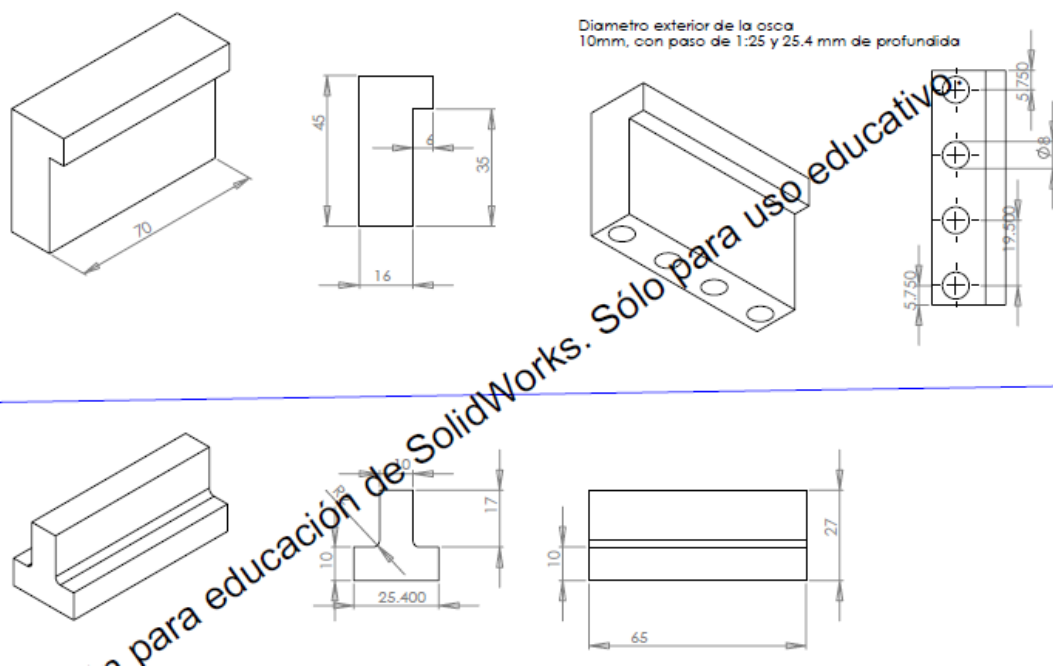
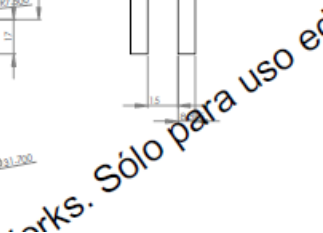


Figure 92. Arcan specimen and grips.



106

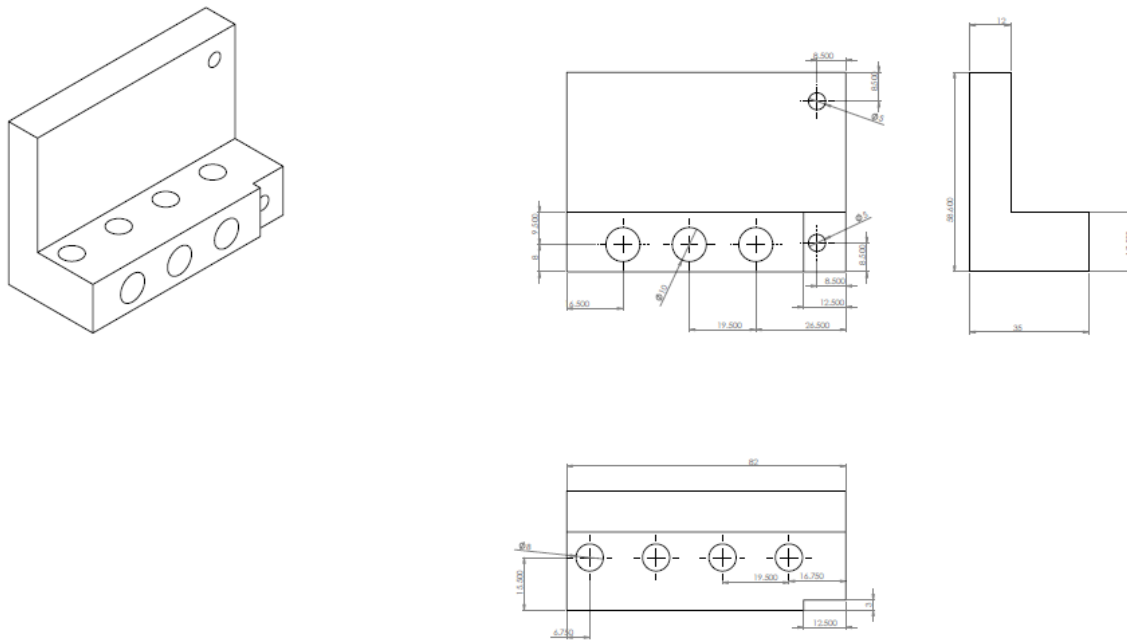


Figure 95. Adapter between grips and Arcan disc.

## 2. Type F specimens.

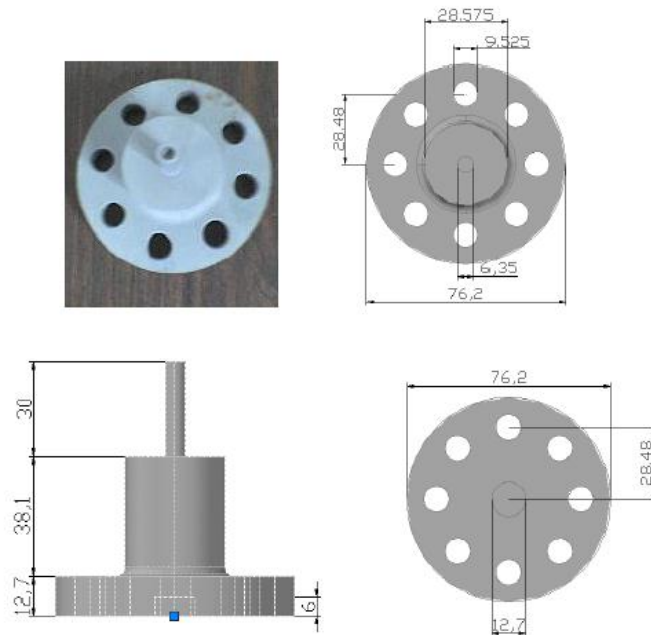


Figure 96. Male part (specimen F)

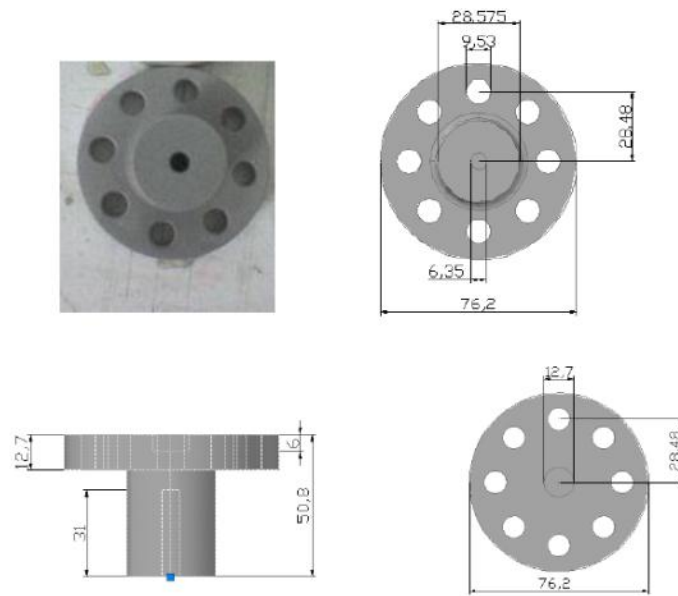


Figure 97. Female part (specimen F)

## Appendix 2. Publications and thesis

### 1. Thesis

1. *Mario Alberto Madrid Pérez (Master's degree). "Criterio de falla de interfase para uniones adhesivas – Criterion of interfacial failure in adhesive joints". Maestría en ingeniería en estructuras. Universidad Autónoma de Chihuahua. December 2011.*

- Abstract: (*In this thesis, type F tests and other tests with adhesive joints without heat treatment were performed*). Tests on adhesive joints with metallic substrates (steel and aluminum) and commercial adhesives (Loctite D609 and Loctite E-20HP) were performed. Butt joints to perform tensile/torsion tests were designed as well as double lap joints tests. Linear elastic assumptions were adopted and a stress criterion involving the interfacial stresses evaluated at a characteristic distance from the edge was used. In this criterion, the interfacial shear stress appears in a quadratic form whereas the exponent of the normal stress is 1. The accuracy of the predictions is discussed.

- The thesis can be requested to Mr. José Antonio Portillo Ocegüera ([jportillo@uach.mx](mailto:jportillo@uach.mx)) at the Universidad Autónoma de Chihuahua.

2. *Eduin Iván González Castillo (Master's degree). "Modelado, Caracterización y Simulación del Comportamiento Elastoplástico de Adhesivos – Modeling, characterization and simulation of the elastoplastic behavior of adhesives. Maestría en Ciencia de Materiales. Centro de Investigación en Materiales Avanzados S.C. December 2010.*

- Abstract: In this work a Drucker-Prager-type model for two structural adhesives (one more ductile than other) was developed. The adhesives were tested in tension and torsion. The accuracy of the model was tested by comparing the model predictions against experimental results. A computational tool was developed to determine stresses and strains in the torsion case. The accuracy of the model is discussed. (*It is worth mentioning*



*that in this thesis the Hysol adhesives were tested but the heat treatment that ensures the quasi-complete curing was not applied).*

- The thesis can be requested to Mr. Marcos López Carrasco at CIMAV ([marcos.lopez@cimav.edu.mx](mailto:marcos.lopez@cimav.edu.mx)).
3. *Francisco Octavio Pérez Blanco. “Criterio de falla de interfase para el adhesivo D609/acero 1018 – Criterion of interfacial failure for a D609 adhesive and a 1018 steel”. Maestría en Ciencia de Materiales. Centro de Investigación en Materiales Avanzados S.C. May 2012.*
- Abstract: In the present work we develop a criterion to predict the interfacial failure in adhesive joints made of Loctite D609/Carbon steel 1018. The criterion involves stress and strain energy conditions. This type of criterion has not been applied to heterogeneous materials and its application to adhesive joints represents the first innovation developed in the present work. The criterion is based on the stress and energy calculations and experiments with ARCAN specimens that allow a scanning of the failure envelope, varying the interfacial shear / normal stress ratio. Also torsion tests were performed with butt joints which generate a pure shear stress state without normal stresses. The analysis of the curing process of the adhesive helped us to define a thermal treatment required to ensure a quasi-complete curing reaction. The finite element technique is applied to calculate stresses and energies. The strength of the specimens tested exhibited a large statistical dispersion as has been reported in previous works. This dispersion is due to manufacturing defects at the specimen edges. At this moment, it is not possible to fully control these defects. Finally, the second and more important innovation of the work consists in predicting the strength dispersion by taking into account the maximum defect size measurements and performing theoretical calculations. Thus, this work is an important contribution to the design of structural adhesive joints.
  - The thesis can be requested to Mr. Marcos López Carrasco at CIMAV ([marcos.lopez@cimav.edu.mx](mailto:marcos.lopez@cimav.edu.mx)).

4. Luis Ernesto Mendoza Navarro (PhD). “Interfacial failure of adhesive joints with a brittle adhesive”. Doctorate in Materials Science. The student will finish his thesis by December 2012.
5. Ignacio Alberto Estrada Royval (PhD). “Modeling of the viscoplastic behavior of adhesives”. Doctorate in Materials Science. The student will finish his thesis by December 2014.

## **2. Publications in conferences**

1. Eduin Iván González Castillo, Rubén Castañeda Balderas, Alberto Díaz Díaz. Simulación del comportamiento elastoplástico de adhesivos sometidos a torsión. XXX Congreso internacional de metalurgia y materiales, Saltillo, Mexico. October 21-23, 2009.
2. M.A. Madrid-Pérez, R. Castañeda-Balderas, A. Díaz-Díaz. Analysis of adhesive failure criteria in structural joints. CC2011 Civil-Comp Conference. Chania, Crete, Greece. 6-9 September 2011.

## **3. Publications in journals**

1. René Alvarez-Lima, Alberto Diaz-Diaz, Jean-François Caron, Sylvain Chataigner. Enhanced layerwise model for laminates with imperfect interfaces – Part 1: Equations and theoretical validation. Composite Structures, Volume 94, Issue 5, pp. 1694-1702, 2012.
2. Luis-Ernesto Mendoza-Navarro, Alberto Diaz-Diaz, Jean-François Caron, Sylvain Chataigner. Enhanced layerwise model for laminates with imperfect interfaces – Part 2: Experimental validation and failure prediction. Composite Structures, Volume 94, Issue 3, pp. 1032-1037, 2012.

3. Luis Ernesto Mendoza-Navarro, Alberto Diaz-Diaz, Rubén Castañeda Balderas, Stéphane Hunkeler, Romuald Noret. Interfacial failure in adhesive joints: experiments and predictions. Submitted to the International Journal of Adhesion and Adhesives on June 2012. *In this paper, the tests and failure predictions with adhesive joints using the polyester adhesive are shown.*